Caractérisation et conception de micro-aimants pour la lévitation diamagnétique de micro- et nano- particules

Mikhail S. Kustov

To cite this version:

Mikhail S. Kustov. Caractérisation et conception de micro-aimants pour la lévitation diamagnétique de micro- et nano- particules. Sciences de l'ingénieur [physics]. Université de Grenoble, 2010. Français. NNT : . tel-00578044

HAL Id: tel-00578044
https://theses.hal.science/tel-00578044

Submitted on 18 Mar 2011

HAL is a multi-disciplinary open access archive for the deposit and dissemination of scientific research documents, whether they are published or not. The documents may come from teaching and research institutions in France or abroad, or from public or private research centers.

L'archive ouverte pluridisciplinaire **HAL**, est destinée au dépôt et à la diffusion de documents scientifiques de niveau recherche, publiés ou non, émanant des établissements d'enseignement et de recherche français ou étrangers, des laboratoires publics ou privés.

UNIVERSITE DE GRENOBLE

N° attribué par la bibliothèque
|__|__|__|__|__|__|__|__|__|__|

T H E S E

pour obtenir le grade de

DOCTEUR DE L'Université de Grenoble

Spécialité : « *Génie Electrique* »

préparée au laboratoire de Génie Electrique de Grenoble et à l'Institut Néel

dans le cadre de **l'Ecole Doctorale** « *Electronique, Electrotechnique, Automatique, Télécommunication, Signal* »

présentée et soutenue publiquement

par

Mikhail Kustov

le 3 décembre 2010

CARACTERISATION ET CONCEPTION DE MICRO-AIMANTS POUR LA LEVITATION DIAMAGNETIQUE DE MICRO- ET NANO-PARTICULES

DIRECTEUR DE THESE : Orphée Cugat
CO-DIRECTEURS DE THESE : Nora M. Dempsey et Gilbert Reyne

JURY

M. Leon Abelmann	, Président et Rapporteur
M. Rudolf Schäfer	, Rapporteur
M. Orphée Cugat	, Directeur de thèse
Mme Nora M. Dempsey	, Co-encadrante
M. Gilbert Reyne	, Co-encadrant
M. Vincent Mosser	, Examinateur
M. Rostislav Grechishkin	, Invité

Characterization and design of micro-magnets for the diamagnetic levitation of micro- and nanoparticles

Abstract:

Integrated film micro-magnets have many potential applications in various types of magnetic micro-systems. To produce the required magnetic field distributions and field gradients, the magnets need to be laterally patterned on the micron-scale. Quantitative characterization of their stray fields is needed to assess their magnetic quality as well as to optimize the design of micro-systems incorporating these micro-magnets. In this work, both scanning Hall probe microscopy and magneto-optic (MO) microscopy have been used for the measurement of the stray magnetic fields produced by micro-patterned Nd-Fe-B films. A novel approach to making 3D measurements using a single-component Hall probe has been proposed and validated. The possibility to do quantitative MO imaging using a unixial MO indicator film in a bias field has been demonstrated. Measured field profiles have been used to extract information concerning the magnetic microstructure of the micro-magnets.

The micro-magnets studied in this work were designed for use in micro-systems, in particular those exploiting diamagnetic levitation. Theoretical and experimental aspects of diamagnetic levitation (diamagnets above magnets, magnets above diamagnets) have been explored. The optimal dimensions of a levitating magnet have been found in order to optimize its levitation height or its permissible load. The levitation of a unidirectionally magnetized micro-magnet has been demonstrated experimentally. An original levitation micro-device with enhanced stability, incorporating both hard and soft elements, has been proposed and simulated.

Keywords: magneto-optic imaging, scanning Hall probe microscopy, micro-patterned Nd-Fe-B films, diamagnetic levitation

Caractérisation et conception de micro-aimants pour la lévitation diamagnétique de micro- et nano-particules.

Résumé:

Les micro-aimants intégrés en couches ont de nombreuses applications potentielles dans divers types de microsystèmes magnétiques (Mag-MEMS). L'aimantation de ces micro-aimants doit être latéralement configurée et structurée à l'échelle du micromètre, afin de générer les distributions adéquates de champs et gradients magnétiques. La caractérisation quantitative de ces champs magnétiques est nécessaire pour évaluer les propriétés magnétiques des micro-aimants ainsi que pour optimiser la conception des Mag-MEMS dans lesquels ils s'intègrent.

Dans ce travail, nous avons utilisé deux techniques pour mesurer les champs magnétiques générés par des couches micro-structurées d'aimants au néodyme-fer-bore (Nd-Fe-B) de plusieurs micromètres d'épaisseur: la microscopie par balayage d'une sonde Hall, et la microscopie magnéto-optique (MO). Nous avons proposé et validé une nouvelle approche de la mesure 3D de champ à l'aide d'une seule sonde Hall unidirectionnelle. Nous avons démontré la faisabilité de l'imagerie MO quantitative à l'aide d'un film MO uniaxial dans un champ d'offset. Nous avons extrait de la mesure des profils de champ des informations sur la micro-structure magnétique des micro-aimants.

Les micro-aimants étudiés dans cette thèse ont été conçus pour leur utilisation dans des Mag-MEMS spécifiquement dédiés à l'exploitation de la lévitation diamagnétique. Nous avons exploré les aspects théoriques et expérimentaux de la lévitation diamagnétique de matériaux diamagnétiques sur des réseaux intégrés de micro-aimants, et réciproquement la lévitation de micro-aimants sur des substrats diamagnétiques, sous l'effet de leurs propres champs et gradients magnétiques. Nous avons cerné les dimensions optimales d'un micro-aimant en lévitation sur un substrat de graphite, afin d'optimiser sa charge utile ou sa hauteur de lévitation. Nous avons démontré expérimentalement la lévitation d'un micro-aimant d'aimantation unidirectionnelle. Enfin, nous avons proposé et simulé un microsystème original incorporant des matériaux magnétiques durs et doux, dont la lévitation est stable dans n'importe quelle orientation.

Mots Clés :: microscopie magnéto-optique, microscopie par balayage d'une sonde Hall, couches micro-structurées d'aimants au néodyme-fer-bore (Nd-Fe-B), lévitation diamagnétique

TABLE OF CONTENTS

GENERAL INTRODUCTION

The great potential for use of magnets in micro-systems has stimulated much effort in the preparation of magnets at the micron scale. The assessment of these micro-magnets, in particular the characterization of the stray magnet fields produced by them, should prove invaluable for the optimization of material processing as well as micro-system design.

In this work we will describe the use and development of two techniques for the localised characterisation of the stray fields produced by NdFeB high performance micro-magnets, namely scanning Hall probe microscope and magneto-optic microscopy. Experimentally determined profiles will be compared with analytical calculations. A novel method for the measurement of the 3 spatial components of the stray field, using a single component probe, will be presented, together with test results. Concerning magneto-optic microscopy, the use of magneto-optic indicator films for the characterization of micro-magnets will be presented. Test results will be shown, to demonstrate the use of both planar and uniaxial MOIF for the qualitative and quantitative characterization of the stray field patterns produced by micro-magnets.

We will present scanning Hall probe microscopy measurements of the stray fields produced by Nd-Fe-B hard magnetic films. The hard magnetic films were patterned at the micron scale using both topographic and thermomagnetic methods. The experimental field profiles will be compared to analytical calculations, to access, in a non-invasive manner, information concerning the micro-magnets' internal magnetic structure. The measured field profiles will be used to derive the spatial variation of the field and field gradient values at different distances from the sample surface.

The design of plate-like levitating systems, which have potential applications in a variety of micro-systems, such as shock sensors, inclinometers, accelerometers, micro-transporters etc., will be presented. Two variants are considered. In the first case we deal with a diamagnetic body in levitation above an array of micro-magnets, in the second with the levitation of a micro-magnet above a diamagnetic substrate. For the case of a diamagnetic plate in levitation above an array of micro-magnets, we have designed a novel "flying carpet" which can be stable in position either above or below the magnetic track. This is possible because in addition to the repulsive force between the diamagnetic plate and the magnet, we propose to induce an attractive force between the bodies by adding a layer of soft magnetic material to the outer side of the diamagnetic plate. Semi-analytical modeling was used to calculate the plate to track distance for the plate above and below the track.

For the case of a micro-magnet in levitation above a diamagnetic substrate, we have used modeling to optimize the magnet dimensions with respect to the maximum achievable levitation height and the maximum permissible load on the levitating magnet. Two variants were considered for the magnet: 1) unidirectional magnetization (single dipole) and 2) bi-directional magnetization (double-dipole). For the later, spacing between the two dipoles was also considered.

Finally, we will present some experimental results which are directly or indirectly related to diamagnetic levitation. The ultimate aim, not yet achieved, is to prepare model levitation systems in which we levitate objects of controlled shape and size. Such model systems would serve in the analysis of experimental diamagnetic levitation.

Since we are interested in the use of diamagnetic levitation in micro-systems, we restrict ourselves to the use of materials directly prepared at the micron scale. Both sputtering and electro-deposition have been used. In the first part we will present results concerning the levitation of a micro-magnet above a diamagnetic substrate. In the end we will also present results concerning attempts to prepare a diamagnetic material (Bi), in a controlled shape (1D wires and 2D sheets), at the micron scale.

CHAPTER 1: STATE OF THE ART

1. State of the art

This chapter includes two sections; the first section gives an overview of modern methods of magnetic field characterization, while the second section briefly describes history and the state of the art of diamagnetic levitation.

1.1 Magnetic field characterization

1.1.1 General remarks

Alongside with the traditional problems of estimating the values of uniform magnetic fields at one or several points of space the magnetic metrology includes the task of characterizing the magnetic induction vector distribution in nonuniform fields. In the latter case the volume of the information scope depends not only on the parameters of the sensor taken alone but also on the number of measurement points and their spatial distribution. The control of magnetic field spatial distribution is required for the development of devices based on the utilization of assigned magnetic field configuration, such as electromagnetic actuators, motors, separators, filters, microelectromechanical systems (MEMS), etc., as well as for the solution of inverse problems – reconstruction of the internal structure of a magnetic source by its external field.

Of special concern are visualizing tools that render magnetic phenomena and structure as images, thus making them visible to the unaided eye satisfying an elemental craving to see the world by our own eyes [Wils.’98]. An impressive suite of imaging tools has been developed over the intervening 150 years including sophisticated modern instruments like electron microscopes in parallel with such old techniques as Faraday and Kerr effect-based magneto-optic microscopy or direct detection of magnetic forces [Freem.’01].

Due to rapid development of micro- and nanotechnologies the interest in magnetic measurements shifts increasingly to the characterization of nonuniform magnetic fields localized or distributed over the regions of space having characteristic lengths in the micron and submicron range. This fact urges to develop new methods or modify the existing ones to satisfy the increased requirements to magnetic characterization with respect to its spatial resolution, functionality, sensitivity, accuracy, etc.

Following Freeman [Freem.'01] it is convenient to loosely classify the imaging techniques in use today into two groups according to the physical mechanism of interaction between the probe and sample, namely *stray field mapping* and *mapping of the magnetization* distribution. The external stray field mapping is of primary interest for the present study oriented on MEMS applications, because it is this field which determines the working forces of interaction with either electric currents or magnetically active micro-objects outside the micromagnet. The methods of magnetization mapping which practically are reduced to the methods of domain structure observation and analysis were comprehensively described by Alex Hubert and Rudolf Schäfer [Hub.'09]

Here we give an overview of the methods of stray field mapping.

1.1.2 Powder pattern Bitter technique

For a long period, the Bitter method offered the greatest spatial resolution and sensitivity in delineating magnetic nonuniformities of different origin. Progress in the art of obtaining Bitter patterns was related mainly with the magnetic domain structure studies. A comprehensive account of the Bitter method as applied to domain structure observations was given by Hubert and Schäfer [Hub.'09], so here only an overview and some recent details on this technique will be given.

In the Bitter method, the surface of a magnetic material is covered by a thin layer of nanoparticles (size 5 – 20 nm) suspended in liquid media (water, kerosene, oil). Numerous recipes of preparation and stabilization of magnetic liquids, as well as contrast theory and experimental conditions for the observation of magnetic patterns are known [Hub.'09]. The optical contrast arises from the nanoparticle concentration at the places of largest field gradients. Moreover, optical anisotropy may be induced in the magnetic liquid (ferrofluid) by the local field under study producing additional optical contrast owing to the birefringence observed in polarized light [Hart.'82, Jones '82]. Due to this effect a construction of the directional map of the stray field pattern becomes possible. The resolution of liquid Bitter patterns is approximately that of the optical microscope (~0.5 μm). Thin solid films may be obtained from the ferrofluid if some agents are added to the nanoparticle suspension so that it forms a continuous film on drying. This will increase the resolution, because the dried nanoparticle layer will be thinner than the original ferrofluid. The dried film may be peeled off the sample and examined in greater detail and with in scanning or tunneling microscopes [Šimš.'91, Rice '91]. In this case the resolution is determined by the size of nanoparticles rather than optical limitation.

Among other modifications of the Bitter method is that of magnetic "smoke" produced by evaporating a magnetic material in a low pressure gas. During this process single-domain nanoparticles of spherical shape may be formed; the size of these particles is regulated by the gas pressure and conditions of evaporation [Hub.'09, Sak.'92].

During settling the particles agglomerate in the magnetic stray fields on the surface of the objects under study. Among the recent applications of the Bitter decoration technique are high-resolution studies of vortex structure in superconductors [Sug.'99]. Paramagnetic oxygen particles may be also used to observe the decoration at low temperatures [Szew.'83].

Technology of micro-encapsulation which allows a thin 2-mil ($\approx 50\ \mu$) layer of ferrofluid slurry to be bonded to a 5-mil sheet of plastic film was applied to produce a flexible viewing film for dc magnetic fields [Ardiz.]. During the encapsulation process nickel nanoparticles become engulfed within gelatinous membranes coated onto the plastic film. After complete drying the nanoparticles maintain freedom of movement within the gelatinous membranes. As conventional ferrofluids the viewing film placed on the surface of magnetic material delineates the regions of largest field gradients, so a particularly useful application is in the identification of changes in magnetic polarity (Fig. 1.1). The currently available viewing films can detect fields as low as only a few gauss (tenths of millitesla); however, the resolution of the available films is too low (~0.2 mm) to be useful for the study of MagMEMS.

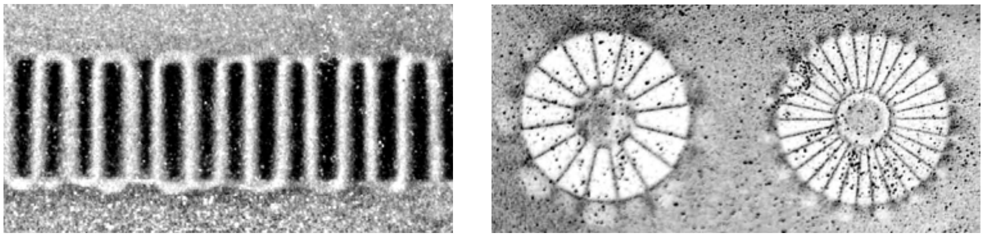

Fig. 1.1. Magnetic field at the surface of a cylindrical, radially magnetized multipole rotor (evolvent width 8 mm) and of 8- and 15-pole ∅8 mm axially magnetized Sm-Co rotors observed with a ferrofluid-based viewing film.

In summary it may be concluded that the Bitter imaging methods, due to their sensitivity, versatility, high resolution, simplicity and cheapness still find use in solving various tasks and all the same there is enough room for further improvements. Of interest are modern methods of production and stabilization of monodisperse nanoparticle ensembles. Improved sensitivity may be presumed with the use of needle-like particles (nanowires) having increased shape anisotropy and microemulsions of the water-in-oil or oil-in-water type with enlarged magnetic moment [Zhang ’05]. Refined visibility may be provided by the ferrofluids containing fluorescent nanobeads or highly reflective metal flakes. One more interesting proposal is to grow magnetic cobalt nanoparticles inside the hollow protein capsid shell derived from the T7 bacteriofhage virus [Liu ’06]. Finally, it may be mentioned that the ferrofluids may be exploited to mechanically control the position of other tiny objects [Yell.’05]. In this case the imaging properties of ferrofluids may be combined with their utilization in micromanipulators.

1.1.3 Scanning probe microscopy (SPM)

A general feature of SPM is the use of a miniature mechanical, electrical, optical, thermal, or other probe prepared to localize a specific interaction with the surface under study [Hart.’05, Nölt.’06].

The probe is generally raster-scanned over the surface and the interaction is measured and displayed as a function of the probe position. The measured interactions can range from current in the case of the scanning tunneling microscope (STM) to force in the case of the atomic force microscope (AFM) [Binn.'86] and evanescent optical excitations in the case of the scanning near-field optical microscope (SNOM).

1.1.3.1 Vibrating scanning probe

The first observations of the stray fields emanating from the magnetic domains of a ferromagnetic sample with a scanning probe microscope were made by Jan Kaczer in 1955 [Kacz.'55, Kacz.'56] just six years after the experimental verification of the existence of ferromagnetic domains using colloidal particles as described by Bozorth [Boz.'49]. In Kaczer's microscope a small piece of a permalloy wire serving as a probe is vibrated in the vicinity of a field gradient (Fig. 1.2).

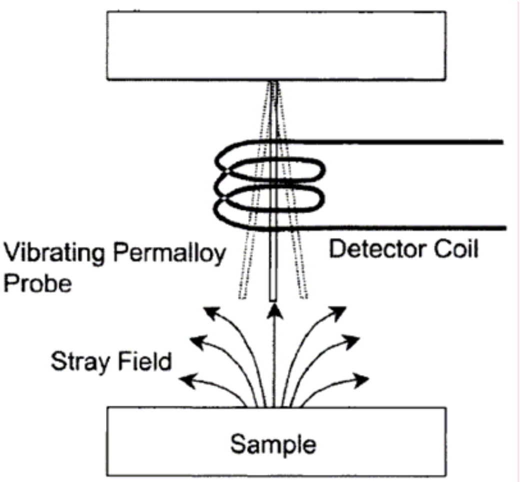

Fig. 1.2. Kaczer's permalloy probe microscope. The probe is oscillated in a detector coil. As the probe is scanned over the stray field from the sample, the flux through the permalloy probe changes which in turn changes the voltage induced in the detector coil.

The output AC signal is measured by a pickup coil at the other end of the wire. As the probe is scanned over a sample surface, the magnetically soft permalloy probe's magnetic state changes in response to the localized field from the sample. The resulting images correlate well with colloid images of the same surface, clearly mapping domain walls and defects in the sample.

With the use of the permalloy probe described above the interaction between the probe and the sample has to be taken into account. To avoid any influence by the probe on the sample a vibrating coil pickup system was developed [Haged.'76, Wurm.'78], which needs no current and consists of nonmagnetic material. It works by the effect of electromagnetic induction. The pickup is a long rectangular loop of conducting material that is forced by a suitable driving system to vibrate in its long direction. A magnetic flux density perpendicular to the plane of the pickup loop will give rise to an induced voltage across its terminals. This voltage is proportional to the difference between the two values of the flux density at the narrow sides of the loop, if the amplitude is small compared to the length of the loop. This method has the advantage that the nonmagnetic probe does not influence the magnetic field of a specimen. The output signal is proportional to the difference between the two values of the flux density at the narrow sides of the loop, if the amplitude is small compared with the length of the loop.

The instrument has been developed for the measurement of magnetic stray fields of ferro- and ferrimagnetic samples without any influence of additional magnetic fields generated by the pickup system. The application mainly intended is to measure magnetic fields with values above some 10^{-4} T. In contrast to some other probes, e.g. such as magnetoresistors, there is no upper limit to the range. The problem with this type of probes is that even with pickup coils of small area the field gradients typical for innovative MagMEMS under development are averaged over too large an area.

Another device for measuring with the aid of vibrating probe is one described by J.M. Lommel [Lomm.'67]. In Lommel's instrument advantage is taken of the localizing effect of the gap in an inductive recording head. Field gradients occurring over small regions are detected as voltages induced in the coil on the head when the recording head gap is vibrated through the field gradient. The vibration is parallel to the surface of the specimen which is scanned by moving it past the vibrating head.

In principal, the vibrating scanning probe technique may be considered as a variety of the magnetic force microscopy technique (that will be given in section 1.1.3.6), with a different detection mechanism.

1.1.3.2 Scanning magnetoresistance microscopy (SMRM)

Scanning magnetoresistance microscopy (SMRM) is one approach to measuring the spatial distribution of the magnetic flux emanating from magnetic sample surfaces. Since a magnetoresistive sensor and its related devices such as the spin-valve device are easily miniaturized and have high magnetic sensitivity at room temperature, a SMRM fitted with such sensors is useful for the quantitative measurement of magnetic fields [Liu ’04, Chris.’99].

A scanning magnetic microscope that uses commercial magnetoresistive record/playback heads as sense probes was proposed by S. Y. Yamamoto and S. Schultz [Yam.’97]. A high-resolution, linearized positioning stage was used to raster scan a magnetic sample with respect to the MR head while the head is in physical contact with the sample. An upper bound on the spatial resolution of 100 nm in the ‘‘downtrack’’ direction and 1–2 μm in the ‘‘crosstrack’’ direction of the head was achieved. An interesting possibility of applying localized fields to the sample via the inductive write element was mentioned which may be useful for some kinds of magnetic studies.

D. P. Pappas et al. [Papp.’05] described and demonstrated the applicability of an SMRM as a noninvasive method for use in forensic analysis and data recovery. The method of data acquisition used with the MR microscope involves scanning the MR sensor over the sample to build an image. A drawing of the sensor is shown in Fig. 1.3. The suspension is a flexible strip that enables the highly polished slider to press on the sample with very low force. The sensor is mounted on the front edge of the slider, and is in contact with the surface. The sensor measures the vertical component of the magnetic field. The intrinsic spatial resolution of the sensors is 0.05 μm in the scan direction along the suspension, and 5 μm laterally.

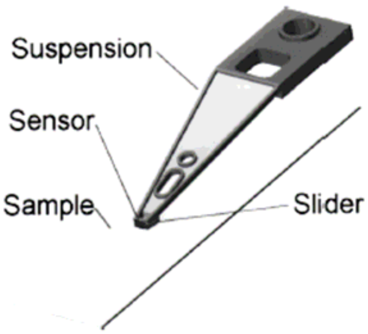

Fig. 1.3. Head assembly (not to scale) from hard disk drive that is used in the imaging technique. Elements include suspension, slider, and the MR sensor element [Papp.'05].

The sensors used in this instrument rely on the anisotropic magnetoresistance effect resulting in maximum resistance change in saturation of about 1% when a magnetic field is applied perpendicular to a current flow. The motion is controlled by a computer connected to servomotor-driven micrometers.

In the work of M. Nakamura et al. [Nak.'02] a cantilever with a magnetoresistive sensor was fabricated for SMRM in order to realize the simultaneous imaging of surface topography and stray magnetic field distribution. Fig. 1.4 and Fig. 1.5 show a SEM image of a cantilever and schematics for the SMRM. The cantilever is approximately 200 μm long, 50 μm wide, and 1 μm thick. Since the cantilever is designed for use with the contact mode atomic force microscope the stiffness of the lever is approximately 0.12 N/m and the measured resonance frequency is about 20 kHz. The magnetic sensor is 5 μm long, 2 μm wide, and 40 nm thick. The easy axis of the sensor is along the elongated side, so its magnetically sensitive direction is along the short side. The spatial resolution of the SMRM system is limited by the width of the MR element. To obtain topographic information of the sample surface, the contact-AFM measurement mode was used. The apex of the cantilever was used as an AFM probe. Since the MR sensor is about 5 μm distant from the apex, the MR images shift with respect to the AFM images obtained simultaneously. This shift was calibrated making use of the known separation distance. A MR image has been successfully obtained with lateral spatial resolution of a few μm and a high field sensitivity ($H_{\min}$~1.7 Oe) at room temperature.

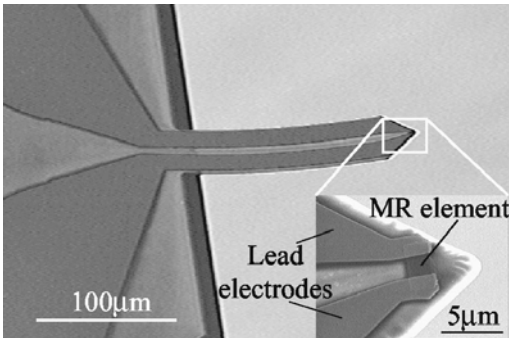

Fig. 1.4. Scanning electron microscopy micrograph of the cantilever with a magnetoresistive sensor. The inset is the enlarged image of the apex [Nak.'02].

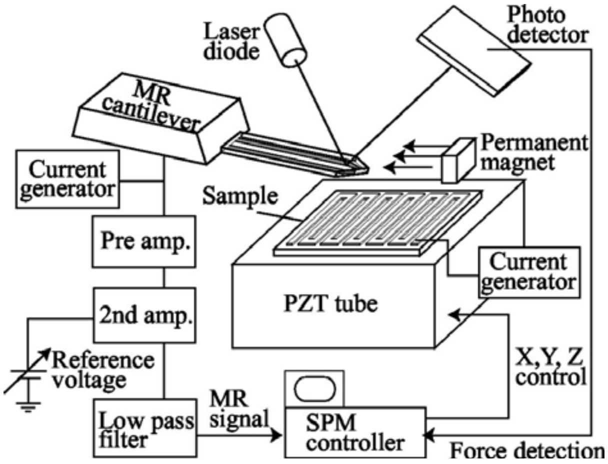

Fig. 1.5. A schematic of the SMRM microscope [Nak.'02].

1.1.3.3 Scanning superconducting quantum interference device (SQUID) microscopy (SSM)

A scanning SQUID microscope (SSM) is the most sensitive instrument for direct observations of local magnetic field distributions on a sample surface [Hart.'05].

A small pickup coil of the SQUID device scans on the surface of the sample, and local field variations are measured. There have been a variety of different techniques used for scanning the sample relative to the SQUID in SSM. These approaches were classified [Kirt.'02] as shown in Fig. 1.6. Of the various magnetic characterization techniques SSM is the most sensistive in terms of absolute magnetic field. As an example, for a pickup coil with a diameter of 10 µm this translates to a field of ~ 10^{-11} T.

The spatial resolution of the apparatus is limited by the diameter of the pickup coil and its liftoff height. Improvement of the SSM spatial resolution is the desirable goal for various experiments. A direct way of achieving high spatial resolution is reduction of SQUID-sample separation and microfabrication of smaller pickup coils. Another way is to attach a sharpened magnetically soft needle to the SQUID serving as a magnetic flux guide (MFG), by which a magnetic field is transferred from a point at the sample surface to the SQUID [Gud.'02, Hart.'05, Kon.'04] (Fig. 1.7). The use of the SQUID-MFG composition in the first place is very important for the SSM intended for room-temperature measurements.

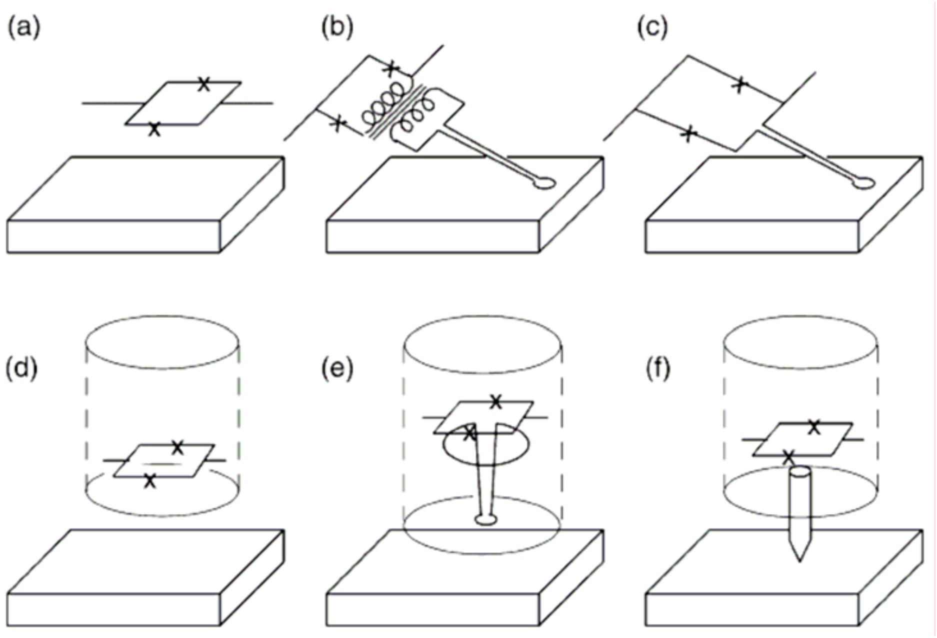

Fig. 1.6. Various strategies for scanning the sample relative to the SQUID. Both sample and sensor can be cooled (a–c) or only the SQUID (d–f). The field at the SQUID can be detected (a, d), or a superconducting pickup loop can be inductively coupled to the SQUID (b, e), or the pickup loop can be integrated into the SQUID design (c). In (f), a ferromagnetic tip is used to couple flux from a room temperature sample to a cooled SQUID [Kirt.'02].

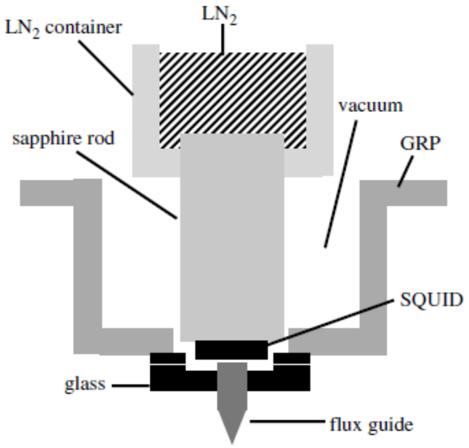

Fig. 1.7. Schematic diagram of the SQUID probe head. The flux guide was used to improve the spatial resolution [Kon.'04].

A number of recent improvements of the SSM include the improved fabrication of microSQUID tips using silicon micro machining and the precise positioning of the micrometer diameter microSQUID loop by electron beam lithography. The distance control during scanning is obtained by integrating the microSQUID sensor with a piezoelectric tuning fork acting as a force sensor allowing to control height and even topographic imaging [Hassel.'08; Veauvy '02].

1.1.3.4 Scanning Hall probe microscopy (SHPM)

The use of Hall effect probes to visualize spatially nonuniform magnetic field distributions dates back well over 30 years [Bend.'99].

Typical SHPM employ sensors based on thin films of bismuth or InAs and micrometer-driven X-Y-Z stages. The construction of the SHPM uses many standard techniques of scanning tunneling microscopy (STM) (see, e.g. [Khot.'08, Din.'05, Fedor '03, Oral '96, Brook '03].

The first microscope using a submicron Hall probe was developed by [Chang '92] (Fig. 1.8). In his work he was able to demonstrate a number of applications of the SHPM, including detecting surface fields with excellent sensitivity at close proximity to the sample, magnetic domain structure, individual vortices in superconductors films, etc.

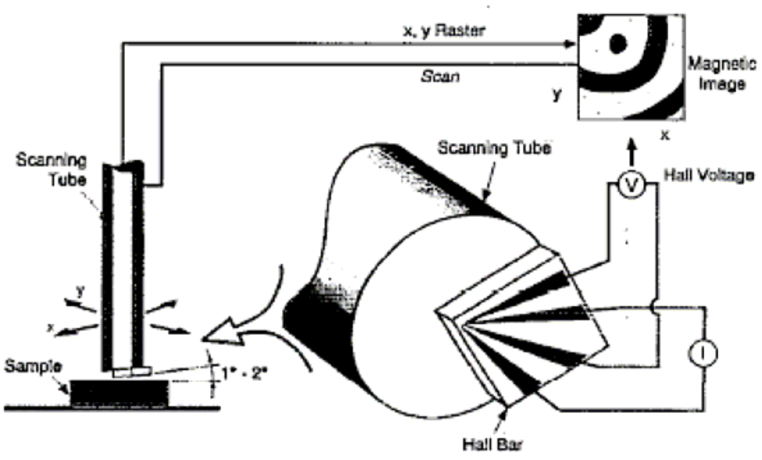

Fig. 1.8. A schematic of the scanning Hall probe microscope developed by Chang et al. [Chang '92].

An important contribution to the further development of SHPM technology was made by Vincent Mosser and Alexander Pross with collaborators [Mos.'94, Pross '04, Pross '05]. These authors raised the question of increasing the sensitivity of Hall sensors for room temperature applications, thereby increasing the attractiveness of the SHPM method for many researchers in various segments of magnetism. A series of second-generation quantum-well Hall probes was developed whereby the careful design of an AlGaAs/InGaAs/GaAs pseudomorphic heterostructure, chip layout, metal interconnects, and passivation layers has allowed a dramatic reduction of low-frequency noise sources. The Johnson noise-limited minimum detectable fields of these sensors are more than an order of magnitude lower than those used in early microscopes. These findings indicate that potentially the size of Hall sensors may be further reduced to form a nanosensor with ~ 80 nm spatial resolution.

It may be added that the performance of Hall sensors may be improved also by the use of magnetic flux concentrators [Leroy '08] in a way similar to magnetic flux guide (MFG) proved to be useful for SQUID microscopes. These factors undoubtedly increase the potential interest to SHPM compared with other magnetic characterization techniques.

Summarizing, we may mention that Hall probes are characterized by low self-fields, which makes them practically noninvasive; they possess rather good sensitivity (though much smaller in comparison to SQUIDs); they provide direct quantitative mapping of the out of plane stray field components, and their spatial resolution may start to rival magnetic force microscopes (MFM) in the near future.

1.1.3.5 Scanning vector Hall probe microscopy

In contrast to MFM, the scanning probe approach realized in SQUID microscopy, SMRM and SHPM is based on the use of microprobes having a direct response to the projection of magnetic flux density vector on the axis of sensitivity. Generally sensors sensitive to the magnetic field component perpendicular to the plane of observation are employed. While this is satisfactory for many research purposes, quantitative information of the other two components of the field may be also of interest.

Two approaches for the measurement of all three vector components of a magnetic field may be distinguished [Schott '98].

The first possibility is to assemble three identical unidirectional sensors orthogonally to each other in a 3D probe head. The combination of three sensors onto a single chip is not possible for most kinds of the sensors, so that packages of two or three separate chips are often used leading to alignment and angle errors and increasing the volume of the final device lowering the spatial resolution.

The second possibility consists of a single chip 3D Hall sensor based on an integrated vertical Hall device capable of detecting all three field components [Zong.'90, Misra 92, Greg.'03, Kejik '05].

Fedor et al. [Fedor '03] realized a vector Hall sensor by patterning Hall probes on tilted faces of a pyramidal-shaped mesa structure following overgrowth using metalorganic chemical vapor deposition (MOCVD) of the active layer, sensor definition and ohmic contact preparation. A sketch of the completed sensor is shown in Fig. 1.9. The active area of each sensor is 5×5 μm^2, and the perpendicular distance of their centers from the sample are ~ 3 µm if the top of the sensor and the sample are in contact. The critical figures-of-merit for the vector Hall sensor are the sensitivity, linearity, and resolution, defined by the properties of three individual probes in an external magnetic field. The sensitivities of the individual probes are S_1 = 53.17 mV/T, S_2 = 54.94 mV/T, S_3 = 53.73 mV/T and typical linearity error for all three probes is less then 1% for the magnetic field interval ± 150 mT for a bias current of 100 mA at 300 K. Time needed to collect data for one image of 256×256 points is ~ 1 hour for 2.5 μm step.

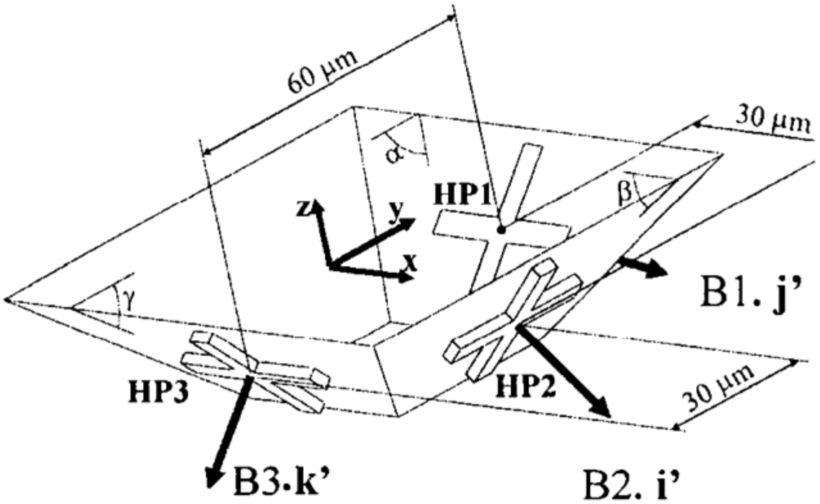

Fig. 1.9. 3D view of the vector Hall sensor. Individual probes HP1, HP2, and HP3 are placed on tilted facets of the pyramid, corresponding slopes of the sidewalls are α, β, γ respectively [Fedor '03].

1.1.3.6 Magnetic force microscopy (MFM)

The technique of magnetic force microscopy, its history and theory has been discussed extensively in the literature in numerous papers, books and reviews (see, e.g., [Thiav.'05, Abel.'05, Grut.'92, Port.'98, Abel.'98, Prok.'99].

The principle of magnetic force microscopy is very much like that of atomic force microscopy [Binn.'86], however in an MFM much smaller forces are measured. In essence every MFM is capable of AFM as well. In an MFM, the magnetic stray field above a flat specimen is detected by mounting a small magnetic element (the tip) on a cantilever spring very close to the surface of the sample. Typical dimensions are a cantilever length of 200 μm, a tip length of 4 μm, a diameter of 50 nm, and a distance from the surface of 30 nm. The force on the magnetic tip is detected by measuring the displacement of the end of the cantilever, usually by optical means. The forces measured in typical MFM applications are of the order of 30 pN, with typical cantilever deflections of the order of nanometers.

Advantages and drawbacks

The MFM has become a widespread, simple in operation as well as sample preparation tool that can provide relatively high-resolution (100 to 10 nm) images of the magnetic microstructures of a variety of materials. The MFM can image the fields from magnetic structures in air and in the presence of a protective overcoat. Thus, samples such as magnetic hard disk surfaces can be imaged quickly with very high resolution. In general, sample preparation for the MFM is much less demanding than for other techniques such as Lorentz microscopy or scanning electron microscopy with polarization analysis while yielding similar resolution. In addition, commercial availability of MFM have made it possible for a large number of non-specialists to use the technology thus multiplying the number of applications.

Disadvantages of MFM include that it is an indirect probe of the sample magnetization; it is sensitive to the stray fields gradients produced by the sample and it is difficult to extract quantitative information directly from MFM images, although different aspects of the complicated interaction between the sample surface and magnetic tip are very active topics of investigation.

Much like the colloid Bitter method the MFM is a magnetic imaging technique that is sensitive to the spatial derivatives of the magnetic fields generated by a sample. These fields do not depend on the sample magnetization directly but result from the divergence of the magnetization, $-\nabla \mathbf{M}$ for the bulk and dot product $\mathbf{M}\cdot\mathbf{n}$ for the surface. It may be said that the MFM is an instrument to visualize the nonuniformity of magnetization distribution. This results in contrast presentation of such features as domain walls, grain boundaries, twins, second phase inclusions, scratches, etc.

The analysis performed by B. Vellekoop, L. Abelmann et al. [Vell.'98] shows that it is impossible to determine the source of stray field from stray field measurements only. When a stray field is measured at constant height, it is possible to construct a virtual plane source of the stray field. As there are many configurations causing exactly the same stray field, it is impossible to measure the exact location of the stray field sources, i.e., determining the internal magnetic structure by means of a stray field sensing device such as an MFM in the general case is impossible.

Imaging in applied field

A powerful tool for understanding the dynamics of a magnetic sample is an applied field. A number of researchers have applied the field to a sample external to the MFM and used the MFM to image the resulting remanent state, while others have applied the field to the sample in-situ.

In the basic experimental setup, MFM measurements are performed at zero external magnetic field and at room temperature on a large variety of magnetic systems. By applying an external magnetic field in MFM, magnetization reversal processes of a system can be studied, especially by correlating field-dependent MFM investigations with bulk magnetization measurements. In order to study magnetic phase transitions, the MFM may be also equipped with a variable temperature stage. As an example, a permanent magnet variable system used by Mohanty et al. [Moh.'05] is shown in Fig. 1.10.

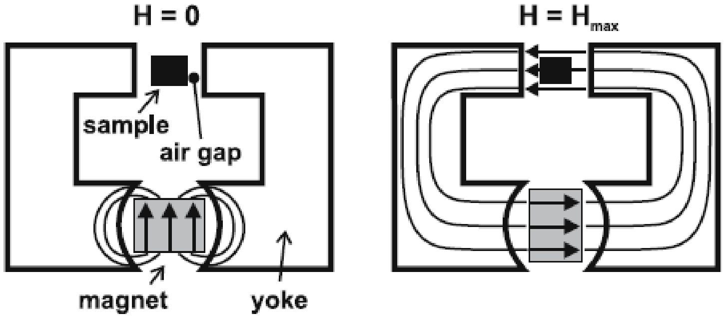

Fig. 1.10. Magnetic field setup: variable amounts of magnetic flux can be guided towards the sample space by the rotation of the permanent magnet [Moh.'05].

One way to simplify interpretation in an applied field is to use a tip with a coercivity that is very different from that of the sample, either much lower or much higher. Then, when the contrast is changing, one can be relatively confident of the origin of the change. For this reason, superparamagnetic tips or very high coercivity tips can be useful for applied field imaging.

1.1.3.7 Combined magneto-optic Kerr effect (MOKE) and MFM

In the situation of exploring a specimen for a specific local feature the process can be rather time consuming, because MFM scans are limited to maximum areas on the order of 100 μm on a side and each scan takes several minutes. Several researchers worked out a technique to predetermine a region of interest by combining the MFM with an optical Kerr microscope [Rave ’99, Rave ’98, Zueco ’98, Pokh ’97].

Kerr microscopy is fast, has a large field of view, and it is directly sensitive to the sample magnetization whereas the MFM has both high spatial resolution and sensitivity so the two techniques are quite complimentary to each other. In materials with magneto-optic contrast, combining the techniques can be powerful. The Kerr microscope may be adapted to a commercial top view MFM system thus enabling first to locate the regions of interest and then position the MFM cantilever at the selected place. In this way the authors of [Zueco ’98] were able to demonstrate in a very attractive way the separation of charge and susceptibility contrast effects important for the theory of contrast formation in MFM and interpretation of the obtained images (Fig. 1.11).

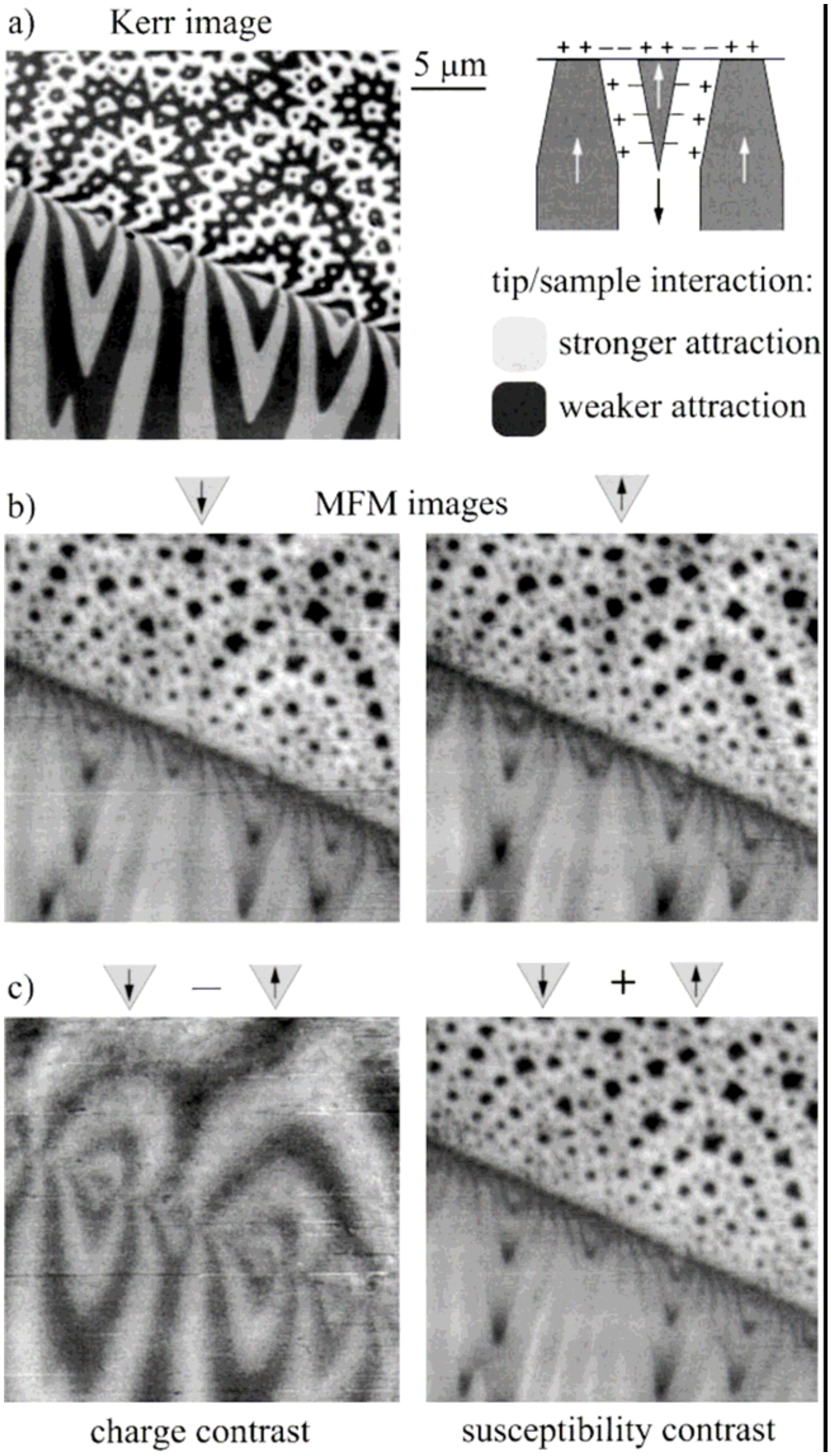

Fig. 1.11. Comparison of polar Kerr image (a) and MFM images obtained at opposite tip polarity (b) around a twin boundary on a NdFeB crystal. Charge and susceptibility contrast can be separated by difference and sum operations (c) [Zueco ’98].

1.1.4 Magnetic imaging by magnetooptical indicator films (MOIF)

As distinct from the scanning probe microscopy methods overviewed above a qualitatively different way to image the stray magnetic fields is to bring a magneto-optically active film into intimate contact with the sample and to examine it under linearly polarized light. This technique was developed mainly in relation with the studies of superconductors and is described in a number of papers and reviews (see, e.g., [Kobl.'95, Jooss '02, Atk.'95, Bend.'99])

Magnetooptic imaging is based on magnetooptic effects. Magneto-optic (MO) effects are phenomena in which an electromagnetic wave is altered due to its interaction with the magnetization in a magnetic medium. In such media, also called gyrotropic or gyromagnetic media, left- and right-rotating elliptical polarizations can propagate at different speeds, leading to a number of effects. The Faraday effect, named in honor of Michael Faraday who discovered it in 1845, is one of the MO effects, which describes the rotation of the plane of polarization of linearly polarized light during its propagation through a gyrotropic medium due to the effect of circular birefringence. The angle of the rotation of the plane of polarization obeys the equation:

$$\vartheta(\omega) = \vartheta_F(\omega) l = v(\omega) \cdot l(\mathbf{M} \cdot \mathbf{k}), \tag{2.4.1}$$

where ϑ_F – Faraday rotation, ω – circular frequency, l – path length, v – proportionality coefficient (Verdet constant), $\mathbf{M}$ – magnetization vector, $\mathbf{k}$ – wave vector. The Verdet constant is a function of the frequency of the incident light ω.

The contrast achieved between regions of different values of magnetization is a consequence of the Faraday rotation of the polarization of the incident light. In practice the measurement geometry is as shown in Fig. 1.12. The MO layer can be deposited either directly on top of the sample or onto a separate transparent substrate. A thin mirror layer of Al is usually deposited between the sample and the film to reflect the polarized light back. This has the advantage that the light passes through the MOIF twice, doubling the rotation angle.

MO measurement systems can vary considerably and Fig. 1.12 shows a particular configuration for the studies of superconductors at low temperatures [Bend.'99]. The sample sits on the cold stage of a helium cryostat in an evacuated chamber at the center of a normal solenoid whose axis is perpendicular to the sample surface illuminated from above. The image can be viewed directly or captured with a CCD camera for further processing.

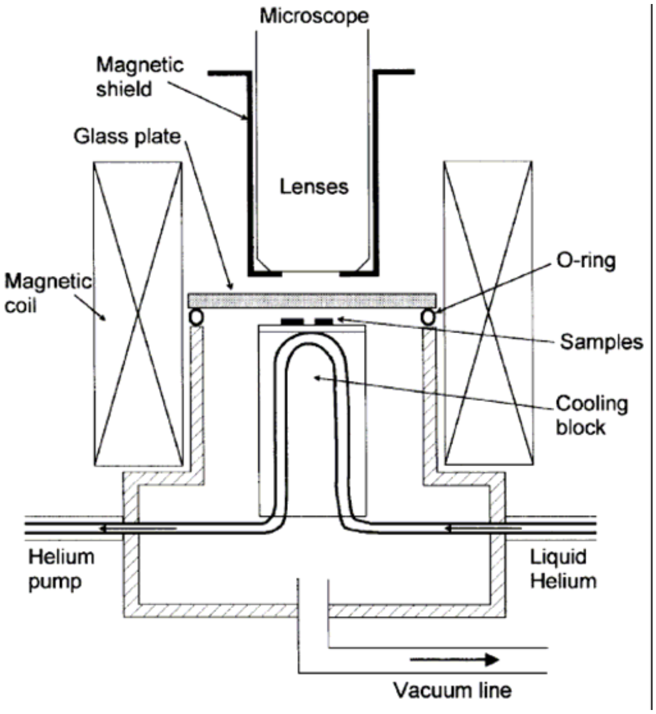

Fig. 1.12. Scheme of a typical experimental set-up for performing MO imaging at low temperatures [Bend.'99].

Until recently most MO imaging has been performed with thin films of europium chalcogenides owing to their large Verdet constants. Alloys of EuS and EuF2 have frequently been employed. More recently single component EuSe films have been used which are paramagnetic down to 4.6K.

The main drawback with the use of europium is that the Verdet constant falls rapidly with increasing temperature, and imaging is only possible below 20 K. For this reason, other MO materials have been developed to extend the temperature range.

Bi-substituted yttrium iron garnet films can be chosen with either perpendicular or in-plane anisotropy and the MO technique is then sensitive to the magnetization component along the light propagation direction. The former have characteristic labyrinth domains of up and down magnetization perpendicular to the sample plane. The changes in the domain structure (i.e. growth of one domain orientation at the expense of the others act as an indicator of stray field profiles. Spatial resolution is, therefore, limited by the characteristic domain widths ~ 5 microns.

Films with in-plane anisotropy, on the other hand, allow a direct observation of magnetic flux patterns as the magnetization vector is rotated out of the plane of the film under the influence of the magnetic field distribution.

The major advantage of YIG films is that their MO response is good all the way up to their Curie temperatures (about 800 K). The great strength of MO imaging lies in the extremely high potential rate of image acquisition.

Examples of magnetic imaging with the aid of YIG films will be given in section 2.4.

1.1.5 Summary: comparison of magnetic characterization techniques

Fig. 1.13 shows a diagrammatic plan of the current state of the art in magnetic field sensitivity and spatial resolution for six techniques, namely electron (Lorentz) microscopy, magnetic force microscopy (MFM), Bitter decoration, scanning Hall probe microscopy (SHPM), magneto-optic (MO) imaging and scanning superconducting quantum interference device (SQUID) microscopy. A measurement bandwidth of 1 Hz has been assumed (except for the ‘static’ case of Bitter decoration).

What is evident from the plot is the trade-off between field sensitivity and spatial resolution. This is well illustrated by the limiting cases of Lorentz microscopy (high spatial resolution) and scanning SQUID microscopy (high field resolution), while SHPM provides a compromise between these two. The notable exception is MO imaging which has significantly worse resolution but is nevertheless an important technique owing to its simplicity and very high intrinsic temporal resolution.

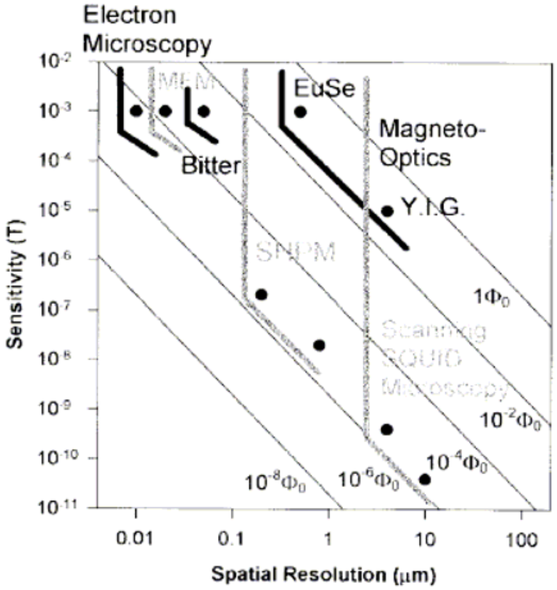

Fig. 1.13. Diagram comparing the magnetic field sensitivity and spatial resolution of electron microscopy, MFM, Bitter decoration, SHPM, MO imaging and scanning SQUID microscopy [Bend.'99].

Fig. 1.14 shows a similar diagram where the time to capture one image frame is plotted against spatial resolution. Since in many cases the limit on scanning speed is set by signal-to-noise ratios, the optimized data points in this figure generally do not correspond to those of Fig. 1.13. It is evident from this plot that the temporal resolution of MO imaging far exceeds all the other techniques although Lorentz microscopy can be performed at video rates with much higher spatial resolution. However, the latter technique suffers from the need for substantial sample preparation since very thin sections, a few tens of nanometers thick, are required to achieve adequate electron transmission. Consequently the possible introduction of artifacts and the influence of sample dimensions on the measurements are important considerations. MFM has not been widely used in the field of stray field mapping because of difficulties of extracting quantitative information. MFM tip can also be highly invasive and great experimental care must be taken during imaging. Bitter decoration is a mature technique for establishing the positions of vortices with relatively high spatial resolution (about 80 nm) but has poor sensitivity and yields very little quantitative information about vortex structures. Furthermore it has virtually no dynamic bandwidth in as much as the sample surface must be cleaned after each decoration before another experiment can be performed.

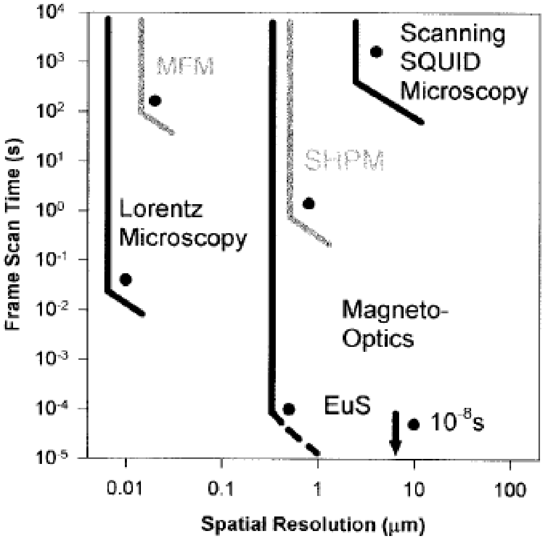

Fig. 1.14. Diagram comparing the image acquisition time and spatial resolution for five of the techniques described in Fig. 1.13 [Bend.'99].

SHPM provides a unique compromise between spatial resolution and sensitivity. Video rate imaging is likely to become possible in the near future. Moreover SHPM is perspective candidate for 3D vector mapping. MO imaging with the aid of MOIF is also a mature technology which has rather modest spatial resolution and sensitivity limited by the available MO materials and the need to bring them into intimate contact with the surface of the sample. The strength of this technique is in high-speed imaging. Scanning SQUID microscopy is the technique with the highest sensitivity while the spatial resolution is limited by current microfabrication capabilities. Existing applications considerably underutilize available signal-to-noise ratios (SNRs) and it is probable that scanning at video rates and beyond will be realized in the near future.

1.2 Diamagnetic levitation

In general levitation may be described as the state of an object when it is suspended in the gravity field without any mechanical contacts with other objects. "Suspended" here means that the position of the object is determined by stable equilibrium (in this case the levitation is called passive) or confined within a space region with no stable equilibrium position (in this case a closed-loop regulation is needed, and the levitation is called active). The forces that can oppose gravity and provide levitation may be different: buoyancy (e.g. for balloon aircrafts), air pressure (e.g. like for a paraglider lifted by an ascending air flow) and electromagnetic forces (examples are numerous, some of them will be given later).

In the case of magnetic levitation, in accordance with its name, magnetic forces are used to oppose gravity. We should distinguish two kinds of magnetic levitation when alternative and static forces are exploited. In the case of alternative forces the eddy currents induced in conductive bodies by the applied alternating magnetic field, are used to generate levitation forces. Our interest here lies in the other kind of levitation, the static one.

Magnetostatic levitation may be active or passive. For active levitation a closed-loop regulation using a feedback system is needed. Sensors providing the feedback give information on the position of the levitated body to allow the regulation system adjust the applied field in order to keep the object flying. This approach is now used for a variety of devices, from toys (e.g. levitating terrestrial globes) to active magnetic bearings and "maglev" trains. The main advantage of this approach is the ability to carry heavy loads. However, it has disadvantages lying in its very principles: a regulation system is needed, which means involving quite complex electronics, and a power supply is necessary to keep such a levitation system working.

The possibility of passive magnetic levitation was predicted in 1847 by William Thomson (Lord Kelvin), who said that a diamagnetic[1] object could be suspended in a stable equilibrium position in a static magnetic field [Thom.1847]. Ninety-two years

---

[1] Note that by saying "diamagnetic material" we mean that every component of its magnetic susceptibility tensor is negative.

after Thomson’s prediction, in 1939, Werner Braunbek experimentally showed the feasibility of diamagnetic levitation, suspending small pieces of graphite and bismuth in the field of a strong electromagnet [Braunb.’39 1]. He also introduced a term “free levitation” [Braunb.’39 2], which according to him is levitation without automatic control, in static fields and with no surrounding medium that may affect the system. He showed that a free levitation with the aid of magnetostatic, electrostatic and gravity forces is possible only if a diamagnetic body is present in one of the systems, which he investigated.

Another class of materials that has to be added to the list of diamagnetic materials is superconductors. Superconductors in an external magnetic field in fact work as perfect diamagnetic materials, for they repel all incoming magnetic flux (the Meissner effect), hence having a magnetic susceptibility equal to minus one. For comparison, the susceptibility of the best-known diamagnetic material – highly oriented pyrolytic graphite (HOPG) – is $-450\cdot10^{-6}$ (in the OOP direction). Due to the huge difference between the forces involved in levitation systems based on superconductors and systems based on diamagnetic materials, we will separate the former type of levitation systems into an individual class.

The first example of magnetic levitation with superconductors was achieved by Vladimir Arkadiev, who published an article [Arkad.’47] where he demonstrated a magnet floating above a superconductor.

Nowadays there are projects destined to exploit the levitation of superconductors for transport systems. In 2005 Ludwig Schultz and his team from IWF published an article [Schultz ’05] where they showed a cart, which could carry 240 kg above rails made of Nd-Fe-B magnets and steel. The cart could be also guided along the rails.

Levitation of superconductors (or above superconductors) shows prospects for practical applications but it has the serious drawback that superconductors have to be constantly cooled. Because of this requirement, applications of this kind of levitation are hardly imaginable for microsystems. From now on we will speak about levitation with the aid of diamagnetic materials, which we will refer as “diamagnetic levitation”.

The detailed history of diamagnetic levitation is given in the article by Gerald Küstler [Küst.'07]. Here we will present some brief history and remarkable achievements.

In 1956 A.H. Boerdijk published an article about different technical aspects of diamagnetic levitation [Boer.'56]. In this paper he also repeated Braunbek's experiments on levitation of pieces of graphite but using permanent magnets instead of electromagnets.

We will separate two cases of magnetic levitation: the levitating part is (i) a diamagnetic object, and (ii) a magnet. The free levitation of the second kind is much more difficult to achieve, for magnets are much denser and hence heavier than typical diamagnetic materials used for levitation.

Boerdijk was also the first who achieved levitation of a permanent magnet above graphite [Boer.'56/57]. To do this he used a second, much larger magnet fixed at a relatively large distance from the flying magnet. The distance was chosen so that the attractive force between the levitated magnet and the fixed magnet almost compensated the gravity force. Then a piece of graphite placed under the levitated magnet generates a repulsive force, which prevents the magnet from dropping. Note that this system would be unstable without the diamagnetic object: the free magnet would either fall down if the distance from the fixed magnet was too large or it would be attracted and stuck to the fixed magnet if the distance was too small.

Note that due to the fixed compensating magnet the levitating one in Boerdijk's system was not free to move along the plane of graphite, which limits the applications of the system. Ronald E. Pelrine 1992 was the first who succeeded in getting rid of the compensating magnet with the aid of strong Nd-Fe-B magnets. He levitated an array of four magnets assembled with alternating magnetization in a square (chessboard-like) configuration above a sheet of HOPG [Pelr.'92]. In 2008 Harald Profijt and his co-authors published an article where they levitated a double-dipolar magnet (collage of two halves magnetized alternately) [Prof.'08]. And to our knowledge the first who succeeded to levitate a single unidirectionally magnetized magnet above HOPG without a supporting magnet was Jaap Kokorian and his workmates in December 2008 [Kokor.'09].

Levitation of diamagnetic objects above magnets has been much wider investigated than the levitation of magnets or arrays of magnets above diamagnetic substrates. To date its applications have been quite numerous. The first class of application was found in diamagnetically stabilized bearings. Contactless suspension of a rotating part solved the main problem of bearings: losses by friction and heating. The first such device was patented in 1952 by Erich Steingroever; in his system a levitating rotor was used in a kilowatt-hour meter [Steing.'52].

In 60th -70th a verity of devices based on diamagnetic levitation was constructed. Description and characteristics of many of them can be found in the review article by Ponizovskii [Poniz.'82]. Here we will briefly mention some of the devices.

R.D. Waldron constructed a magnetic bearing that was a pyrolytic graphite ring attached to a light acryl ring suspended in a field generated by a system of Alnico PM. The useful load of the bearing was 2.91 g [Wald.'66]. R. Evrard and G.J. Boutry designed a high-precision micro-manometer using a magnetically suspended graphite disc. It could measure the gas pressure with a threshold sensitivity of 10^{-10} torr [Evr.'69]. V.B. Braghinskii constructed a high-precision electrometer for experiments on searching of free (isolated) quarks [Brag.'70]. I. Simon patented a 1D accelerometer, which was a graphite rod suspended in an axial gap of a cylindrical permanent magnet [Simon '69]. Its displacement was measured optically. The damping of the rod was realized due to the interaction between eddy-currents induced in the rod and the magnetic field generated by the magnet. Similar design was used in a high precision tiltmeter (output sensitivity 9 µA per angular second) [Simon '68]. V.B. Braghinskii and V.I. Osika constructed a measurer of moment of force [Brag.'69]. The device was based on a graphite ring suspended in a field of an electromagnet. The authors claim that the device can measure the moment of force acting on the ring or on a load placed on the ring with a precision of 10^{-15} N·m.

During the last two decades the variety of materials of levitated objects was notably supplement.

In 1991 E. Beaugnon and R. Tournier succeeded to levitate water and other diamagnetic liquid and solid substances in a high magnetic field generated by a superconducting electromagnet [Beaug.'91]. In 2000 Michael Berry and Andrey Geim were awarded with an IgNobel prize for their work on making a frog fly [Geim '97].

These days levitation in strong magnetic fields finds applications in weightless fluid dynamics [Beaug.'01] and containerless crystal growth [Poodt '05],

Due to reduction scale laws[1], the smaller the levitated object the more dominating the diamagnetic force becomes over gravity. It makes diamagnetic levitation favorable for microsystems. Several applications of levitation for microsystems were recently demonstrated.

Igor Lyuksyutov and his colleagues presented a levitation device for the high precision manipulation of floating diamagnetic femto-droplets [Lyuks.'04]. Later Hishem Chetouani et al. [Chet.'07] reported on diamagnetic levitation of living cells over topographically micropatterned film magnets[2] and later Christian Pigot and his colleagues used similar magnets to levitate solid diamagnetic micro-objects [Pigot '08]. They also demonstrated a way of manipulation of the levitated particles by a laser beam.

Film magnets have great potential for micro-systems exploiting the principles of diamagnetic levitation. The distributions of the magnetic field and field gradient required to generate the diamagnetic force, depend on the magnetic properties of the magnets and their magnetization pattern. Hence, development of levitation microsystems demands tools of local quantitative characterization of the magnetic field distributions generated by the micro-magnets.

---

[1] The scale reduction laws will be explicitly given in section 4.2

[2] For more details about topographically patterned film magnets see annex I.

CHAPTER 2: LOCAL CHARACTERIZATION OF THE STRAY FIELDS PRODUCED BY MICROMAGNETS

2. Local characterization of the stray fields produced by micromagnets

2.1 Introduction

The great potential for use of magnets in micro-systems has stimulated much effort in the preparation of magnets at the micron scale [Demp.'09]. The assessment of these micro-magnets, in particular the characterization of the stray magnet fields produced by them, should prove invaluable for the optimization of material processing as well as micro-system design. The development of methods for stray field characterization constitutes the core of this thesis work. Three tools have been used, 1) analytical calculations, 2) scanning Hall probe microscopy and 3) magneto-optic microcopy. Analytical calculations are used to simulate the field patterns produced at a given distance above the micro-magnet arrays, as a function of the geometry of the individual micro-magnets and the overall micro-magnet arrays as well as the direction of magnetization of the individual micro-magnets. The calculated field patterns are then used to analyze the experimental results achieved with scanning Hall probe microscopy and magneto-optic microcopy.

In this chapter the basic ideas behind the analytical calculations will be explained and results for some test magnet geometries will be presented. Concerning scanning Hall probe microscopy, the experimental set-up will be presented and the probe calibration procedure will be described. Measurement of a sample's surface topography and tilt, as well as the Hall-cross to sample distance will be shown. Test results will be presented for each case. Finally, a novel method for the measurement of the 3 spatial components of the stray field, using a single component probe, will be presented, together with test results. Concerning magneto-optic microcopy, the use of magneto-optic indicator films for the characterization of tantalum-capped micro-magnets will be presented. Test results will be shown to demonstrate the use of both planar and uniaxial MOIF for the qualitative and quantitative characterization of the stray field patterns produced by micro-magnets. Details concerning the fabrication of the micro-magnets studied here are given in annex 1.

2.2 Analytical calculations of magnetic field distributions

The work described in this section was done in collaboration with Prof. Rostislav Grechishkin (Lab. of Magnetoelectronics, Tver State University, Russia).

Here we will deal with a straightforward field calculation of basic permanent magnet configurations. Following the article of Erlichson [Erl.'89] we use derivations based only on the most fundamental laws (those of Biot-Savart and Coulomb) and numerical integration (when necessary). As will be seen, the solutions may be simple but cover many practical cases, including some rather exotic permanent magnet designs.

A favorable feature of modern rare-earth type permanent magnets is that due to their very high anisotropy field ($\mu_0 H_a$ = 10-40 T) and coercive force ($\mu_0 H_c$ > 1.5 T), the residual magnetization vector, $\mu_0 M_r$, is strongly fixed to the easy axis of magnetization. This model, which assumes rigid magnetization patterns, is also applicable to thin Nd-Fe-B film magnets since they are highly coercive and strongly out-of-plane textured [Demp.'07] (i.e. the film's magnetization may be considered to remain uniform, even in the presence of large demagnetizing fields, although the induction may be non-uniform). This rigidity of magnetization also allows the application of superposition principles for systems composed of many elements. In fact, rare-earth magnets are nearly ideal models of uniformly magnetized bodies as represented by surface Amperian currents[1] forming an equivalent solenoid. Thereby, the Biot-Savart law is applicable to the calculation of the field of such a body. The same body may be alternatively represented by magnetic poles (charged surfaces). This approach, for example, is used in the calculation tool MacMMems [Rak.'06], which is also used in this work.

---

[1] The illustration of a magnetized *cylinder* with molecular currents cancelling each other inside the body and leaving uncompensated surface currents is recurring in textbooks, perhaps from the times of Ampere. However, for a *cylinder*, in contrast to an *ellipsoid,* this representation was not justified before the advent of high-coercivity materials, because older types of permanent magnets are characterized by $\mu_0 H_C < \mu_0 M_r$, hence in an open magnetic circuit the cylinder's self-demagnetizing field disturbs the magnetization thus giving rise to *volume* currents in addition to surface ones.

In this section we will give an example of using the Amperian current model to calculate the magnetic field generated by a magnet with the shape of a tetragonal rectangular prism, for, in fact, all the magnetic configurations mentioned in this work can be approximated by a combination of such prisms. Examples of using the Amperian current model, and also the model of charged surfaces, for other magnetic configurations, as well as the comparison of the two approaches, are given in annex II.

2.2.1 Basic relations

To avoid ambiguity below we write the basic relations (in SI units) as they will be used here.

The magnetic field due to a linear current element I**d**$\mathbf{l}$ at a distance $\mathbf{R}$ from it is given by the Biot-Savart law:

$$d\mathbf{B} = \frac{\mu_o I}{4\pi}\frac{\left[d\mathbf{l}\times\mathbf{R}\right]}{R^3}. \tag{2.2.1}$$

In the coordinate form the cross product [d**l** × **R**] is given in an obvious notation by:

$$[d\mathbf{l}\times\mathbf{R}] = \mathbf{i}\begin{vmatrix} dl_y & dl_z \\ R_y & R_z \end{vmatrix} - \mathbf{j}\begin{vmatrix} dl_x & dl_z \\ R_x & R_z \end{vmatrix} + \mathbf{k}\begin{vmatrix} dl_x & dl_y \\ R_x & R_y \end{vmatrix}. \tag{2.2.2}$$

The total flux density (magnetic induction) in the magnetized medium is given by:

$$\mathbf{B} = \mu_0(\mathbf{H} + \mathbf{M}), \tag{2.2.3}$$

the direction of the vector of equivalent current density $\mathbf{I}_m$ (in A m^{-1}) at the media interface will be defined by the cross product:

$$\mathbf{I}_m = [\mathbf{M}_1 - \mathbf{M}_2] \times \mathbf{n}, \tag{2.2.4}$$

where $\mathbf{n}$ is the normal directed from the medium with magnetization $\mathbf{M}_1$ toward the medium with $\mathbf{M}_2$ ($\mathbf{M}_2 = 0$ in vacuum).

In a permanent magnet the residual magnetization, $\mu_0\mathbf{M}_r$, is by definition equal to the residual induction (remanence), $\mathbf{B}_r$. The latter parameter commonly serves to characterize permanent magnet materials and will be used in here.

2.2.2 Rectangular current turn and thin solenoid

To arrive at a magnet of prismatic shape we have to calculate the field generated by a rectangular current turn. Its schematic diagram is presented in Fig. 2.1.

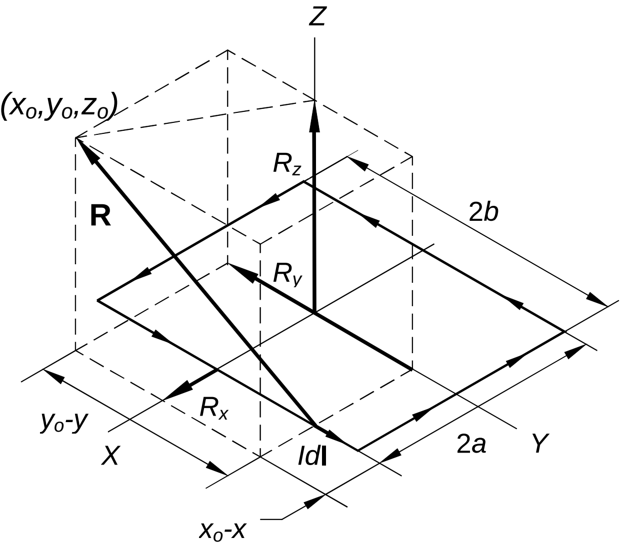

Fig. 2.1. Diagram for the rectangular current turn.

From the Biot-Savart law (2.2.1) and the cross-product expression (2.2.2), it follows that:

$$dB_x = \frac{\mu_o I}{4\pi R^3} dl_y R_z \,,\ dB_y = \frac{\mu_o I}{4\pi R^3} dl_x R_z \,,\ dB_z = \frac{\mu_o I}{4\pi R^3}(dl_x R_y - dl_y R_x) \,, \quad (2.2.5)$$

while $R^2 = (x_0\text{-}x)^2+(y_0\text{-}y)^2+(z_0\text{-}z)^2$.

Integrating (2.2.5) over the sides of the turn from -*a* to *a* and -*b* to *b,* followed by integration over the height 2*h* of a thin solenoid based on this turn, one obtains simple expressions in terms of elementary functions as follows:

$$dB_x = -\frac{\mu_o}{4\pi}\frac{I}{2h}\left[\left(\int_{-h}^{h}\frac{\beta(z_o - z)\,dz}{\left[\alpha^2 + (z_o - z)^2\right]\sqrt{\alpha^2 + \beta^2 + (z_o - z)2}}\right)_{\alpha_1}^{\alpha_2}\right]_{\beta_1}^{\beta_2},$$

$$B_x = -\frac{\mu_o}{4\pi}\frac{I}{2h}\left\{\left[\left(\ln\left(\beta + \sqrt{\alpha^2 + \beta^2 + \gamma^2}\right)\right)_{\alpha_1}^{\alpha_2}\right]_{\beta_1}^{\beta_2}\right\}_{\gamma_1}^{\gamma_2}. \quad (2.2.6)$$

$$B_y = -\frac{\mu_o}{4\pi}\frac{I}{2h}\left\{\left[\left(\ln\left(\alpha + \sqrt{\alpha^2 + \beta^2 + \gamma^2}\right)\right)_{\alpha_1}^{\alpha_2}\right]_{\beta_1}^{\beta_2}\right\}_{\gamma_1}^{\gamma_2}. \quad (2.2.7)$$

$$B_z = -\frac{\mu_o}{4\pi}\frac{I}{2h}[(\int_{-h}^{h}\frac{\alpha\beta\,dz}{[\beta^2+(z_o-z)^2]\sqrt{\alpha^2+\beta^2+(z_0-z)^2}} +$$

$$+\int_{-h}^{h}\frac{\alpha\beta\,dz}{[\alpha^2+(z_o-z)^2]\sqrt{\alpha^2+\beta^2+(z_0-z)^2}})_{\alpha_1}^{\alpha_2}]_{\beta_1}^{\beta_2} =$$

$$= -\frac{\mu_o}{4\pi}\frac{I}{2h}\left\{\left[\left(\arctan\frac{\gamma\sqrt{\alpha^2+\beta^2+\gamma^2}}{\alpha\beta}\right)_{\alpha_1}^{\alpha_2}\right]_{\beta_1}^{\beta_2}\right\}_{\gamma_1}^{\gamma_2}, \qquad (2.2.8)$$

α, β and γ stand for the limits of definite integrals implying that:

$$\left\{\left[\left(f(\alpha,\beta,\gamma)\right)_{\alpha_1}^{\alpha_2}\right]_{\beta_1}^{\beta_2}\right\}_{\gamma_1}^{\gamma_2} = f(\alpha_2\beta_2\gamma_2) - f(\alpha_1\beta_2\gamma_2) - f(\alpha_2\beta_1\gamma_2)$$

$$+ f(\alpha_1\beta_1\gamma_2) - f(\alpha_2\beta_2\gamma_1) + f(\alpha_1\beta_2\gamma_1) + f(\alpha_2\beta_1\gamma_1) - f(\alpha_1\beta_1\gamma_1),$$

where $\alpha_{1,2} = x \pm a, \beta_{1,2} = y_o \pm b, z_{1,2} = z \pm h$ (+ and - signs apply to subscripts 1 and 2, respectively).

Fortunately it was possible to perform triple integration in the above derivation in closed form, hence the expressions (2.2.6)-(2.2.8) are exact[1].

2.2.3 Tetragonal prismatic magnet: axial and inclined magnetization

Now knowing the formulas for a thin solenoid of rectangular shape, we can calculate the field generated by a tetragonal prismatic magnet. A scheme representing the axially magnetized tetragonal prism by currents is given in Fig. 2.2 (a).

In fact the rectangular solenoid formulas (2.2.6) - (2.2.8) are ready for use immediately after replacing $\mu_o I/2h$ by the remanence B_r. The model also describes the case of magnetization inclined with respect to the prism edges. A specific case of **M** rotated by an angle α in the *ZY* plane is illustrated in Fig. 2.2 (b). Two superimposed solenoids with orthogonal magnetization directions are adequate for the description of this case provided appropriate equivalent current values are ascribed to each of them.

---

[1] summation formula acrtan x – acrtan y = acrtan $[(x-y)/(1+xy)]$ ($x>0$, $y>0$) is helpful when folding the final expression (2.2.8) for B_Z.

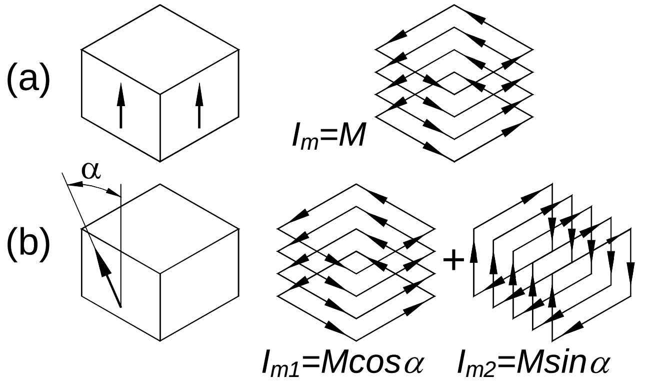

Fig. 2.2. Representation of prismatic magnets (left column) by Amperian currents (right column).

The formulas (2.2.6) - (2.2.8) were programmed in Python and used in our work to calculate the fields generated by single prismatic magnets and arrays of prismatic magnets.

2.3 Scanning Hall probe microscopy

2.3.1 Scanning Hall probe microscope set-up

The scanning Hall probe microscope (SHPM) was recently constructed by Piotr Laczkowski and Danny Hykel, under the supervision of Dr. Klaus Hasselbach (MCBT Department, Insitut Néel). It was designed to measure distributions of the magnetic field component perpendicular to the sample stage at a certain distance from the sample surface. Since most of the measured samples were films, we will call this component the out-of-plane (OOP) component (or alternatively the Z-component). In section 2.3.6 the possibility to measure all three components of magnetic field with a small modification of the SHPM will be described.

A schematic diagram of the SHPM is shown in Fig. 2.3. The measurement device consists of four principal blocks: (i) a motorized XYZ-stage for sample positioning, (ii) a contact detection system, (iii) a real-time sample stage height regulation and (iv) a magnetic field detection system.

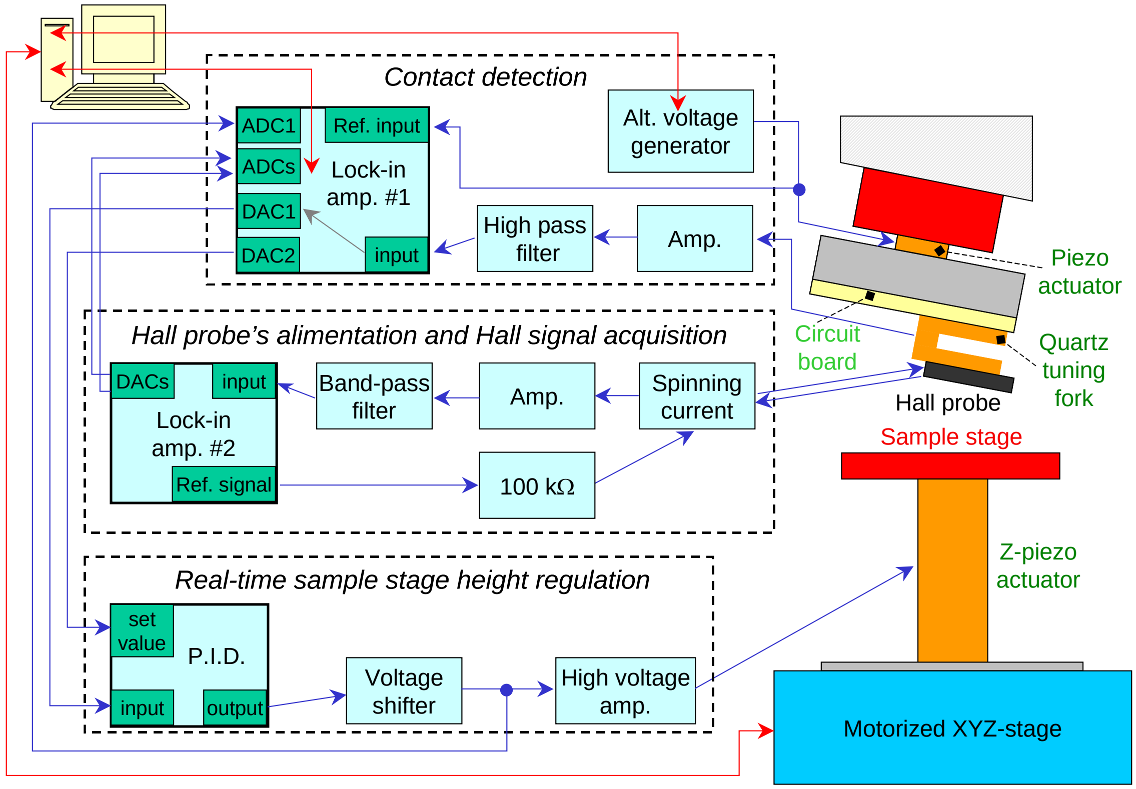

Fig. 2.3. Schematic diagram of the SHPM set-up.

(i) XYZ-stage for sample positioning

The motorized XYZ-stage allows the controlled movement of the sample stage in three directions (x, y, z) with a spatial resolution of 0.1 µm. The Z-motor (Micos MT-40) is used for changing the probe-sample distance while the X- and Y-motors (Micos PLS-85) allows the sample to be scanned in the plane perpendicular to the Hall probe's sensitive axis. This XYZ stage is used for initial sample positioning and for the control movement of the sample with respect to the Hall probe. All the motors are controlled with the aid of a computer program. Note that the sample stage is fixed to the XYZ stage via a piezo actuator that can move the sample stage in the Z direction.

(ii) Contact detection

Together with the sample stage height regulation system (described below), the contact detection system allows the device to work in the so-called 'contact mode'. In this mode the probe chip remains in contact with the sample surface while scanning, in spite of the sample topography and/or tilt. The contact detection method is based on a commercial quartz tuning fork (6 mm long, 0.5 mm wide quartz watch crystal), in a way similar to that used in the design of a SQUID force microscope [Hassel.'08]. When oscillations are excited in the tuning fork, a voltage appears on its sides due to the piezoelectric effect. The voltage induced on the tuning fork near its resonance frequency decreases when the probe chip stuck to it approaches close to the sample surface, because of a shift in the tuning fork's resonance frequency due to the changing environmental conditions. The same methods used to describe the oscillation processes of AFM tips [Binn.'86] can be applied to describe the oscillator used in our work. Technically, the realization of the method is the following. The Hall probe chip is stuck to the tuning fork which is in turn glued onto a circuit board, which serves as a base for electrical connections of the Hall sensor and tuning fork. The circuit board is screwed to an aluminium block. A piezo actuator (Staveley Sensors Inc.) is glued onto this block from one side and onto a copper support from the other side. This piezo actuator is used to excite vibrations in the tuning fork. Thanks to the piezoelectric effect, the quartz tuning fork transduces the vibrations into an electrical voltage. This signal is amplified and then passes through a high-pass filter (cutoff frequency = 40 kHz) into a lock-in amplifier (“lock-in #1”; Signal Recovery 7220 DSP). A sine voltage generator with an adjustable frequency and amplitude (Yokogawa FG 200) is used to excite the vibrations in the piezo actuator. This signal is also supplied to the reference input of lock-in #1. The induced voltage amplitude for the “free” tuning fork is recorded and serves as an input for the real-time adjustment of the sample stage height, using the Z piezo actuator.

(iii) Real-time adjustment of the sample stage height

As mentioned above, the sample stage is attached to the motorized XYZ-stage via a piezo-actuator (PICMA P-885.90), the vertical position of which can be varied in the range of 30 μm, depending on the applied voltage (from 0 to 120 V). The voltage is regulated by a closed-loop analogue PID[1] (proportional–integral–derivative) control. The amplified amplitude of the signal from the tuning fork is supplied to the input of the PID. The previously recorded value of voltage amplitude for the free tuning fork is supplied as a set value, using one of the DAC outputs of lock-in #1. The bipolar output signal from the PID goes through a voltage shifter and then to a high voltage amplifier[1] with the amplification of 10, which accepts only a unipolar input signal (because of the unipolarity of the piezo-actuator). The height of the piezo actuator depends on the applied voltage almost linearly (actually the dependence has a hysteretic behaviour, as will be discussed later). The SHPM is thus able to register topographical images of the sample surface. To do this, the output signal from the PID, which in fact defines the voltage applied to the piezo actuator regulating the height of the sample stage, is supplied to an ADC input of lock-in #1. To avoid the influence of external vibrations on the stage’s height regulation process, the measuring device is placed on a vibration isolation table.

(iv) Magnetic field detection system

The key component of the magnetic field detection system is a second-generation quantum-well Hall probe based on a 2D electron gas (2D-EG) (provided by Vincent

---

[1] provided by M. Grollies and J.L. Bret from the electronic service of the MCBT department, Institut Néel

Mosser, Itron France) [Pross '05]. The probe contains three Hall crosses of active area size around 4×4, 10×10 and 40×40 μm^2 (Fig. 2.4). Each of these is sensitive to the component of magnetic field perpendicular to the probe plane. Only one of them at a time is used for measurements. The signal from the Hall probe is measured using a lock-in amplifier. The Hall probe is supplied with an alternating current. For this it is connected in series with a resistor (100kΩ) to an alternating voltage supply, which is in fact the reference signal from a second lock-in amplifier ("lock-in # 2"; Signal Recovery 7265 DSP). The frequency of the supply voltage corresponding to the minimum value of the final output signal noise was found empirically to be 987 Hz. The powering of the probe and measurement of the Hall voltage is carried out through a spinning-current device[1]. The spinning current technique is one of the most efficient methods for offset reduction in Hall devices, its principle can be found elsewhere [Stein.'98]. After amplification, the Hall voltage passes through a band-pass filter[2] with an adjustable frequency band, and then it is fed to the input of the lock-in # 2. The amplification gain can be either 10^2, 10^3, or 10^4. Together with the input signal voltage and the lock-in amplifier's measurement range, it determines the final measurement error of the device and the maximum measurement field, and must be chosen according to the expected magnetic field generated by the sample under investigation. The Hall voltage measured by lock-in #2 is sent to a computer where it can be recorded.

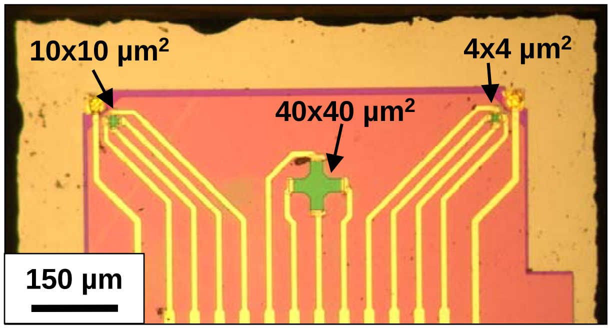

Fig. 2.4. Plan-view image of the Hall probe containing three active areas.

---

[1] provided by D. Lepoittevin from the electronic service of the Nano department, Institut Néel

[2] provided by M. Grollies and J.L. Bret from the electronic service of the MCBT department, Institut Néel

All the measurement parameters are fixed using a set of computer programs written in LabVIEW and a computer program also controls the process of scanning and recording the data. To minimize the probability of problems with external device / computer communication, only one of the used lock-in amplifiers ("lock-in #1") communicates with the computer. On account of this, the Hall signal (its in-phase component and its phase) measured using lock-in # 2, goes to the computer via two DAC outputs of lock-in # 2 and then the ADC inputs of lock-in # 1.

2.3.2 Probe calibration procedure

Calibration solenoid

The probe was calibrated in the magnetic field generated by the solenoid shown in Fig. 2.5. The parameters of the solenoid are the following: inner radius = 15.0 cm, outer radius = 25.4 cm, height = 3.6 cm; turns per layer = 13, number of layers = 36, diameter of wires = 0.28 cm, total length of the wire = 0.6 km. The constant of the solenoid at its center was calculated to be 16.85 G/A (or 1.685 mT/A).

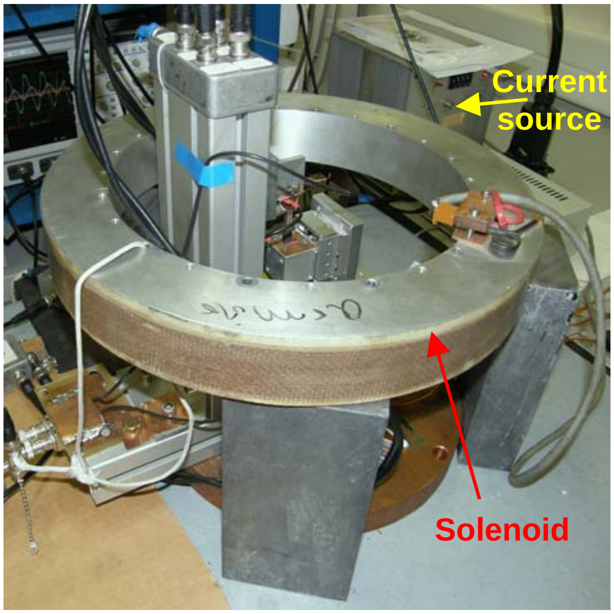

Fig. 2.5. Photo of the solenoid used for the calibration of the Hall probe. The Hall probe is at the center of the solenoid.

The field of the solenoid was then measured using a calibrated Hall gaussmeter. The field at the center of the solenoid was measured for a set of values of the current flowing in the solenoid (from -4 to 4 A). Then the measured points were fitted with a straight line (Fig. 2.6). Taking into account measurement errors, the constant of the solenoid at its center was estimated to be 16.83±0.25 G/A (or 1.683±0.025 mT/A), which is in a very good agreement with the calculated value (16.85 G/A).

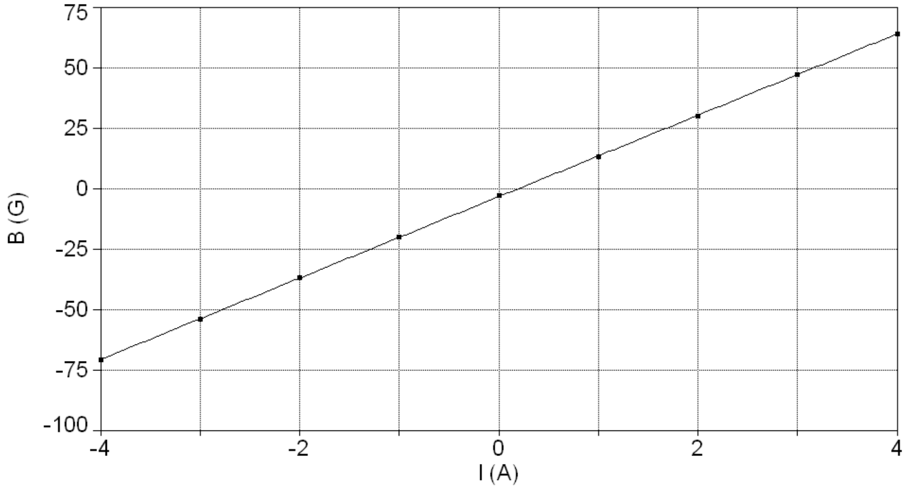

Fig. 2.6. Calibration graph for the solenoid.

To estimate the size of the region in the vicinity of the center of the solenoid where the generated field may be considered as homogenous, the field was calculated along the radius of the solenoid at the height equal to half of its total height. Note that only the component of the field parallel to the solenoid's axis is of interest. Fig. 2.7 shows the calculated axial component of the magnetic field versus the radius.

The field homogeneity is better than 5% and 1% in the central regions of diameter 3 cm and 1 cm, respectively. This allows this solenoid to be used for calibration purposes without having precise mechanisms for adjusting the position of the probe in the solenoid during calibration.

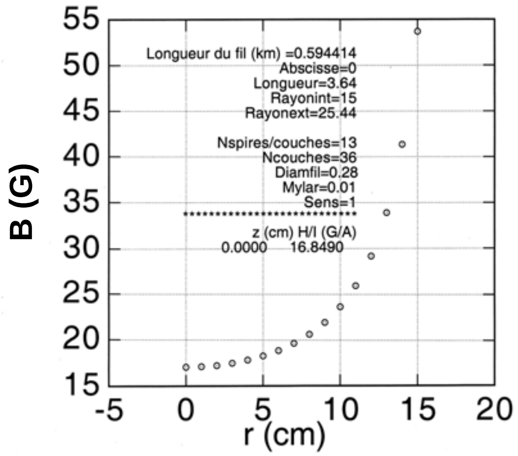

Fig. 2.7. Calculated axial component of the magnetic field generated by the calibration solenoid versus its radius at the center of its height.

Calibration of the Hall probe

The used probes were calibrated by measuring the Hall response in a known field generated by the calibrated solenoid described above. During the calibration procedure, the field measurement settings were fixed at the following values: Hall probe feeding current = 3 V / 100 kΩ = $3\cdot10^{-5}$ A, feeding current frequency = 987 Hz, amplification gain = $1.0\cdot10^{3}$, filter pass band = [$1.0\cdot10^{2}$, $1.0\cdot10^{4}$ Hz].

As mentioned in the previous section, the amplified and filtered Hall response signal is measured using a lock-in amplifier. The operation features of a lock-in amplifier are recalled in annex III. The magnitude of the output signal is given by $M = \sqrt{U_x^2 + U_y^2}$, where U_x and U_y are the in-phase and out-of-phase components of the output signal, respectively. Since the magnitude is proportional to the RMS value of the input signal, it does not contain information about the sign of the input signal. However, the sign of the signal may be deduced from either the in-phase or out-of-phase component.

To convert the measured Hall voltage into a magnetic field value, we used a coefficient k (the coefficient inverse to the Hall sensitivity (U/B) for a given feeding current):

$$k = \frac{B}{U_x},$$

where B is the measured field and U_x is the in-phase component of the lock-in output signal. The initial phase shift was set to zero in a high magnetic field in order to make the modulus of U_x almost equal to the value of the output signal magnitude. The calibration graph for the 40×40 μm^2 probe is presented in Fig. 2.8. The figure shows the Hall response versus the current in the calibration solenoid. It can be seen that a straight line approximates the measured points with a very good precision. Note that the calibration was done without the spinning current device, for it was out of service. Knowing the slope of the calibration line (42.44 mV/A ± 0.35%) and the constant of the solenoid (1.685 mT/A ± 1.5%) the coefficient k was estimated to be 39.7 mT/V ± 1.9%. In the same manner the coefficient k for the 4×4 μm^2 cross was estimated to be 48.5 mT/V ± 2.6%.

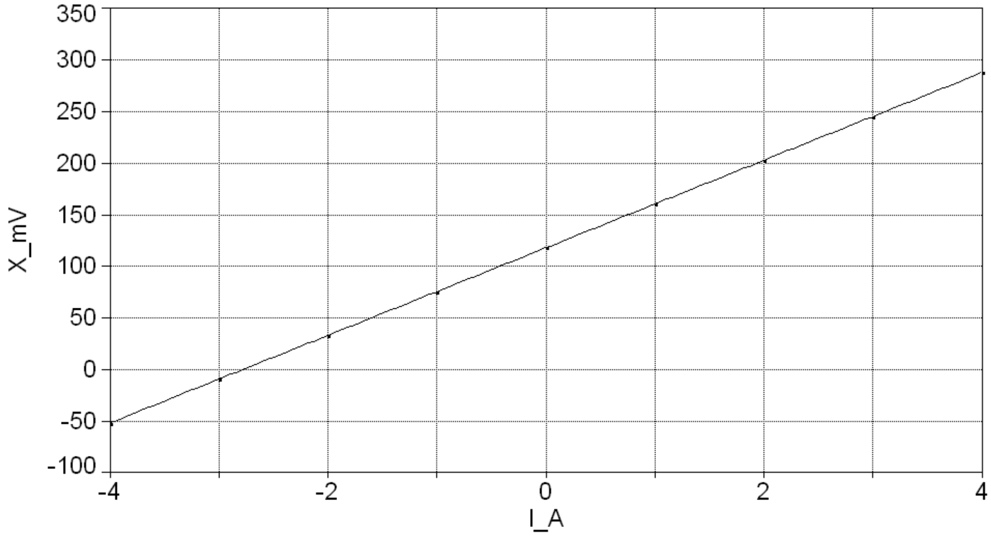

Fig. 2.8. Hall response measured with a lock-in amplifier (the in-phase component) vs. the current in the calibration solenoid for the 40×40 μm^2 probe.

The magnetic field resolution of the probe is determined by its output signal noise, which depends on the size of the active area: the smaller the size the larger the noise. Even for the smallest Hall cross the field resolution was estimated to be far better than 10 $\mu T/Hz^{0.5}$; but taking into account the system noise during scanning, the final magnetic field accuracy of the measuring device was about 60 μT (for the smallest Hall cross, at the frequency 987 Hz and the time constant 5 ms). Note that this value is much smaller than the typical values of the magnetic field generated by the measured samples (around 10 mT).

Hall probe sensitivity to ambient lighting

It was noticed that the sensitivity of the probe, when it was screened from light, and when it was not screened (i.e. when the calibration is made under the illumination of overhead lighting) differed by around 5% (the measurements were done without the spinning current device). Moreover, some variations of the signal were observed when someone was partly screening the probe from light when passing by the device. Therefore to avoid variations of the sensitivity, the SHPM was screened from light with a non-transparent cardboard box whenever a scan or a calibration was being carried out. When screened, the variation of the probe's sensitivity did not exceed the confidence interval of sensitivity measurements (around 2%).

2.3.3 Measurement of sample surface topography and tilt

As it was mentioned before, the SHPM can measure not only magnetic field distributions but also it can give information about the topology and the tilt of the surface of a sample being investigated. When the device is working in the "contact mode", the probe follows the sample's surface thanks to the piezo actuator that adjusts the height of the sample stage. The height of the piezo actuator depends on the applied voltage, which is regulated by a closed-loop PID control in which the amplified magnitude of the signal from the tuning fork is supplied to the input of the PID (see section 2.3.1). Fig. 2.9 shows the displacement of the Z stepper motor, which was necessary to keep the probe in contact with the sample while changing the voltage applied to the piezo actuator (the displacement was chosen to be zero when the applied voltage is maximum). In fact the graph shows how the actuator's height depends on the applied voltage. A hysteretic behavior can be observed. In the middle of the voltage range (around 70 V) the difference between the corresponding points on the "back" and "forth" scans is around 3 μm. This value determines the uncertainty of the topographical measurements where the height–voltage dependence is approximated with a straight line and used as a calibration line to convert volts to micrometers. Note that this considerable hysteretic behavior of the height–voltage dependence does not affect the regulation in the "contact mode". Since the regulation is closed-loop, the voltage applied to the piezo actuator is adjusted constantly during scanning, based on whether the probe is touching the sample surface or not.

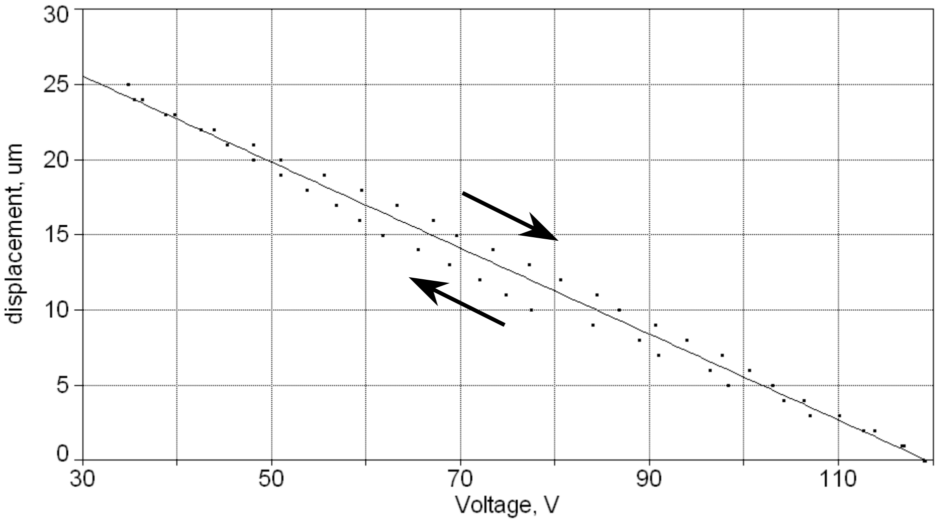

Fig. 2.9. Displacement of the Z stepper motor, necessary to keep the probe in contact with the sample stage while changing the voltage applied to the piezo actuator. The solid line represents the approximation of the data points with a strait line with a slope of – 0.286 μm/V.

Test measurement of sample surface topography

As an example of a topographical profile, a profile of a circuit board is presented in Fig. 2.10 (a). The probe was touching the board's surface along the line indicated in Fig. 2.10 (b). Note that the probe could not reach all the way down between the two circuit traces, since the probe's chip itself has a considerable size (4×1×0.5 mm^3) and hardly resembles a tip used for AFM measurements. Therefore the SHPM cannot be considered for topographical imaging of micron-sized features, but topographical imaging can be used to correct for the sample's tilt and to find the sample's edges, which can be useful for some cases that will be presented later.

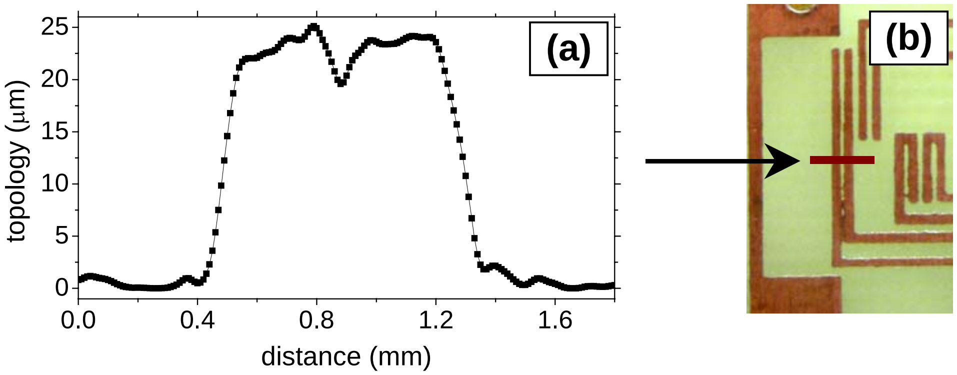

Fig. 2.10. Topographical profile of a circuit board (a) along the red line indicated on the top-view optical image of the board (b).

2.3.4 Estimation of the Hall-cross to sample distance

The probe is slightly inclined with respect to the sample stage (Fig. 2.11 (a)) for two reasons: (i) to prevent damage to the Hall crosses by contact with the sample and (ii) to prevent detachment of the gold wires from the bottom side of the probe by contact with the sample. The inclination angle is typically around 5°. In many cases the angle can be considered small enough to assume that the measured signal to be proportional only to the out-of-plane component of the sample's stray magnetic field. The question of the contribution of the in-plane component of the stray field to the measured signal will be discussed further in this section. The inclination angle together with the distance between the edge of the probe and the center of the Hall cross determine the distance between the Hall cross and the surface of the sample being measured. Note that even if the sample surface may be considered flat it may not be necessarily parallel to the sample stage. In general it may have a tilt "α" around the OY axis and "β" around the OX axis (Fig. 2.11 (c)). While the former (α) is taken into account automatically if we measure the inclination angle between the probe and the sample surface (and not between the probe and the sample stage), the latter (β) must be measured independently. Knowing the angles α and β and the distances between the center of the Hall cross and the corresponding edge of the probe, l_1 and l_2, we can calculate the Hall cross – sample distance using the following equation:

$$d\,[\mu\text{m}] = l_1 \sin\alpha + (1000 - l_2)\sin\beta\cos\alpha\text{, for } \beta > 0\text{, and}$$

$$d\,[\mu\text{m}] = l_1 \sin\alpha + l_2 \sin\beta\cos\alpha\text{, for } \beta < 0,$$

where 1000 is the width of the Hall probe's chip in µm. For the 40×40 µm^2 active area these two formulas are equivalent, because l_2 = 500 µm (Fig. 2.11 (b)).

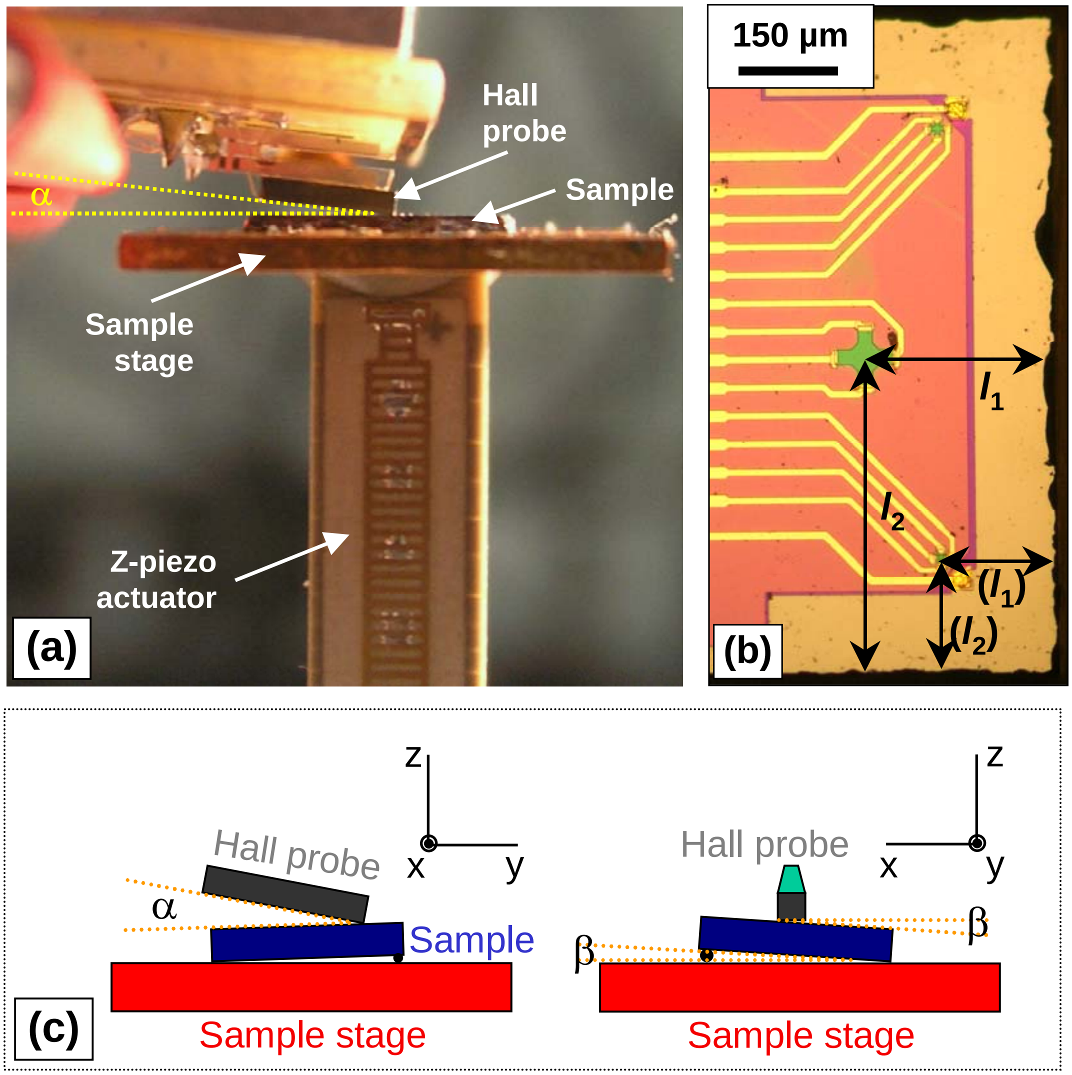

Fig. 2.11. (a): Hall probe and sample position in the set-up; (b): distances from the Hall cross to the probe's edges; (c): schematic illustration of the probe's tilt.

Note that for all non-zero values of β, the Hall-cross to sample distance only increases. Assuming β to be zero, let's estimate the minimum Hall cross – sample distance (hereafter, by "Hall cross – sample distance" we mean the distance between the center of the Hall cross and the upper surface of the sample). The distance l_1 for the 40×40 µm^2 Hall cross is 284 µm (Fig. 2.11 (b)). The minimum realistically achievable tilt of the probe is around 4°, thus the minimum Hall cross – sample distance in this case is around 20 μm. For the 4×4 μm^2 Hall cross the distance to the edge of the probe is 175 μm, so the minimum Hall cross – sample distance is around 12 μm. In fact, this distance is the limiting factor for the spatial resolution of the measuring device, but on the other hand the relatively large distance assures the safety of the Hall crosses (especially when the device has to work with topographically patterned magnets[1]).

There is another reason why it is not always desirable to go to a close distance. It was noticed that the magnetic field near the surface of the film is noticeably inhomogeneous along the surface (even for non-patterned films), with the period of inhomogeneity being smaller than the smallest Hall probe's active area. It is a known fact that at room temperature, where we must consider the Hall effect to be in the diffusive regime (the free path of the current carriers is smaller than the Hall cross size), the Hall response strongly depends on local field inhomogeneities [Liu '98, Guill.'03]. Even if we knew the Hall weighting function [Koon 93, Koon 98, Bend.'97] the interpretation of the measurements in inhomogeneous fields and their comparison with calculations would be a difficult task.

We measure the inclination angle α by taking a picture of the probe from its side with a digital camera and then measuring the angle using the software product ImageJ. This method gives an error of around $\pm 0.5^{\circ}$. The inclination angle can also be measured magnetically by comparison of two calibration graphs: one for the horizontal and the other one for the inclined position of the probe. The inclination angle is given by the formula:

$$\alpha_1 = \arccos\left(\frac{c_{s1}}{c_{s0}}\right),$$

where c_{s1} is the slope value of the calibrating line at $\alpha = \alpha_1$, and c_{s0} is the slope for the horizontal position of the probe. $[c_{s0}] = [c_{s1}] = \frac{\text{mT}}{\text{A}}$. This method demands a very high experimental accuracy (see annex IV), and thus the former technique was used.

---

[1] A corner of one of the probe's chips, which had been used many measurements in the contact mode, was notably rubbed off.

Test measurement of Hall-cross to sample distance

Let's consider an example of estimating the Hall cross-sample distance when the field generated by a Nd-Fe-B film thermomagnetically patterned in stripes is measured (for more details about the sample see section 3.3).

The 40×40 μm^2 Hall cross was used for these measurements. The distance l_1 from its center to the edge of the probe is 284 µm, the distance l_2 to the side edge is 500 µm. Fig. 2.12 shows the main interface window of the program of scanning process control and registration of topographic and magnetic data. The angle α is measured optically in the way described before. It was $5.3^o \pm 0.5^o$. A topographical image was used to estimate the angle β. In Fig. 2.12 (at the bottom) you can see topographical and magnetic images of the sample. The calibration line presented in Fig. 2.9 was used to convert the voltage into the altitude. Fig. 2.13 shows the sample's surface altitude profiles along the A, B and C lines indicated on the topographical image shown in Fig. 2.12. These profiles were used to estimate the corresponding average tilt of the sample with respect to the probe (angle β). It was estimated to be $0.4^o \pm 0.1^o$. Knowing the two angles and the two distances l_1 and l_2 we can calculate the Hall cross - sample distance:

$$d = 285 \cdot \sin(5.3^o \pm 0.5^o) + 500 \cdot \sin(0.4^o \pm 0.1^o) \cdot \cos(5.3^o \pm 0.5^o) = 29.7 \pm 3.3\ \mu m.$$

Fig. 2.14 shows calculated profiles of the z-component of magnetic field generated by this sample along the y axis for the Hall-cross to sample distances $d = 26.4$, 29.7 and 33.0 (the limits and the mean value of the distance's confidence interval 29.7 ± 3.3 µm). This graph presents variations of the field value estimation due to the uncertainty in the distance measurement. The peak to peak value of the field with the error interval is around $21^{+4.6}_{-3.7}$ mT (or 21 mT $^{+22\%}_{-18\%}$). The variation of the field values with the Hall-cross to sample distance depends on the sample, and in some cases it can be analytically predicted. An example will be given is section 3.2.

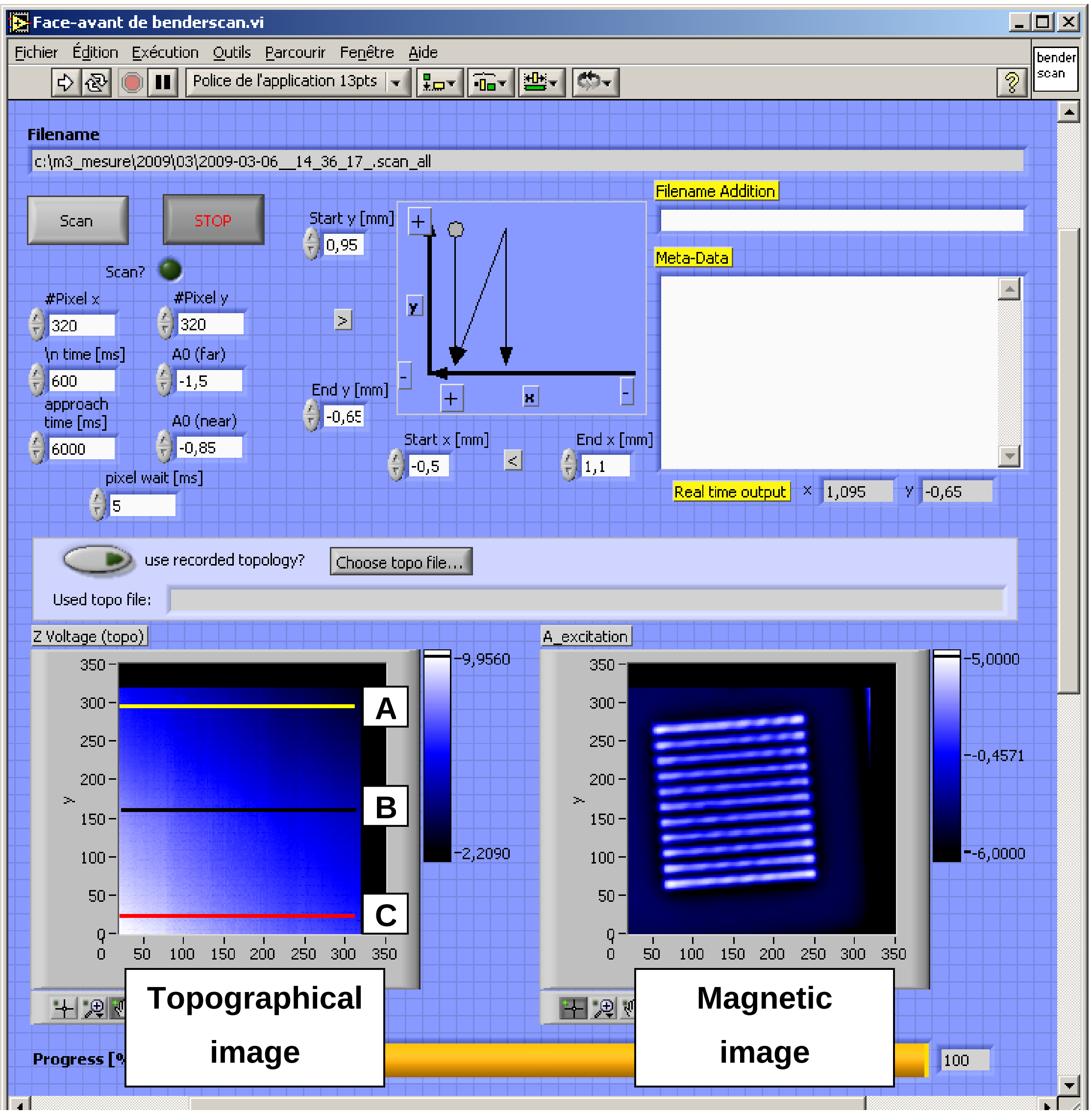

Filename: c:\m3_mesure\2009\03\2009-03-06__14_36_17_.scan_all

Start y [mm] 0,95

End y [mm] -0,65

Start x [mm] -0,5

End x [mm] 1,1

#Pixel x 320

#Pixel y 320

\n time [ms] 600

A0 (far) -1,5

approach time [ms] 6000

A0 (near) -0,85

pixel wait [ms] 5

Real time output x 1,095 y -0,65

Progress 100

Fig. 2.12. Main interface window of the program of scanning process control and registration of topographic and magnetic data.

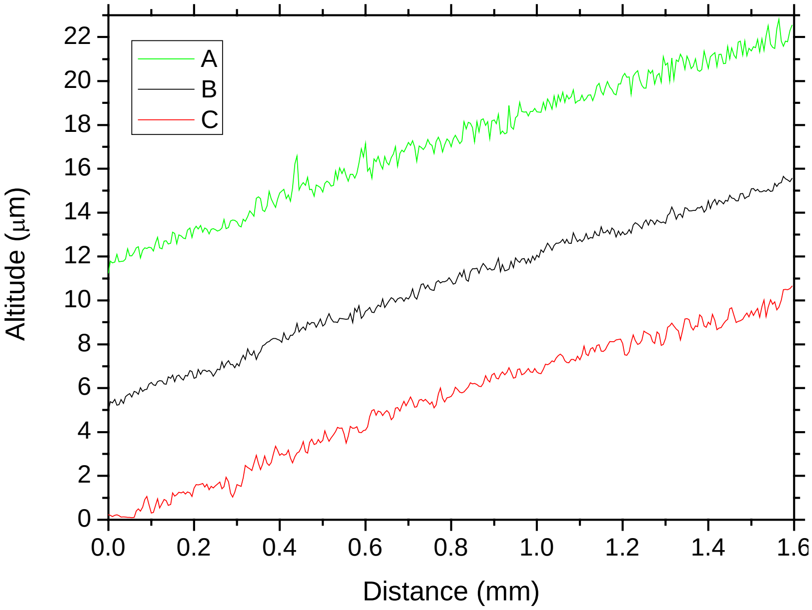

Fig. 2.13. Sample's surface altitude profiles along the A, B and C lines indicated on the topographical image in Fig. 2.12.

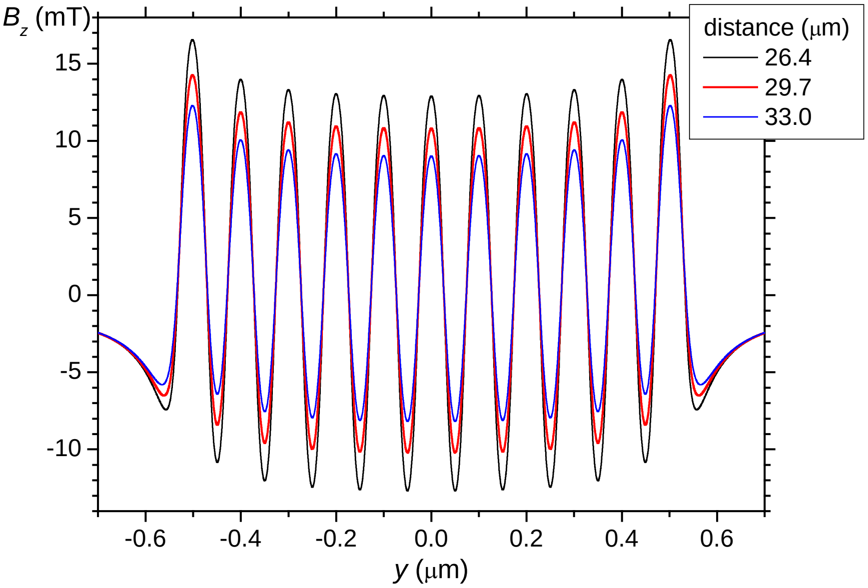

Fig. 2.14. Calculated profiles of the z-component of magnetic field generated by the stripe-like patterned sample along the y-axis for the distances from the surface d = 26.4, 29.7 and 33.0 μm (the limits and the mean value of the distance's confidence interval 29.7 ± 3.3 μm.)

2.3.5 Contribution of the in-plane components to the measured field profile

Due to the tilt of the probe, the Hall signal is proportional not only to the z-component of the field B_z but to the two components B_z and B_y (here we neglect the tilt β, for it is usually considerably smaller than α), and the Hall voltage is determined by the expression:

$$U = C \cdot \left(B_z \cos \alpha + B_y \sin \alpha \right),$$

where C is a coefficient of proportionality.

Continuing with the example of the stripe-like thermomagnetically patterned sample, let's see how far $B_z \cos \alpha + B_y \sin \alpha$ is from B_z. The inclination angle α in the case of our example is 5.3°. Fig. 2.15 shows calculated profiles of B_z and $B_z \cos \alpha + B_y \sin \alpha$ profiles along the y-axis at 29.7 µm from the sample. As it can be seen from the figure, the profiles almost repeat each other, there is only some distinguishable difference between them at the edges of the pattern, which anyway is much smaller than the uncertainty due to the distance confidence interval. Thus for these kinds of samples we can say that the SHPM measures the Z-component of the field, despite the probe's tilt. However, for some kinds of magnetic configurations, the difference between $B_z \cos \alpha + B_y \sin \alpha$ and B_z is more significant. An example of such a magnetic pattern will be given in annex V.

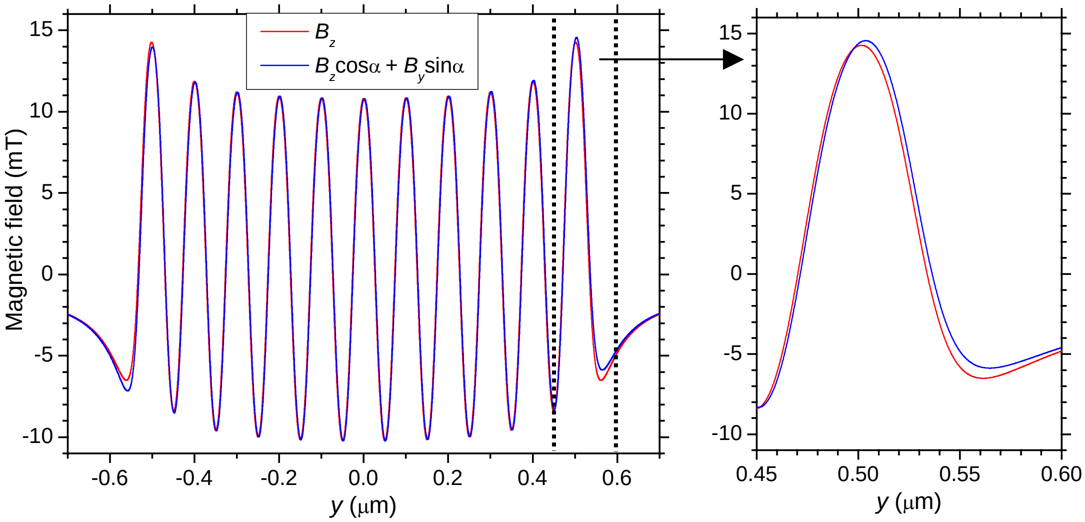

Fig. 2.15. Calculated profiles of B_z (red) and $B_z$cosα + $B_y$sinα (blue) profiles along y-axis at the distance 29.7 µm from the sample; α = 5.3°.

2.3.6 Measurement of all three components of magnetic field

Here we propose a simple way of measuring all three spatial components of a magnetic field using the single component SHPM described in section 2.3.1 with a few modifications to the set-up. A total of three scans along defined in-plane directions allows to extract the three spatial components of the magnetic field.

The core of the idea is very simple: if we want to measure all three components of the field generated by a sample at some point and we have a probe that can measure only one component, we have to take a measurement at this point three times for three different probe-sample relative orientations (these three orientations must not be coplanar). The seemingly easiest way to measure all components is to rotate the probe, or alternatively the sample, between measurements in such a way that 3 successive measurements are made with the probe's sensitive axis parallel to each of the axes of the coordinate system attached to the investigated sample. However, technically this would be very difficult to achieve. A more feasible way is to rotate the probe (or the sample) around one axis and take three measurements for three different values of the rotation angle (from 0 to 360^{o}). In our work we rotate the sample in the XOY plane keeping the probe fixed. To make the three probe-sample positions non-coplanar, the probe must be tilted with respect to the axis of rotation (value of the tilt must not be 0 or 90^{o}), and as we know from the previous section the probe is already tilted, so we don't add a new precondition. Note that to keep the probe's active area in the same point, it must lie on the axis of rotation. This condition will demand an additional pre-adjustment of the system.

Let these 3 different angles along with the probe tilt define the non-orthogonal *pqr* coordinate system (Fig. 2.16). To convert the measured field components (in the non-orthogonal *pqr* coordinate system) to the original frame of reference (the orthogonal *xyz* coordinate system), a coordinate system transformation is needed. Details of this transformation, as well as the choice of angles (α, β_1, β_2 and β_3) relating the two frames of reference, are given in annex V.

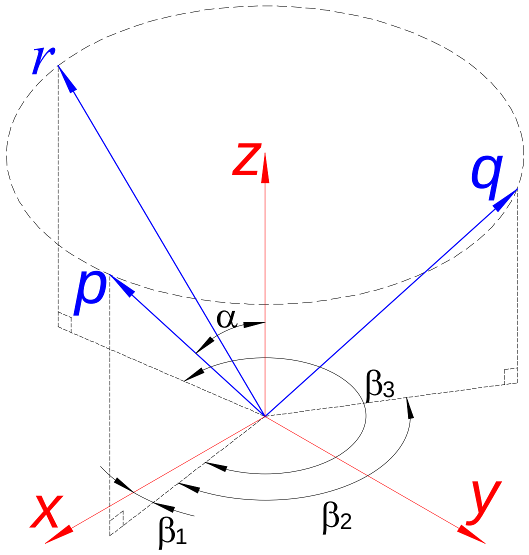

Fig. 2.16. Two coordinate systems: a nonorthogonal (*pqr*) determined by the sensor–to-sample position at the moments of measurement and an orthogonal (*xyz*) linked to the sample.

If we combine this approach with the scanning technique, we will have three magnetic images to reconstruct the images corresponding to the three field components. For this, software must be used to adjust the three initial images. If the probe's active area is on the axis of rotation the images can be just rotated using this software. If there is some unknown shift between the probe's active area and the axis of rotation, some topographical (for example the edge of the examined sample) or magnetic references must be used to compensate this shift during the image treatment (this question will be discussed later).

2.3.6.1 Modification of the set-up

The modifications of the set-up concern mostly the stepper motors. The "motor part" can be modified in two ways. The first way is to supply the system with a rotary table (preferably motorized) and with another XY-stage (not necessarily motorized) in addition to the existing motorized XYZ stage so that the rotary table is standing on the XY stage and serves as a base for the XYZ stage (Fig. 2.17). The rotary table is needed to provide rotation of the sample stage by a known angle. It will be shown later that the rotary table is not absolutely necessary, we just need a device which gives three predefined positions of the sample stage with a good precision. The XY stage at the bottom of the set-up is needed to adjust the probe's active area with respect to the axis of rotation (for example, using a magnetic reference; this question will be discussed later). Note that here the XYZ stage need not necessarily give absolute coordinates of its position. Relative coordinates (counted from the limiting position) suffice in this case. The second way is to place a rotary table onto an XYZ stage which gives absolute coordinates. This kind of motorized stage uses a feedback to "know" its exact position and costs considerably more than stages without a feedback (and hence giving only relative coordinates). Since the XYZ stage gives absolute coordinates we can take into account the possible shift between the probe's active area and the axis of rotation and there is no need for the second XY-stage. The second modification is to provide an ability to change the probe's tilt over a wider range (ideally from 0 to 90$^{\mathrm{o}}$).

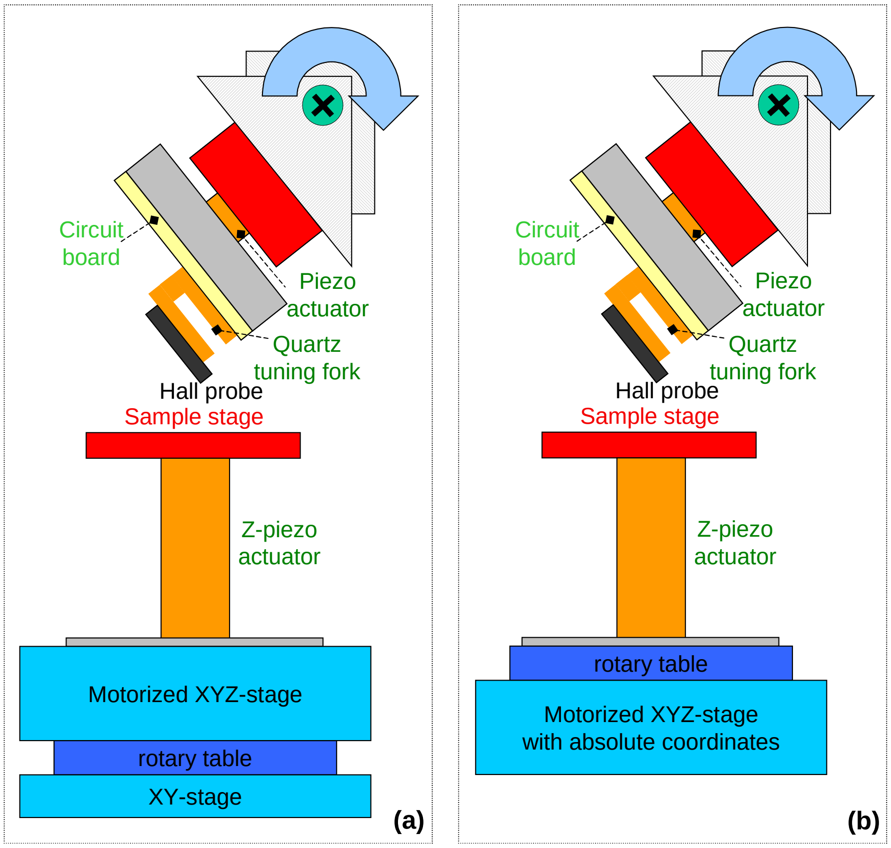

Fig. 2.17. Schematic diagram of two variants of the SHPM set-up.

Considering all possible realizations of the system, the rotary table may be replaced by a rotary "head" where the probe will be located. In this case the head with the probe is constantly turning and taking three measurements during each turn (the active area must be on the axis of rotation). In the scanning mode the sample stage may allow the probe make several turns about one point to be able to average the measured data, before moving to a new point of measurement.

2.3.6.2 Test measurement and its comparison with an analytical calculation

To validate our idea, test measurements were made with a bulk Nd-Fe-B magnet of parallelepiped shape (Fig. 2.18), the surface of which was 350 μm from the probe. The magnet is magnetized along the Z-axis.

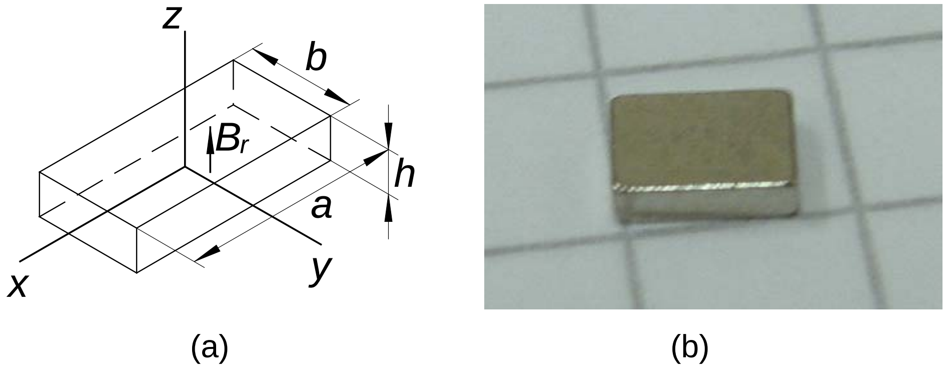

(a) (b)

Fig. 2.18. Schematic diagram (a) and photography (b) of the test sample: Nd-Fe-B parallelepiped magnet: $a = 4$ mm, $b = 3$ mm, $h = 1$ mm, $B_r = 1.4$ T.

The sample was measured using $\beta_1 = 0$, $\beta_2 = \pi$. The probe tilt α was 32 ± 1 degrees. The magnetic image of the sample for $\beta_1 = 0$ is shown in Fig. 2.19 (a). In fact this is the B_p component of magnetic field. Fig. 2.19 (c) shows the profile of B_p along the line in (a). The image of the B_q component (taken at $\beta_2 = \pi$) and its profile along the line are shown in Fig. 2.19 (b) and (d), respectively. Because of the symmetry of the sample the B_p and B_q components are symmetrical. The measured 2D distribution images and 1D profiles can be compared with the calculated graphs presented in Fig. 2.19 (e) - (h). In can be seen that the measured values are around 10% higher than the calculated values. The difference might come from the uncertainty in the measurement of the probe's inclination angle and probe – sample distance.

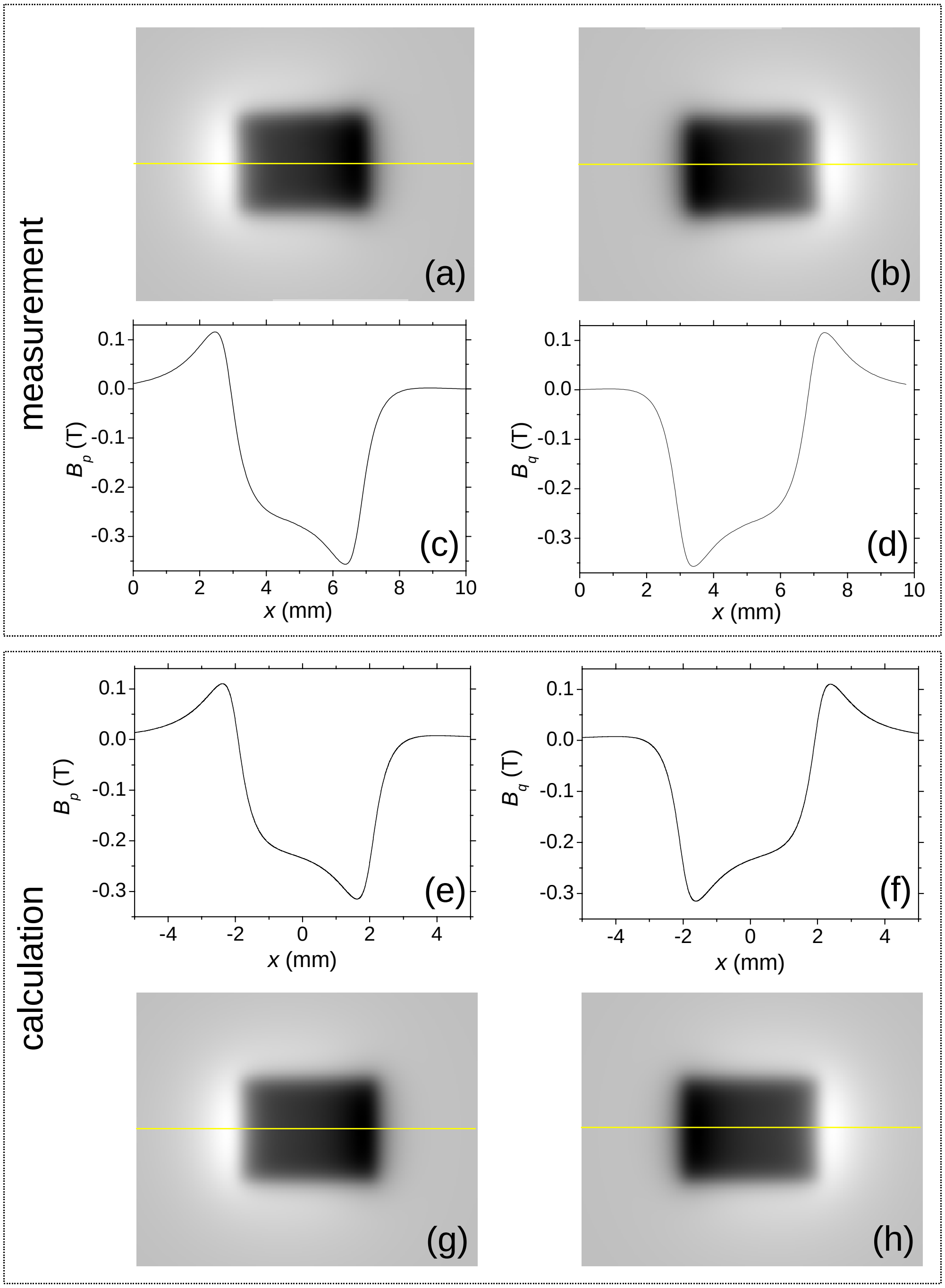

Fig. 2.19. Measured (top) and calculated (bottom) B_p and B_q components of the field generated by the test sample.

The B_x and B_z components formulas are given by (annex V):

$$B_x = \frac{B_p - B_q}{2\sin\alpha}\ , B_z = \frac{B_p + B_q}{2\cos\alpha}\ .$$

The mathematical operations with the initial images were done with the software product ImageJ. The resultant 2D B_x and B_z distributions and corresponding 1D profiles are presented in Fig. 2.20 (a) – (d). Calculated graphs are given in Fig. 2.20 (e) – (h) for comparison with the measurements. The measured and calculated profiles of the X-component are in a very good correspondence (better than 1%) while the measured values of the Z-component are higher than the calculated values by around 13%.

Since the initially measured values (of B_p and B_q) are 10% higher comparing with the calculated values, it is surprising that the measured and calculated values of B_x are in such good correspondence. It could be for the reason that during the test measurement the probe's active area was not adjusted to the axis of rotation of the sample. Hence the images of B_p and B_q are slightly shifted (though this shift is almost indistinguishable to the eye). This shift proved important for computing B_x. When the shift was not compensated, the profile of B_x had two negative and two positive peaks (Fig. 2.21 (b)) instead of one negative and one positive peak, as it should be for the in-plane component of the field generated by a magnet of parallelepiped shape. Note that the distance between the 'local' peaks in the 'global' peaks shows the value of the misalignment, so a profile of the IP-component generated by an OOP-magnetized parallelepiped PM may be used as an 'indicator' of misalignment.

Image Fig. 2.20 (a) (as well as (b)) was reconstructed taking the misalignment into account. There was an error due to the uncertainty in the misalignment computation, which was not estimated. It is clear that we need to use a specially prepared and optimized magnetic reference sample to correct the misalignment rather than using the examined sample itself as a reference. Note that the operation of misalignment compensation must be done only once. We could not do it because at the time of the test measurement we did not yet have a rotary table and the sample rotation was performed by hand. The test measurement was rather done to prove the idea, not for accurate testing of the measuring device. Work on the proper modification of the set-up for 3D measurements is in progress.

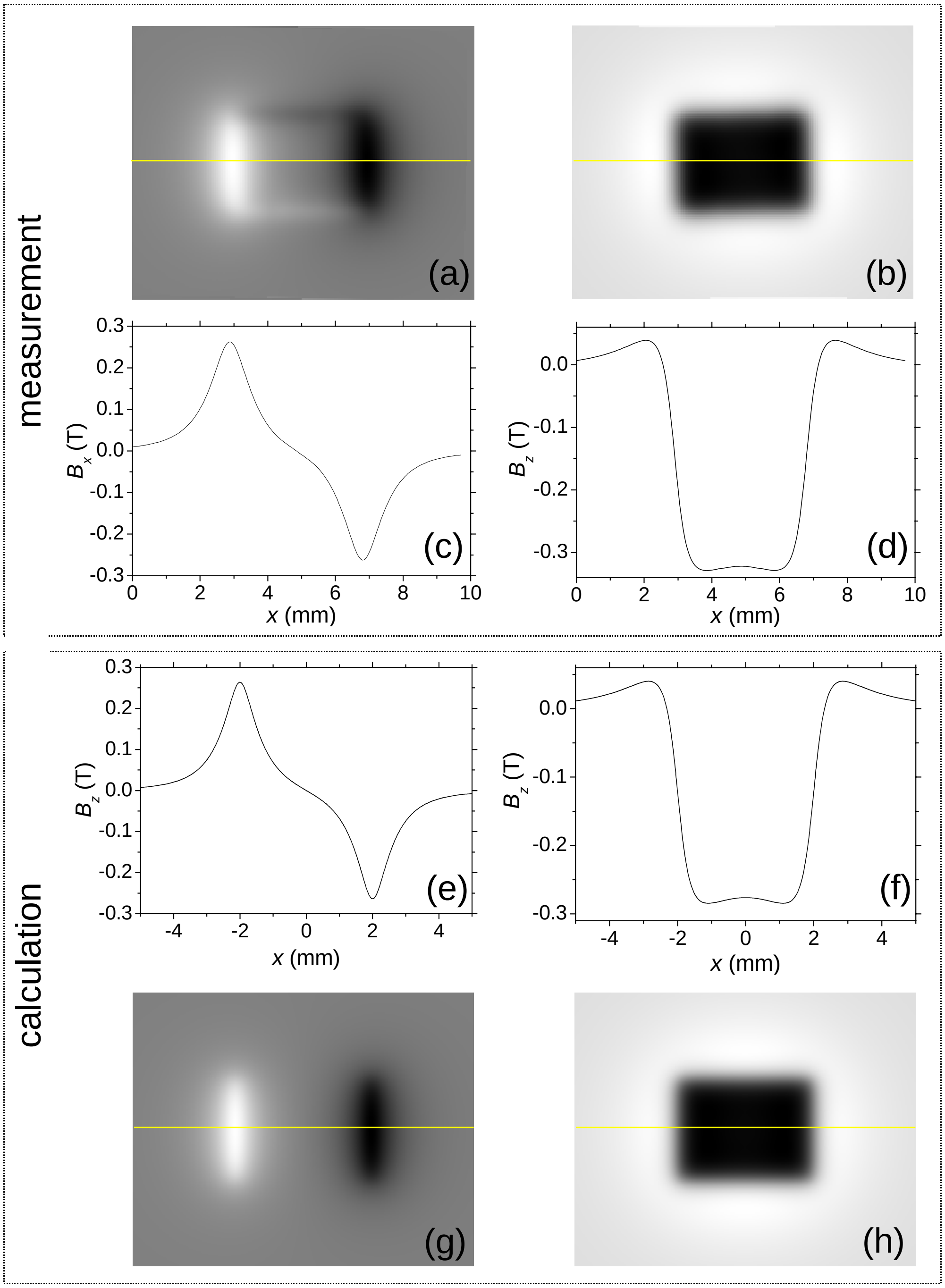

Fig. 2.20. Measured (top) and calculated (bottom) B_x and B_z components of the field generated by the test sample.

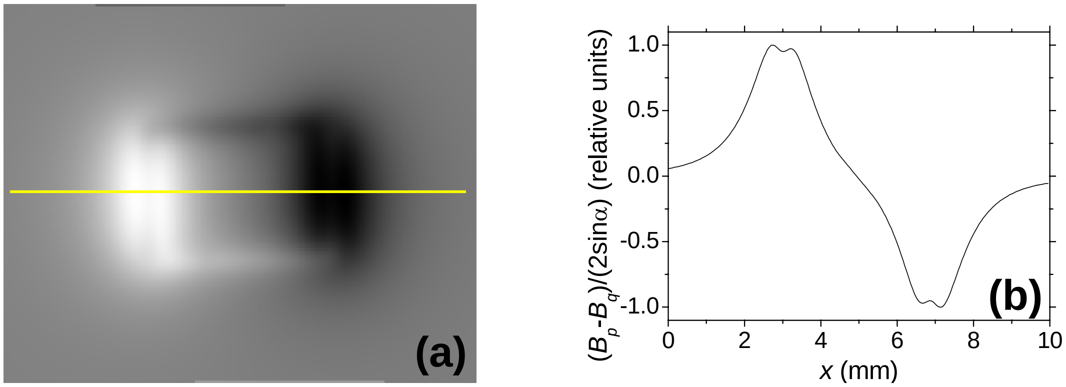

Fig. 2.21. (a): 2D image of $\frac{B_p - B_q}{2\sin\alpha}$ when the magnetic images of B_p and B_q are slightly shifted one with respect to the other; (b): profile along the yellow line.

2.3.6.3 Conclusions for the 3D measurements

We presented a simple way of measuring all three spatial components of a magnetic field using a single component SHPM or any kind of scanning probe microscopes using a one-coordinate probe (e.g. magnetoresistor, flux-gate) with minor modifications.

Note that despite the fact that the method requires three scans over a sample it does not necessarily mean that it needs thrice as much time as a scanning probe microscope supplied with a 3D-sensor. The total time will depend on the time constants, which depend on the signal noise. Another point is if the 3D-sensor is an assembly of three individual sensors, which are located at some distance from each other, it means that we will have to increase the scanning lateral range to take into account the gap between the probes.

However, time of measurement is a disadvantage of the method. Another disadvantage is the need to position the Hall cross at the center of rotation of the sample stage.

The advantages of this technique include:

- relative simplicity and low cost of the set-up,
- low noise and relatively small sensing area (e.g. typically ~5x5 μm^2 for GaAs 2D-EG Hall probes),

- the measurement of each component is taken at the same distance from the sample surface,
- since there is only one probe there is only one sensitivity coefficient (and hence only one offset and only one sensitivity with temperature drift), and not three as in the case of using a 3D sensor, which considerably simplifies the calibration procedure.

2.4 Magneto-optic Faraday microscopy

The work described in section 2.4 was done in collaboration with Prof. Rostislav Grechishkin (Lab. of Magnetoelectronics, Tver State University, Russia).

2.4.1 Magneto-optic imaging films (MOIF)

In this work we use bismuth containing ferrite garnet magneto-optic imaging films (MOIF) (supplied by Mikhail Gusev, Zelenograd, Russia). They are transparent monocrystalline layers, prepared by liquid-phase epitaxy. The typical composition for magneto-optic applications is $R_{3-x}\,Bi_x\,Fe_{5-y}\,M_yO_{12}$, where R is a combination of rare earth elements, M - Ga, Al and microadditives of elements with an empty *d*-shell. The active layer of ferrite garnet (usually 2-10 µm in thickness) is grown on a rigid transparent substrate made of gadolinium-gallium garnet ($Gd_3Ga_5O_{12}$) of thickness 300-500 µm (Fig. 2.22 (left)). A thin layer of silver or aluminium is deposited onto the active layer, to act as a mirror and so to double the angle of rotation of the plane of polarization due to a doubling of the path length (Fig. 2.22 (right)).

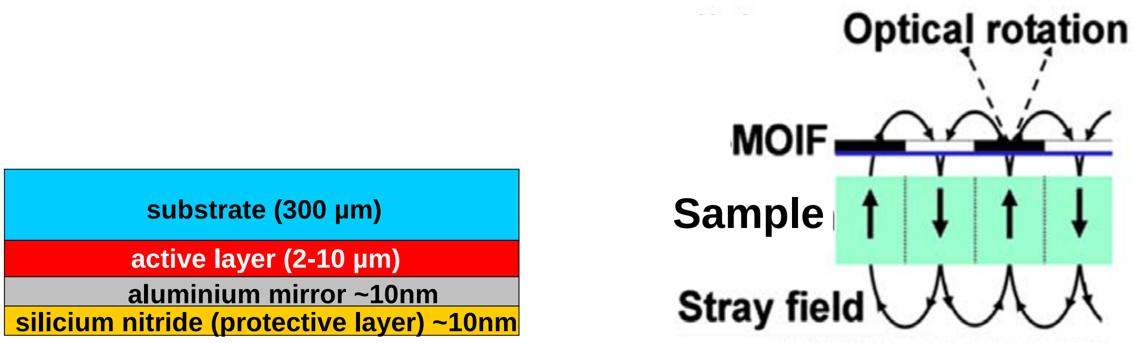

Fig. 2.22 (left): schematic diagram of the MOIF structure (not to scale); (right): scheme of magneto-optic imaging with a MOIF.

Transparency in the optical range and high values of the Verdet constant make these films useful for visualization of magnetic field distributions exploiting the Faraday effect, the principle of which was already given in section 1.1.4.

For most magneto-optic set-ups, the light falls perpendicularly to the surface of a MOIF. In this case the dot product **M·k** from formula for the Faraday rotation (see section 1.1.4):

$$\vartheta(\omega) = \vartheta_F(\omega) l = \nu(\omega) \cdot l(\mathbf{M} \cdot \mathbf{k}), \tag{2.4.1}$$

is maximal. For such an orientation a MOIF is sensitive only to the OOP component of the stray magnetic field. Later on we will deal only with this orientation.

One of the most important characteristics of MOIF is their magnetic anisotropy. Directions of the easy magnetization of the films are determined by the minimum of the anisotropic part of the free energy, including energies of cubic anisotropy E_c, uniaxial anisotropy E_u, interaction with the external magnetic field $E_m = -\mu_0(\mathbf{M} \cdot \mathbf{H})$ and energy in self demagnetizing field $E_d = -\mu_0(\mathbf{M} \cdot \mathbf{H}_d)/2$.

For ferrite garnet films the constant of uniaxial anisotropy K_u is generally represented by magnetoelastic component K_u^s, arising due to differences in the lattice parameters of the film and substrate, and growth component K_u^g , evolving during film crystallization because of nonstatistical ion distribution in garnet magnetic sublattices [Grech.’07].

The technology of the method of liquid phase epitaxy allows obtaining ferrite garnet films with different types of effective magnetic anisotropy (by controlling its magnetoelastic component). Depending on ratios between the corresponding constants of the anisotropy, it is possible to get one of the three anisotropy types: easy axis, easy cone or easy plane.

Mostly the MOIF with the anisotropy of only the former and the latter type (easy axis and easy plane) are used for MO imaging. In the first case (easy axis anisotropy) the MOID are called “uniaxial”, in the second case (easy plane anisotropy) they are called “planar”. The both types are used for imaging of distributions of the stray magnetic field component perpendicular to the plane of the films. The main difference between the uniaxial and planar MOIF is that the uniaxial ones give us only quantitative information (yet we will show below how they can be used for obtaining qualitative information), while the planar ones can give us qualitative information about the stray magnetic field’s out-of-plane (OOP) component.

2.4.2 Quantitative imaging with the aid of planar MOIF

The work described in this section was done in collaboration with Sergey Soshin, Sergey Chigirinsky, and Rostislav Grechishkin (Lab. of Magnetoelectronics, Tver State University, Russia).

The Faraday rotation for planar MOIFs is a continuous function of the z-component of the stay field in every point (x, y). This feature allows using them as analog sensors of magnetic field distributions [Grech'96].

The intensity of the light passed through a MOIF is determined by Malus' law. For a "non-ideal" optical system with an extinction coefficient ξ, Malus' law can be written as:

$$I_{\pm} = (1-\xi)I_0 \exp(-\alpha l)\left(\sin^2(\beta \pm \vartheta_F l) + \xi\right), \tag{2.4.3}$$

where β is the angle of polarizer/analyzer uncrossing, I_0 is the incident light intensity, α is the attenuation factor [Shurk.'62].

The light intensity distribution can be registered by a CCD matrix of a digital camera, which the polarizing microscope is supplied with. The camera is connected to a computer for recording and treatment of the data.

The quality of imaging can be considerably improved by using the so-called differential regime of registration and processing the images. The idea of the method is the following. If we change the sign of angle β we inverse the Faraday contrast, leaving the optically passive image components (such as scratches on the MOIF's mirror, dirt on the film's surface and so on) unaffected.

For $|\beta_1| = |-\beta_2| = \beta$ the corresponding light intensities are:

$$I_1 \sim \sin^2(\beta + \vartheta_F l) \text{ and } I_2 \sim \sin^2(-\beta + \vartheta_F l). \tag{2.4.4}$$

Pixel-by-pixel subtraction of the images obtained for $\pm\beta$ provides compensation of the optically passive background, while the useful signal is expressed by the formula [Grech.'07]:

$$\Sigma I(x,y) = I_1(x,y) - I_2(x,y) \sim \sin(2\beta)\sin(2\vartheta_F l). \tag{2.4.5}$$

For angles $\vartheta_F < 5^{\circ}$, $\sin(2\vartheta_F l)$ can be approximated by the value of its argument, $2\vartheta_F l$. And since the Faraday rotation ϑ_F depends linearly on the z-component of magnetic field (see (2.4.1)), the light intensity registered by the camera almost linearly depends on the field's z-component. The factor sin(2β) determines the slope of the transfer characteristic. The angle of polarizer/analyzer uncrossing β has to be chosen taking into account the measured fields and the sensitivity range of the camera.

If U is the light intensity value given by the camera in a point (x, y) (the value U is proportional to the intensity of the light impinging on the pixel of the camera's CCD matrix, located at the point (x, y)) we can write

$$U(x, y) = kB_z(x, y), \tag{2.4.6}$$

where k is the proportionality coefficient. This coefficient depends on the Verdet constant of the material for the given incident light frequency, thickness of the film, the angle of polarizer/analyzer uncrossing, the intensity of the incident light in the point (x, y) and the sensitivity coefficient of the camera. Due to the non-uniformity of the incident light, local variations of MOIF properties, and pixel-by-pixel variation of the sensitivity coefficient of the camera, the proportionality coefficient k is also a function of x and y. The distribution of the coefficient $k(x, y)$ over the field of view must be found by a calibration procedure.

Example of quantitative imaging

Here we will show an example of quantitative imaging of the distribution of the OOP component of the magnetic field generated by a 10 μm thick Nd-Fe-B film topographically-patterned in stripes with a period of 40 μm. The imaging was done using an inversed horizontal polarizing microscope MIM-8 supplied with an 8 bit black-and-white digital camera (Watec WAT-902B) for registering images connected to a PC by a usual video capture device (Pinnacle 500-USB) for registering images. The planar MOIF used for the measurements was attached to the microscope's sample stage and then calibrated in the field of a solenoid. The sample was approached to the MOIF with the aid of a Z-positioner (Fig. 2.23). Special attention was paid in order to avoid any movement of the MOIF during the calibration and the measurements. Using the calibration distribution of the proportionality coefficient $k(x, y)$, the B_z distribution (Fig. 2.24 (a)) was reconstructed from the halftone image (Fig. 2.24 (b)) taken in the differential regime (described above) [Chig.'09].

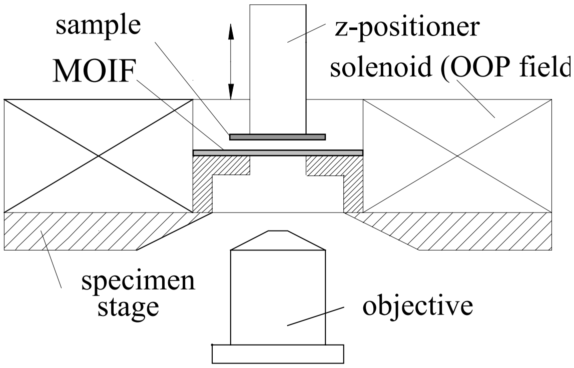

Fig. 2.23. Schematic diagram of the set-up used for quantitative imaging with a planar MOIF (side view).

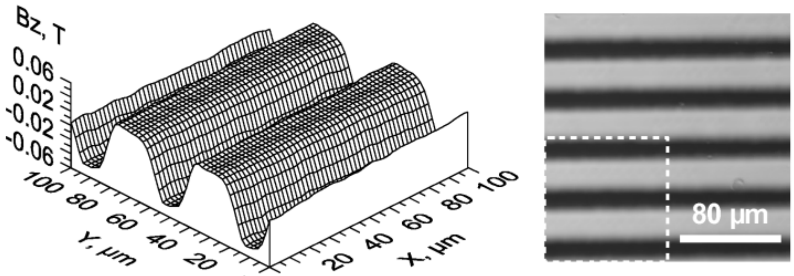

(a) (b)

Fig. 2.24. B_z distribution (a) reconstructed from the halftone image (b) obtained with the aid of a planar MOIF at a distance of 4 µm from the surface of a unidirectionally magnetized Nd-Fe-B film topographically patterned with a period of 40 µm.

2.4.3 Qualitative and quantitative imaging with the aid of a uniaxial MOIF

Usually uniaxial MOIF are used for qualitative imaging of the OOP-component of stray magnetic field. Here we present the method that allows using a uniaxial MOIF for obtaining qualitative information about the stray magnetic field's OOP-component. Here we used a polarizing microscope Leica supplied with a digital camera (Watec WAT-902B). The sample stage of the microscope was fitted with a calibrated solenoid for generating a vertical bias magnetic field, homogeneous in the region of the sample location (Fig. 2.25). The solenoid was fed with a regulated DC current using a power supply / operational amplifier (Kepco BDP 100-4M). A digital amperemeter was used for measuring the current in the solenoid.

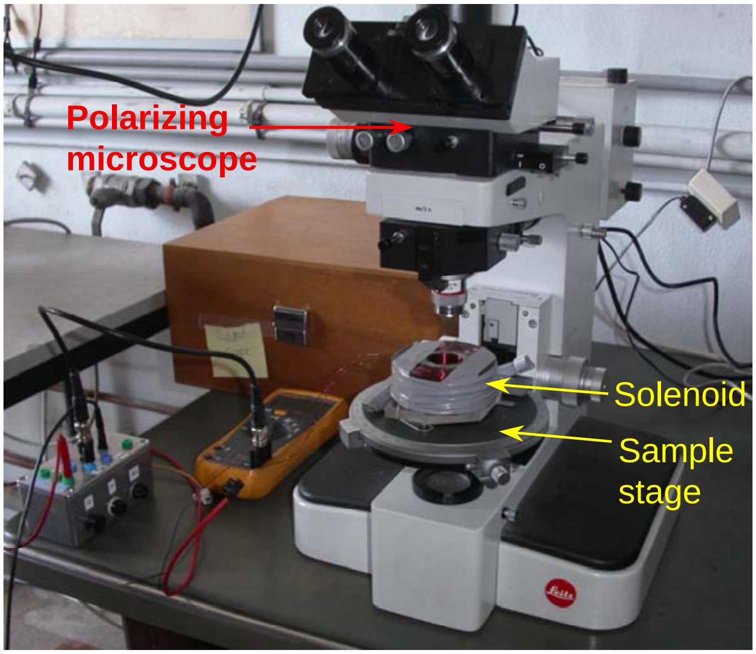

Fig. 2.25. Experimental set-up: polarizing optical microscope with a solenoid around the sample position.

Fig. 2.26 (a) shows the intrinsic domain structure of a uniaxial MOIF (i.e. in zero external magnetic field). 180-degree band domains with the magnetization vector of all domains perpendicular to the film plane are observed. The width of the domains with magnetization pointing up is equal to the width of the domains with magnetization pointing down so that the overall magnetization of the film is equal to zero. Fig.

2.26 ((b) shows the domain structure of the MOIF when it is positioned in the stray field produced by a micro-structured hard magnetic film. Since the MOIF is uniaxial, the binary grade of brightness (i.e. dark or bright) simply informs us of the direction of the vertical component of the stray field (up or down). The position of the domain walls indicates the regions where the z-component of the stray magnetic field is zero, i.e. the domain walls delineate the zero-field isolines of the magnetic field pattern produced by the micro-structured magnetic film at the position of the MOIF. Used in such a manner, a uniaxial MOIF works as a null-sensor and gives qualitative information concerning the direction of the stray field's z-component at a fixed distance above the film.

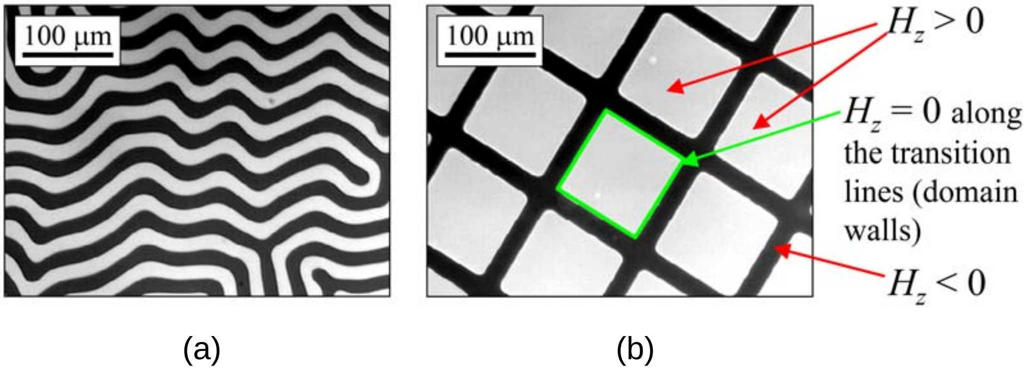

Fig. 2.26. (a) Intrinsic domain structure of a uniaxial MOIF in zero external field; and (b) the induced domain structure of the same MOIF positioned in the stray field of a micro-structured hard magnetic film.

The superposition of a homogeneous external magnetic field (bias field) onto the field pattern produced by the micro-structured hard magnetic film leads to a shift in the position of the zero field isolines (Fig. 2.27). Knowing the magnitude of the bias field, we can access quantitative information concerning the z-component of the stray field of the micro-structured hard magnetic film.

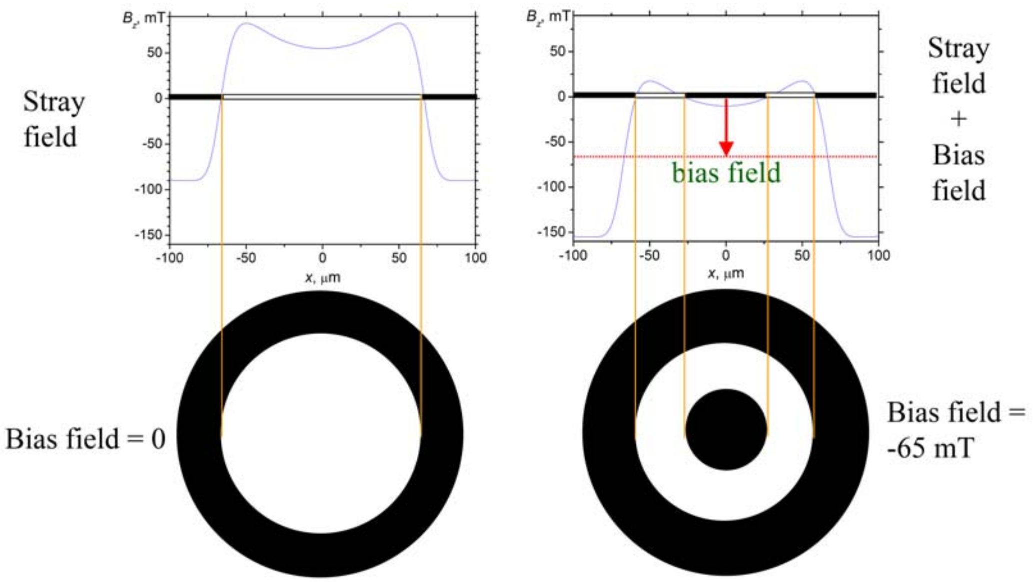

Fig. 2.27. Stray magnetic field profile (z-component) at a given distance from a suppositional field source without (top left) and with a bias field (top right) and schematic representation of the domain structures that such field patterns would induce in a uniaxial MOIF (bottom).

Test sample results

A series of binary images of the uniaxial MOIF were captured in the presence of a bias field of varying magnitude. Fig. 2.28 (a) shows serial sections of the z-component of the magnetic field generated by a grid-like thermo-magnetically patterned film, used here as a test sample (film thickness = 5 μm, remanent magnetization = 1.4 T, grid used for TMP: hole size = 100×100 μm^2, grid wall width = 20 μm) at the given values of bias field. Note that hysteresis occurred between increasing and decreasing bias fields when nucleation of a reverse domain occurs in the MOIF because the energy required to nucleate a reverse domain is greater than the energy needed to move the domain wall. For this reason the experimental images were taken under such conditions of changing bias field that the size of isolated domains in the MOIF was always decreasing. For example, if we observe that a new domain appears in the MOIF while the bias field is increasing, we decrease the field down to the value where the new domain disappears again. Pinning of the domain wall in the MOIF is neglected. To reconstruct the whole magnetic picture we use only the values of the bias field for which the domain size decreases. These experimental results are in relatively good agreement with calculated serial sections shown in Fig. 2.28 (b). Calculated 3D plots showing the serial sections as cuts from the top are presented in Fig. 2.28 (c).

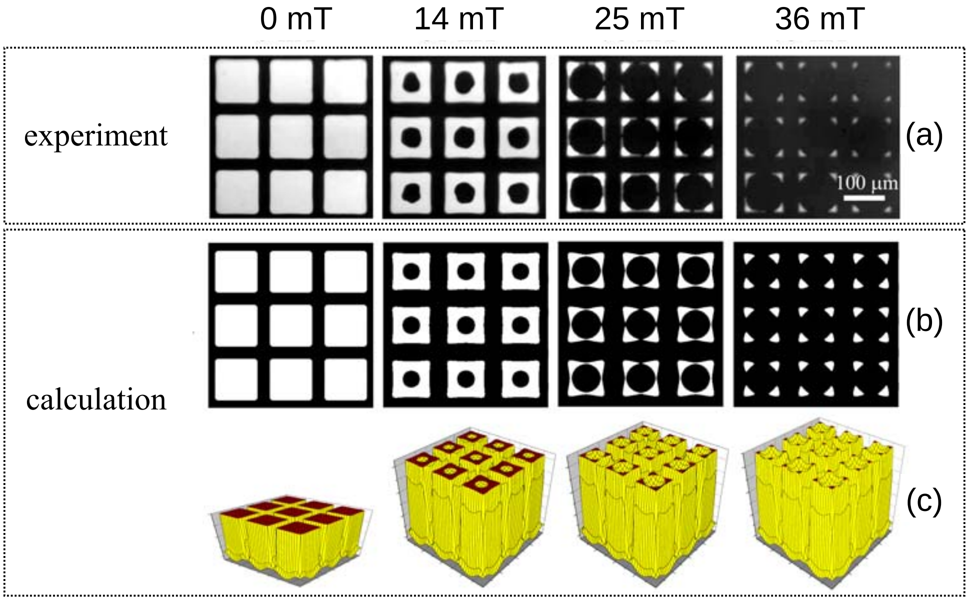

Fig. 2.28. Serial sections of the B_z magnetic field distribution at a distance of 5 µm above a thermomagnetically patterned NdFeB film under different biasing fields: (a) images of a uniaxial MOIF under different bias fields, (b) calculation of the resultant field pattern when a bias field is superimposed on the calculated field pattern, and (c) calculated pseudo 3D plots showing the serial sections as cuts from the top.

Note that since we consider just the binary grade of brightness (dark or bright), we can ignore variations in light intensity due to inhomogeneous illumination in the microscope (e.g. the increase in the level of brightness towards the bottom of the images in Fig. 2.26). For this reason, the requirements concerning the quality of the microscope and care needed when imaging are much less stringent for a uniaxial MOIF compared to a planar MOIF, where changes in light intensity are used to extract the values of z-component of the local magnetic field.

Comparison between images obtained with the aid of a uniaxial and a planar MOIF

The same sample was investigated with the aid of a planar MOIF (Fig. 2.29 (a)). The initial half-tone image was programmatically transformed into the binary form (Fig.

2.29 (b)) for comparison with the corresponding image taken using a uniaxial MOIF (Fig. 2.28 (a), 14 mT). From the comparison it can be seen that the "uniaxial MOIF image" contains less details than the "planar MOIF image". In the image in Fig. 2.29 material nonuniformity was revealed while this information is lost in the corresponding image taken with the uniaxial MOIF. It shows that the resolution of the imaging technique is lower in the case of the uniaxial MOIF due to the high energy of domain nucleation. Note that in the case of planar MOIF we see the sample's stray field distribution directly while in the case of the uniaxial MOIF we see the domain structure of the MOIF which "tries" to shape itself according to the stray field coming from the sample.

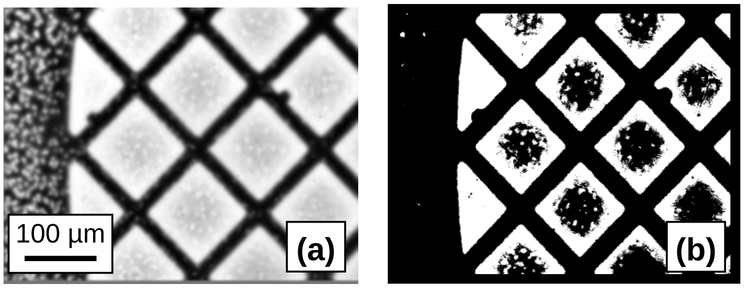

Fig. 2.29. (a): A half-tone magneto-optic image of the sample as observed with a planar MOIF; (b): image in (a) after binarization.

Despite the disadvantages of the method (relatively low spatial resolution and accuracy due to the hysteresis caused by pinning of domain walls and high domain nucleation energy), magneto-optic imaging using a uniaxial MOIF and a bias field has potential applications for magnetometry for quick quantitative imaging of stray magnetic field generated by permanent micro-magnets in cases when the precision of measurements is not critical. The obvious advantages of the technique include relatively low cost of the uniaxial MOIF (in comparison with the planar ones), low requirements for the quality of polarizing microscope (polarization, light homogeneity, etc), and short time for obtaining images.

2.5 Comparison of SHPM and MO-imaging

Spatial resolution

The spatial resolution of a SHPM is determined by the size of the Hall-cross used, the Hall-cross to sample distance and the scan step size used. Hall-crosses of size 4×4 and 40×40 μm^2 were used in this work while the Hall-cross to sample distance was in the range 20-30 µm and measurements were made with a step size of 5 µm. We estimate that the spatial resolution of the SHPM used here is of the order of 10 µm. The spatial resolution of MOIF is limited by the wavelength of light, the thickness of the sensitive layer used, the distance from the sensitive layer to the sample (which may depend on the roughness and the cleanness of the surface), and the typical size of domains (only for the uniaxial MOIF). We estimate that the spatial resolution for the MOIF imaging used here is of the order of several micrometers for the planar films and of the order of 10-20 µm for the uniaxial ones.

Note that we aim to improve the spatial resolution of SHPM, by using finer Hall-crosses and by decreasing the Hall-cross to sample distance (this will be achieved by reducing the in-plane distance between the Hall-cross and the edge of the overall probe.

Measurement time

The scanning technique is by definition slower than the imaging technique. Scanning time depends on the size of the surface being measured and the step size used. Typical scan times of 2 hours (typical scan surface area 2×2 μm^2, step size = 5 µm) were used in this work.

Though all the data is collected at once with the MO imaging technique, quantitative analysis requires post image processing. For the case of quantitative imaging with a uniaxial MOIF, using the novel method presented in section 2.4.3, no calibration of the MOIF is needed (as opposed to quantitative imaging with a planar MOIF), but the data acquisition requires more time since sequential imaging in different bias fields is required.

2.6 Conclusions

In this chapter we have described two experimental techniques to locally measure the stray fields produced by micro-patterned hard magnetic films. In the first case a recently constructed, home-made scanning Hall probe microscope was used. In this work, protocols for the measurement of a sample's surface topography and tilt, as well as the Hall-cross to sample distance, were established. These measurements are essential for the quantitative characterisation of stray field profiles. The validity of the field profiles obtained, on test samples, was established by comparison with analytical calculations. A novel method for the measurement of the 3 spatial components of the stray field, using a single component probe, was proposed. The method involves making three consecutive measurements, with a rotation of the sample relative to the probe, between each scan. The method was validated by test measurements on a mm-sized magnet.

The second technique studied concerns magneto-optic microcopy with the aid of planar and unixial magneto-optic indicator films (MOIF). MOIF are extremely useful for the quick, qualitative characterization of micro-patterned hard magnetic films, revealing the sign and spatial extent of the z-component of the stray field. An example of quantitative imaging with a planar MOIF is demonstrated. A novel method was established for quantitative imaging with the aid of a uniaxial MOIF. The method involves sequential imaging in a bias field of variable intensity. Experimental data on a test sample was compared to analytical calculations. The use of a bias field can also serve to extend the range of the field measurable with a planar MOIF.

The aim of this chapter was to describe and compare two different techniques for quantitative characterization of the stray fields produced by micro-patterned hard magnet films. In all cases, test measurements were validated by comparison with analytical calculations. In the following chapter, z-component field profiles, obtained with the SHPM, will be presented for two types of patterned films.

Chapter 3: Characterization of micromagnets: results and discussion

3. Characterization of micromagnets: results and discussion

3.1 Introduction

In the last chapter we described two different techniques for quantitative characterization of the *z*-component of the stray fields produced by micro-patterned hard magnet films. In this chapter we will present measurements made with one of these techniques, scanning Hall probe microscopy, on Nd-Fe-B hard magnetic films. This technique was chosen because it is more precise and we are more confident in our estimation of the probe to sample distance with this technique than with the MO-imaging technique. The hard magnetic films were patterned at the micron scale using both topographic and thermomagnetic methods. Details of the preparation techniques are given in annex 1. The experimental field profiles will be compared to analytical calculations, to access, in a non-invasive manner, information concerning the micro-magnets' internal magnetic structure. The measured field profiles will be used to derive the spatial variation of the field and field gradient values at different distances from the sample surface [Kust.'10].

3.2 Characterization of topographically patterned films

A 38 µm thick magnet deposited on a stripe-like topographically patterned substrate was investigated. An optical plan-view image of the topographically patterned substrate is shown in Fig. 3.1. The patterned substrate has etched features of a constant depth 40 µm, nearly constant length around 2 mm and variable widths in the range 10-50 µm. The Hall probe was scanned above the sample at an estimated height of 25 ± 3 µm (Hall probe active area size = 4×4 µm^2, measurement step size along y is 5 µm).

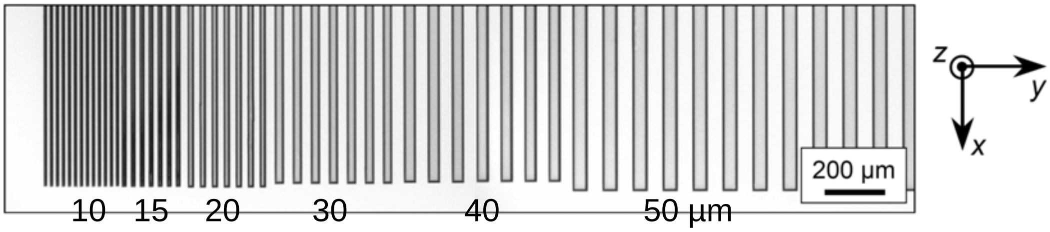

Fig. 3.1. Optical plan-view image of a part of the topographically patterned substrate. The stripe width of the corresponding section is indicated (in µm).

The 2D image and two 1D profiles of the out-of-plane magnetic field component, measured by the SHPM are shown in Fig. 3.2. The profile in Fig. 3.2 (a) corresponds to a scan made towards the center of the motif while the profile in Fig. 3.2 (c) corresponds to a position close to the bottom edge of the motif. The 1D profiles show that the amplitude of the magnetic field produced at a given height above the sample decreases as the feature width decreases. Features as small as 15 µm are resolved at a scan height of 25 µm. The measured profiles have a vertical offset, the magnitude of which is greater for the measurement made near the bottom edge of the motif.

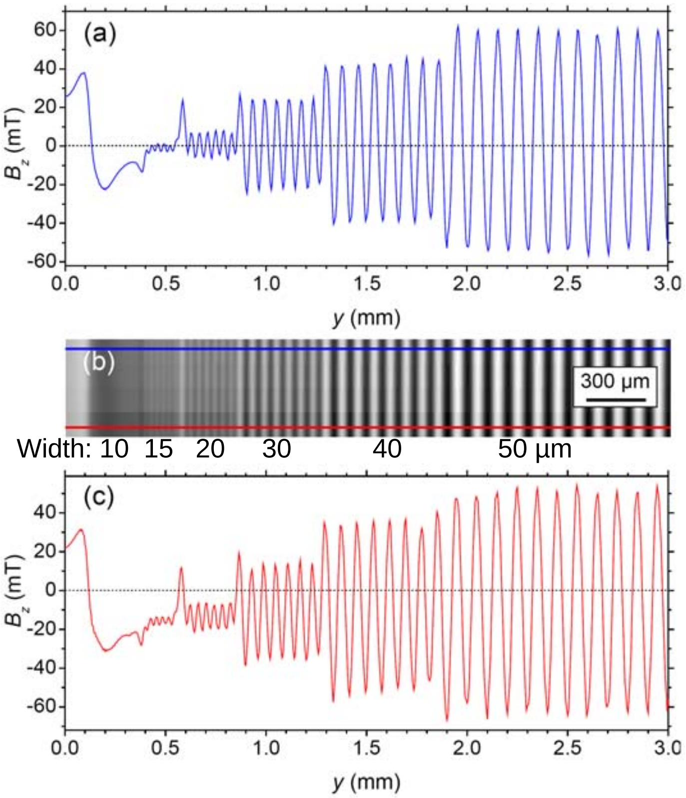

Fig. 3.2. 2D image (b) and 1D profiles of the out-of-plane magnetic field component measured at a height of 25µm above a topographically patterned 38 µm thick NdFeB film unidirectionally magnetized out-of-plane measured towards the center of the motif (a) and near the edge of the motif (c).

The B_z/B_r profile at a height of 25 µm above the center of such a topographically patterned film, where B_r is the remanent induction of the magnetic material, was calculated analytically. The geometry of the modeled structure was based on a scanning electron microscope (SEM) image of the film's cross section, shown in Fig. 3.3 (a). Assuming a parallelepiped shape for the magnets and neglecting the deposit on the sidewalls of the trenches, calculations were made either considering or neglecting the magnetic material deposited at the bottom of the trenches (Fig. 3.3 (b)). Note that the thickness of the sidewall deposit is only about 5 µm and its overall volume content becomes less significant as the feature width increases. The calculated profiles in Fig. 3.4 reveal that the bottom magnets contribute only to a slight shift in the vertical off-set of the B_z/B_r profile but to no appreciable difference in the peak-to-peak induction. The overall shape of the calculated profiles is in very good agreement with the measured profile (Fig. 3.2 (a)), thus validating the assumptions made in modeling the structures. Calculations (not shown here) demonstrate that the vertical offset in the field values has two contributions: (i) the non-patterned film sections in proximity to the patterned motif and (ii) the finite length of the motif's features. This explains why the vertical offset is stronger in the profile measured at the edge of the motif than that measured towards the center of the motif.

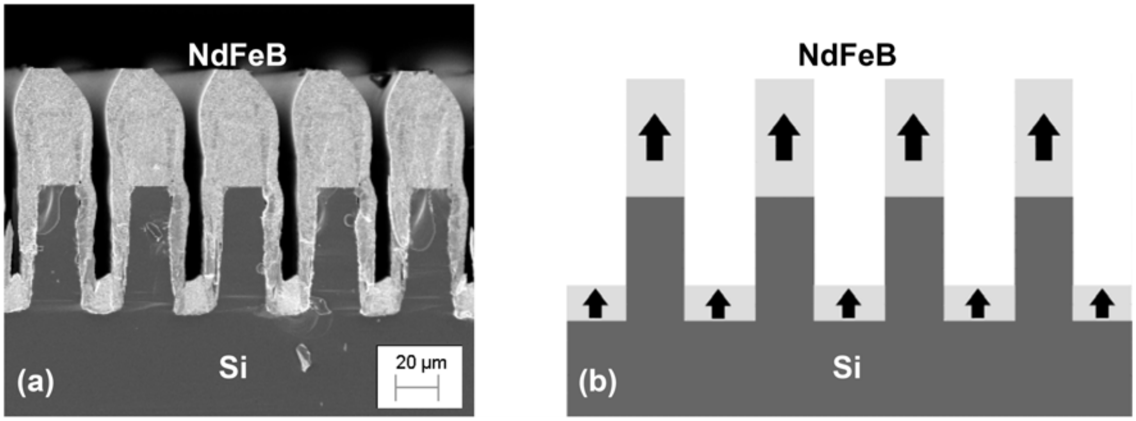

Fig. 3.3. (a): SEM image of the fractured cross-section of a 38 µm thick NdFeB film deposited on a Si wafer patterned by deep reactive-ion etching (DRIE) (the film section shown here has 20 µm wide features); (b): schematic representation of the structure assumed for analytical calculation of the stray field patterns produced by the topographically patterned film (note that the deposit on the sidewalls is neglected).

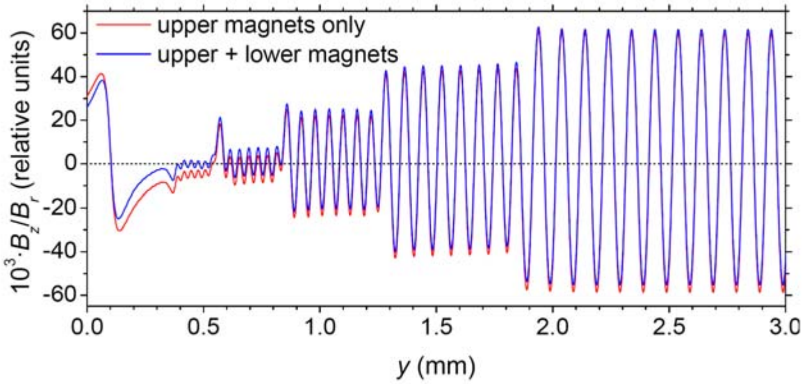

Fig. 3.4. Calculated 1D profiles of the out-of-plane magnetic field component along the center of the motif, normalized to the value of remanent induction of the magnetic material, assuming a scan height of 25 µm.

The calculations and measurements show that both peak-to-peak magnetic field values, $B_z^{\text{p-p}}$, and the ratio $B_z^{\text{p-p}}$ (50 µm)/$B_z^{\text{p-p}}$ normalized for features of different widths with respect to the widest 50 µm one vary with the distance above the films (Table 3.1). The best agreement between experiment and calculation is achieved for the calculation which assumes a probe to sample distance of 25 µm. This is in excellent agreement with the estimated sample to probe distance (see above).

A comparison between the measured and calculated peak-to-peak magnetic induction at the determined scan height of 25 µm reveals that the average value of the remanent magnetization is about 1 T. This value is less than the value of 1.4 T, estimated for continuous (non-patterned) films [Demp.'07]. This reduction in the average value of remanence is attributed to local modifications in the crystallographic texture developed in films deposited on patterned substrates. Accordingly, both SEM imaging of the grain structure and a comparison between in-plane and out-of-plane hysteresis loops measured with an extraction magnetometer on an ensemble of motifs confirmed that these topographically patterned films are less well textured than continuous ones [O'Brien].

Table 3.1. Calculated and measured maximum, minimum, and peak-to-peak values of the z-component of the magnetic field above features of different widths; relative values normalized with respect to the 50 μm wide feature are also given.

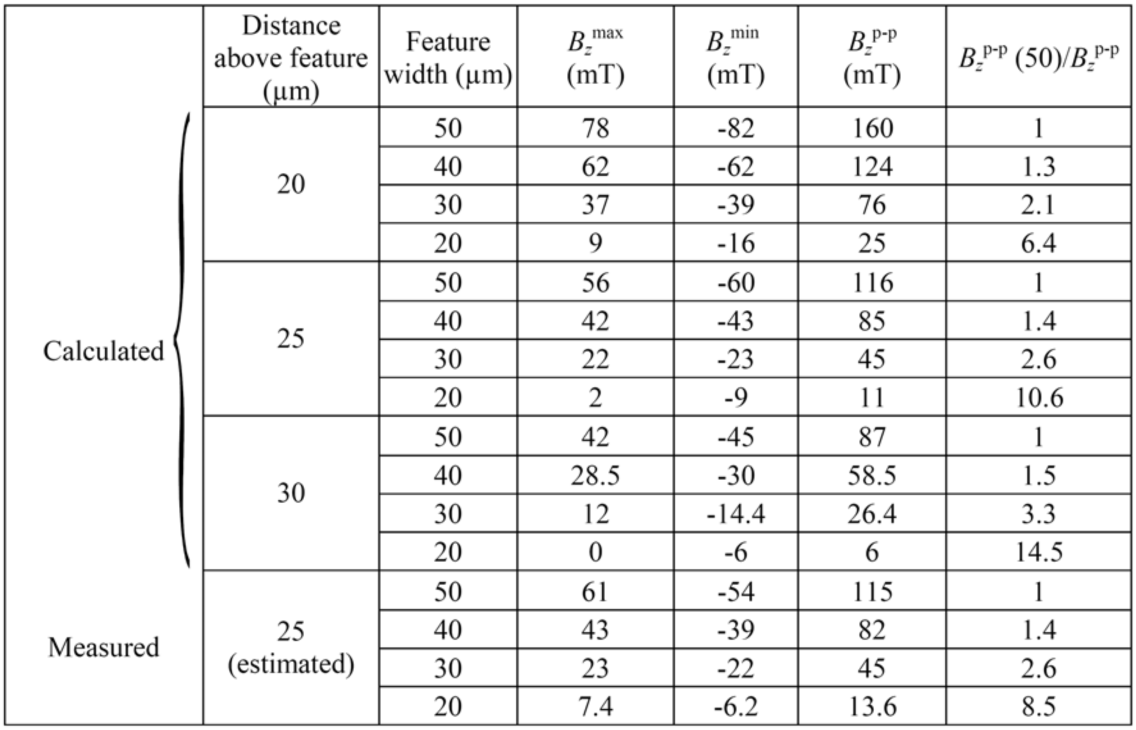

	Distance above feature (μm)	Feature width (μm)	B_z^{max} (mT)	B_z^{min} (mT)	$B_z^{\text{p-p}}$ (mT)	$B_z^{\text{p-p}}$ (50)/$B_z^{\text{p-p}}$
Calculated	20	50	78	-82	160	1
		40	62	-62	124	1.3
		30	37	-39	76	2.1
		20	9	-16	25	6.4
	25	50	56	-60	116	1
		40	42	-43	85	1.4
		30	22	-23	45	2.6
		20	2	-9	11	10.6
	30	50	42	-45	87	1
		40	28.5	-30	58.5	1.5
		30	12	-14.4	26.4	3.3
		20	0	-6	6	14.5
Measured	25 (estimated)	50	61	-54	115	1
		40	43	-39	82	1.4
		30	23	-22	45	2.6
		20	7.4	-6.2	13.6	8.5

3.3 Characterization of thermo-magnetically patterned films

Here the SHPM was used to measure the distribution of the magnetic field generated by 4 µm thick, thermomagnetically-patterned NdFeB films. Samples of two different patterns were investigated, one was patterned through a mask containing 50 µm wide stripes, the other one using a 100×100 µm^2 chessboard mask. Both samples were magnetized in the out-of-plane direction [Dum.'10].

The measured 2D distribution of the vertical component of the magnetic field produced by the stripe-like thermo-magnetically patterned film at a height of approximately 30± 3 µm above its surface is shown in Fig. 3.5 (a). The measurement step size is 5 µm. The chosen step size was determined by a compromise between the image resolution and the measurement time. Note that the spatial resolution of the measurement device is lower than the step size (5 µm), for it depends also on the probe-sample distance (30 µm) and the size of the probe's active area (40×40 µm^2). The field profile measured along the line indicated in this image is plotted in Fig. 3.5 (b). The faint dark traces observed on the white stripes in the 2D image are due to unintentional interference patterns occurring during thermo-magnetic patterning [Dum.'10]. The non-monotonic variation in the peak intensities of the field profile can also be attributed to these interference effects. 2D distributions and field profiles at 30 µm from the film surface were calculated assuming that the sections of the hard magnetic film reversed during thermo-magnetic patterning are parallelepiped in shape (Fig. 3.5 (c)) and have the same value of remanent magnetization as the non-reversed sections, i.e. 1.4 T [Demp.'07]. In addition, the width of the transition zone between reversed and non-reversed sections was assumed to be zero. A 2D distribution calculated using the known physical parameters of the patterned film (number of stripes, stripe length, area of non-reversed film surrounding the stripes) is shown in Fig. 3.5 (d) and field profiles for different assumed depths of reversal are shown in Fig. 3.5 (e).

The increase in the peak-to-peak height towards the edges of the pattern in Fig. 3.5 (e) is due to the finite number of stripes while both the finite length of the stripes and the finite size of the non-reversed film surrounding the stripes lead to a vertical off-set. The overall shape of the calculated profiles (Fig. 3.5 (e) is in good agreement with the measured profile (Fig. 3.5 (b). From the comparison between the peak-to-peak field values of the experimental and calculated field profiles it is deduced that approximately 1.3 ± 0.2 µm of the film was reversed during thermo-magnetic patterning. The 15% error in this evaluation is due to (i) the uncertainty in the estimate of the probe to sample distance and (ii) to the fact that the reversed volume was assumed to be a parallelepiped. This reversal depth agrees relatively well with the value of 1.2 ± 0.3 µm, estimated by comparing the average remanent magnetization of the as-irradiated film (M_r^i) with the average remanent magnetization measured following saturation in a field of 8 T (M_r^s), measured in a vibrating sample magnetometer [Dum.'10].

In the calculations presented above, the sensor's active area was taken into account by assuming that the sensor response is proportional to the average magnetic field in the active area (total magnetic flux divided by the active area). Since the size of the active area is comparable with the size of the pattern's features, there is a noticeable difference in the field values as calculated taking into account the averaging effect of the sensor and as calculated for the case of a point sensor (Fig. 3.6). Due to this difference when the finite size of the Hall sensor active area is not taken into account, the reversal depth is estimated to be 1.1 ± 0.2 µm.

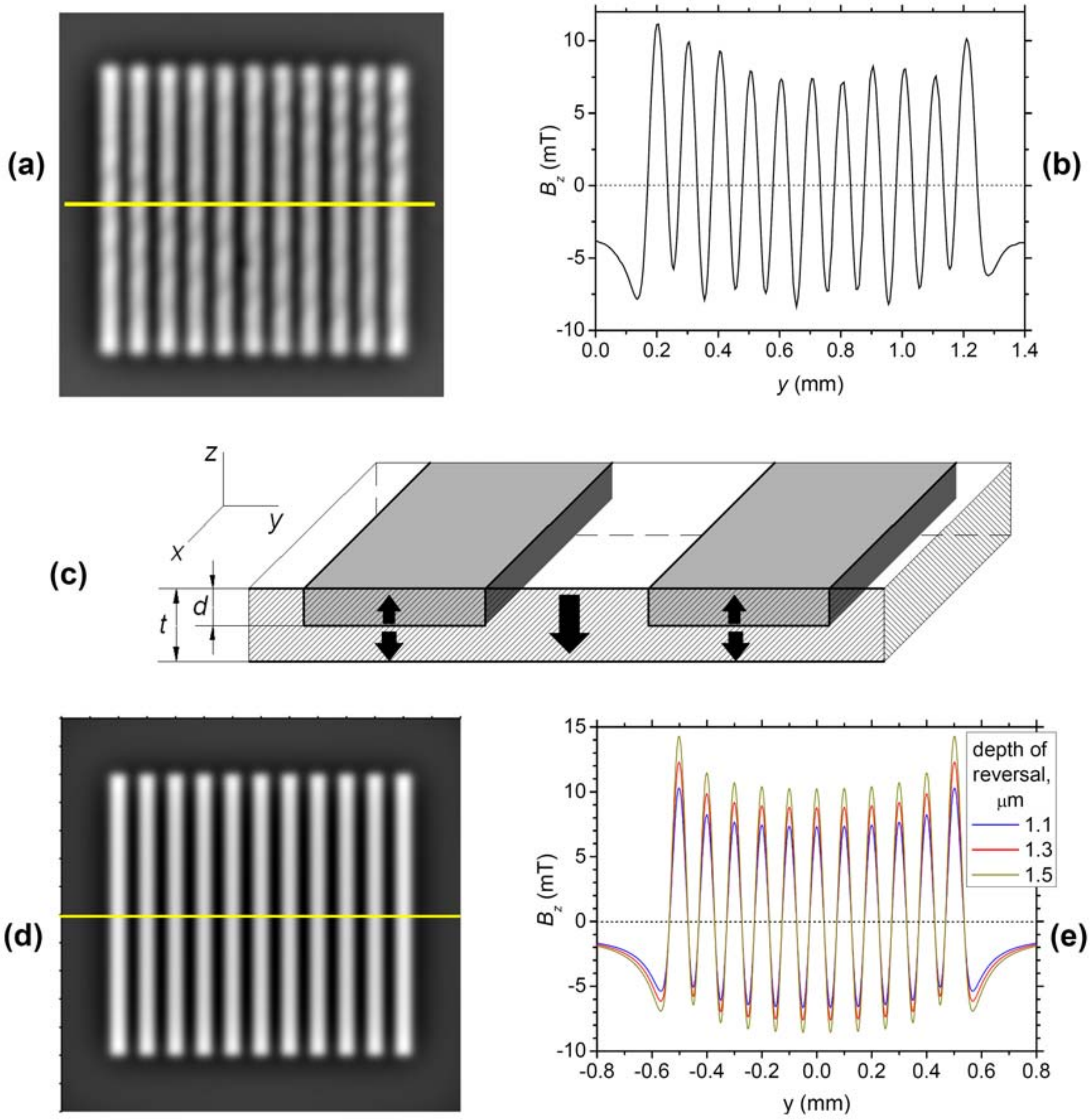

Fig. 3.5. (a): SHPM image of the out of plane component of the magnetic field pattern measured at 30 μm above the surface of a thermo-magnetically patterned 4 μm thick Nd-Fe-B film. (b): Field profile along the line indicated in (a). (c): Schematic representation of the structure assumed for analytical calculation of the stray field patterns produced by the thermo-magnetically patterned film. (d): Analytically simulated 2D image of the sample with the parameters as in (a). (e): 1D field profiles of (d) calculated for different assumed depths of magnetization reversal.

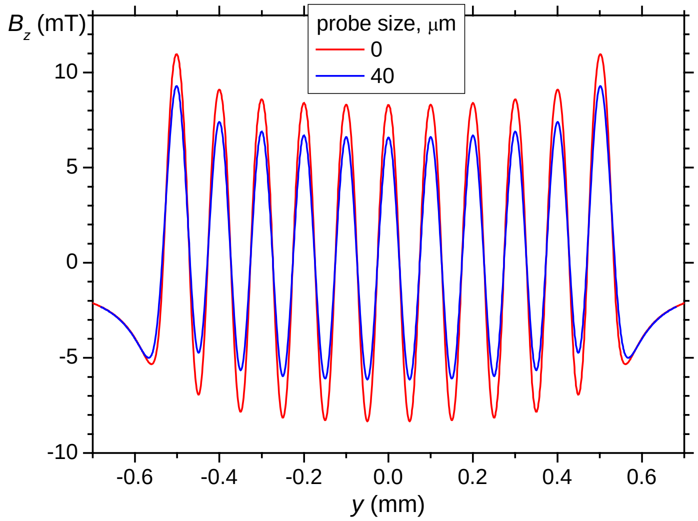

Fig. 3.6. Field profiles along the yellow line on Fig. 3.5 (d) calculated for a point sensor (red) and for a 40×40 μm^2 sensor averaging the field over its size (blue) for the assumed depth of reversal = 1 μm.

Similar measurements and calculations, and the analysis based on their comparison, was done for the chessboard-like thermomagnetically patterned film. Fig. 3.7 is analogous to the Fig. 3.5 presented before. On the 2D image of the measured field distribution Fig. 3.5 (a) the interference effects can be clearly seen on the non-patterned part of the sample. The observed increase of the edge peaks of the field profile (Fig. 3.5 (b)) is due to the finite overall size of the pattern. The depth of reversal was also deduced from the comparison between the peak-to-peak field values of the experimental (Fig. 3.5 (b)) and calculated (Fig. 3.5 (e)) field profiles and for this sample it is estimated to be approximately 1.1 ± 0.2 μm.

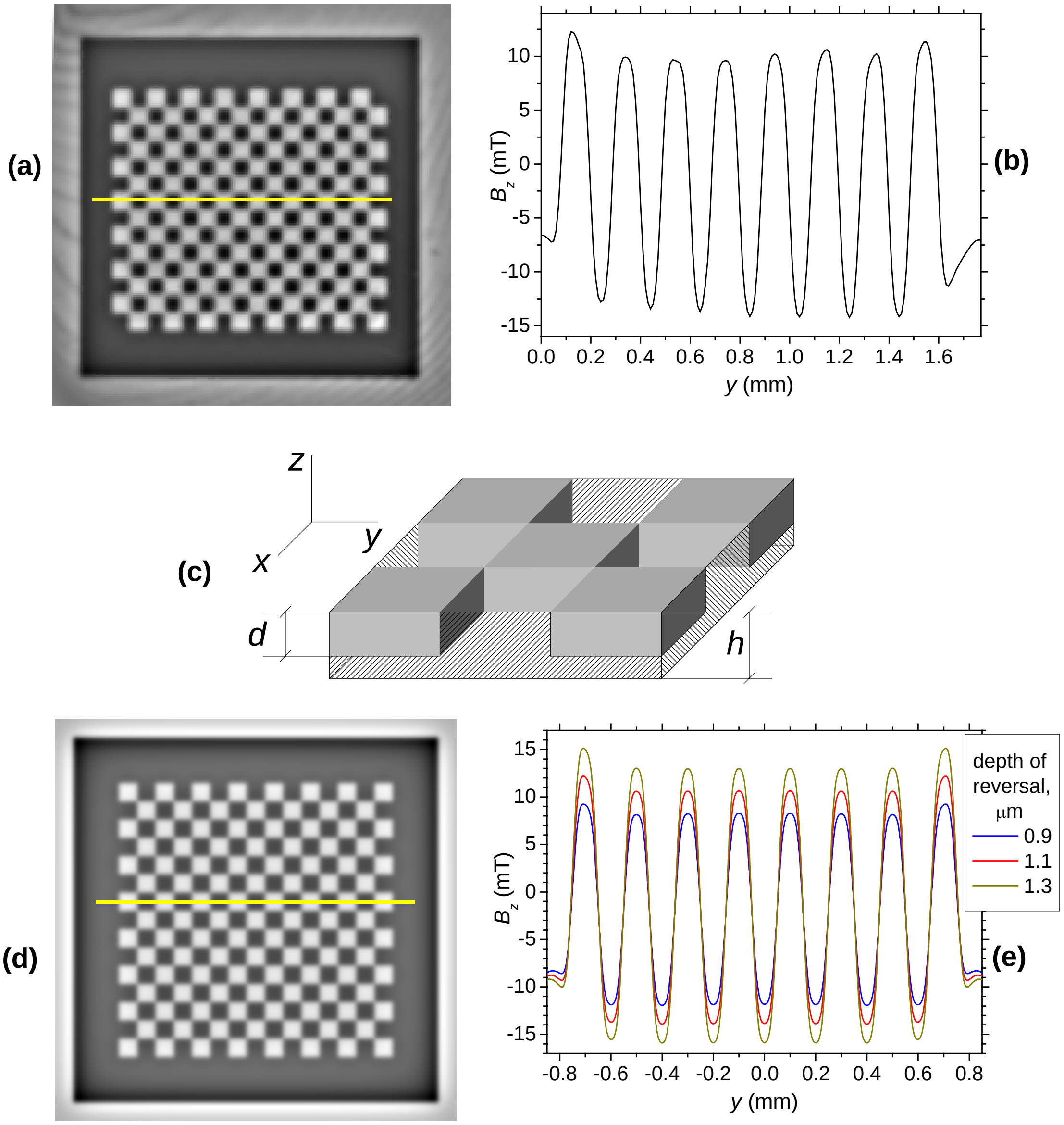

Fig. 3.7. (a): SHPM image of the out of plane component of the magnetic field pattern measured at 26 μm above the surface of a thermo-magnetically patterned 4 μm thick Nd-Fe-B film. (b): Field profile along the line indicated in (a). (c): Schematic representation of a fragment of the structure assumed for analytical calculation of the stray field patterns produced by the thermo-magnetically patterned film. (d): Analytically simulated 2D image of the sample with the parameters as in (a). (e): 1D field profiles of (d) calculated for different assumed depths of magnetization reversal.

Note that the averaging effect of the probe (Fig. 3.8) is almost not visible for this sample, since the size of the active area is more than twice smaller than the size of the pattern's features (100×100 μm^2).

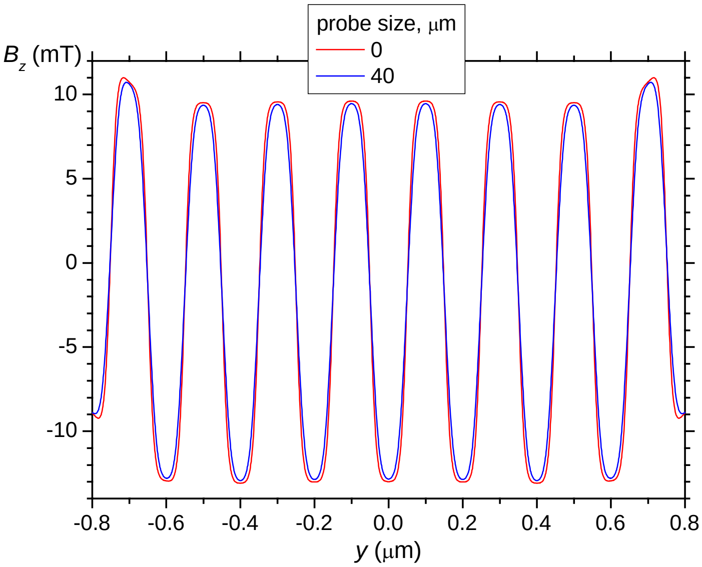

Fig. 3.8. Field profiles along the yellow line on Fig. 3.7 (d) calculated for a point sensor (red) and for a 40×40 μm^2 sensor averaging the field over its size (blue) for the assumed depth of reversal = 1 μm.

3.4 Derivation of the field and field gradients generated by the micro-patterned hard magnetic films

The micro-magnet arrays reported here are of particular interest for lab-on-chip applications, such as the trapping of biological species (liposomes, cells, bacteria…) tagged with magnetic nanoparticles [Gijs ’07], or the levitation / confinement of diamagnetic objects (cells, water droplets…) [Lyuks.’04, Frén.’08]. The strength of the field and the field gradient produced by a hard magnet varies strongly with distance from the magnet and it is important to quantify these parameters at the relevant length scales. The values of the *z*-component of the magnetic field, measured at one given sample-to-probe distance, have been used to derive the modulus of the magnetic field ($B = |\mathbf{B}| \equiv \sqrt{B_x^2 + B_y^2 + B_z^2}$), and two components of its gradient: $\partial B/\partial z$ and $\partial B/\partial y$ at three different distances (0.1, 1 and 10 µm) above the micro-magnet arrays (Fig. 3.9). These distances were chosen because the typical size of the magnetic nanoparticles used for tagging is in the range 10-100 nm, while that of bacteria and cells is of the order of 1 µm and 10 µm, respectively. The calculations were made above the central micro-magnet of the stripe-like thermomagnetically patterned array and the central 50 µm wide micro-magnet of the topographically patterned array, with the entire arrays being taken into consideration. In the calculations the same assumptions concerning the micro-magnet geometry described in section 3.2 and 3.3 were made.

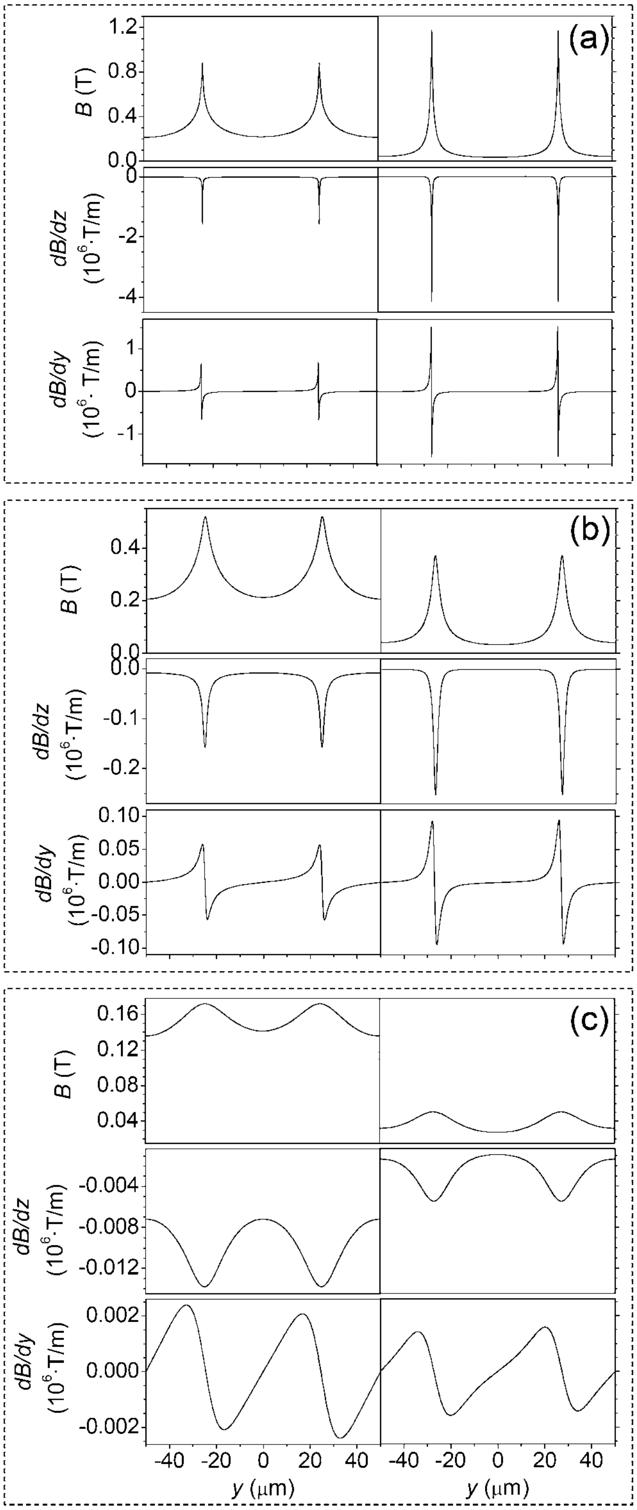

Fig. 3.9. B, ∂B/∂z and ∂B/∂y profiles calculated at distances z = 0.1, 1 and 10 μm ((a), (b) and (c) respectively) above the central micro-magnet, with the entire array being taken into consideration; left hand column – topographically patterned film of thickness 38 μm (above the central 50 μm wide micro-magnet), right hand column – thermomagnetically patterned film of effective thickness 1.3 μm.

The idealized straight-walled sharp-cornered geometry and the assumption of perfectly uniform magnetization in the films most probably leads to an overestimation of the values of field and field gradient, especially at the closest distance. Nevertheless the comparison of fields and field gradients at different heights above the structures may be considered to be instructive. In future work finite element analysis will be used to simulate structures that emulate the observed structure shape.

At the closest distance of 0.1 μm, the values of the field modulus and field gradients are maximum for the thermomagnetically patterned film ($B = 1.1$ T; $\partial B/\partial z = -4.1\times10^6$ T/m; $\partial B/\partial y = \pm1.5\times10^6$ T/m). For both structures significant fields and gradients are produced only at the edges of the micro-magnets, because of the effect of nonuniform demagnetizing field distributions inherent in non-ellipsoidal bodies [Joseph '65]. At larger distances (1 and 10 μm), the value of the field modulus is greater for the topographically patterned film (maximum values: 0.5 T and 0.016 T, respectively). Only for the largest distance (10 μm), the field gradients are maximum for the topographically patterned film ($\partial B/\partial z = -0.014\times10^6$ T/m; $\partial B/\partial y = \pm0.002\times10^6$ T/m). This disparity reflects (i) the difference in film thickness (38 and 1.3 μm for the topographically and thermomagnetically patterned films, respectively), and (ii) the difference in their magnetic structure (the topographically patterned films are unidirectionally magnetized and physically separated by a gap, whereas thermomagnetically patterned micro-magnets are oppositely magnetized and in direct contact, i.e. the structure is fully compact). The much greater thickness of the topographically patterned films only becomes important for the largest distance considered (10 μm). In the case of trapping biological species tagged with magnetic nanoparticles, the thicker topographic films would act over a further distance, favoring the initial capture, while the bipolar thermomagnetically patterned magnets would better pin the trapped particles. Hybrid topographic-thermomagnetic structures could be used to optimize both the capture and trapping of magnetic nanoparticles.

3.5 Conclusions

SHPM has been used for the quantitative measurement of the stray magnetic fields produced by micro-patterned high performance hard magnetic films. Comparison of experimentally measured field patterns with calculated ones provides important information concerning the micro-magnets' internal magnetic structure. In the case of topographically patterned films, estimation of the average value of remanent magnetization revealed that deposition onto patterned substrates influenced the crystallographic texture achieved. In the case of thermo-magnetically patterned films, the depth of magnetization reversal was estimated. The patterned films characterized in this study generate fields with peak-to-peak z-component induction values in the range 20-120 mT at heights of 25-30 μm above the micro-magnet arrays. At these distances the field gradient values are of the order of 10^3 T/m increasing up to 10^6 T/m at the magnet surface. A comparison of the derived z-dependence of the field and field gradient profiles reveals the relative importance of the film thickness on one hand and the magnetic structure (non-compact unipolar structure vs. fully-compact bipolar structure) on the other hand.

Chapter4: Design of levitation systems

4. Design of levitation systems

4.1 Introduction

This chapter deals with the design of plate-like levitating systems, which have potential applications in a variety of micro-systems, such as shock sensors, inclinometers, accelerometers, micro-transporters etc. Two variants are considered. In the first case we deal with a diamagnetic body in levitation above an array of micro-magnets, in the second with the levitation of a micro-magnet above a diamagnetic substrate. By way of introduction, we recall the equations which are used to calculate the forces involved.

For the case of a diamagnetic plate in levitation above an array of micro-magnets, we have designed a novel “flying carpet” which can be stable in position either above or below the magnets. This is possible because in addition to the repulsive force between the diamagnetic plate and the magnet, we propose to induce an additional attractive force between the bodies by adding a layer of soft magnetic material to the outer side of the diamagnetic plate. Semi-analytical modeling was used to calculate the plate to track distance for the plate above and below the track.

For the case of a micro-magnet in levitation above a diamagnetic substrate, we have used modeling to optimize the magnet dimensions with respect to the maximum achievable levitation height and the maximum permissible load on the levitating magnet. Two variants were considered for the magnet: 1) unidirectional magnetization (single dipole) and 2) bi-directional magnetization (double-dipole). For the later, spacing between the two dipoles was also considered.

4.2 Forces in a magnetic field

To find the force acting on a paramagnetic or diamagnetic body in a magnetic field we will use the formulas for the force acting on a magnetic moment in a magnetic field, which can be found in textbooks on magnetism [Griff.'99].

The components of the force acting on a magnetic moment $\mathbf{p} = (p_{\mathrm{m}x}, p_{\mathrm{m}y}, p_{\mathrm{m}z})$ in a field $\mathbf{B} = (B_x, B_y, B_z)$ are

$$\begin{aligned} F_x &= p_{\mathrm{m}x}\frac{\partial B_x}{\partial x} + p_{\mathrm{m}y}\frac{\partial B_y}{\partial x} + p_{\mathrm{m}z}\frac{\partial B_z}{\partial x} = \mathbf{p}_{\mathrm{m}}\frac{\partial \mathbf{B}}{\partial x}, \\ F_y &= \mathbf{p}_{\mathrm{m}}\frac{\partial \mathbf{B}}{\partial y}, \\ F_z &= \mathbf{p}_{\mathrm{m}}\frac{\partial \mathbf{B}}{\partial z}. \end{aligned} \tag{4.2.1}$$

Knowing that in vacuum (or in air) the vectors of the magnetic field strength **H** and the magnetic field (magnetic induction) **B** are related by the following expression:

$$\mathbf{B} = \mu_0\mathbf{H} \qquad (4.2.2),$$

let's write (4.2.1) in terms of **H.**

$$\begin{aligned} F_x &= \mu_0\left(p_{\mathrm{m}x}\frac{\partial H_x}{\partial x} + p_{\mathrm{m}y}\frac{\partial H_y}{\partial x} + p_{\mathrm{m}z}\frac{\partial H_z}{\partial x}\right) = \mu_0\mathbf{p}_{\mathrm{m}}\frac{\partial \mathbf{H}}{\partial x}, \\ F_y &= \mu_0\mathbf{p}_{\mathrm{m}}\frac{\partial \mathbf{H}}{\partial y}, \\ F_z &= \mu_0\mathbf{p}_{\mathrm{m}}\frac{\partial \mathbf{H}}{\partial z}. \end{aligned} \tag{4.2.3}$$

When we place a magnetic material in a field it gets magnetized. An element dV of the magnetic material has a magnetic moment

$$d\mathbf{p}_{\mathrm{m}} = \mathbf{M}dV, \tag{4.2.4}$$

where **M** is the magnetization vector.

From (4.2.3) and (4.2.4) the components of the force acting on the element dV in a magnetic field $\mathbf{H} = (H_x, H_y, H_z)$ become:

$$dF_x = \mu_0\left(M_x \frac{\partial H_x}{\partial x} + M_y \frac{\partial H_y}{\partial x} + M_z \frac{\partial H_z}{\partial x} \right)dV = \mu_0 \mathbf{M} \frac{\partial \mathbf{H}}{\partial x} dV,$$

$$dF_y = \mu_0 \mathbf{M} \frac{\partial \mathbf{H}}{\partial y} dV, \tag{4.2.5}$$

$$dF_z = \mu_0 \mathbf{M} \frac{\partial \mathbf{H}}{\partial z} dV.$$

The magnetization components and the components of magnetic field strength are related via the material's susceptibility:

$$M_i = \chi_{ij} H_j, \tag{4.2.6}$$

here χ_{ij} are components of the tensor of volume magnetic susceptibility. The tensor can be diagonalized; then (4.2.6) can be rewritten as:

$$M_i = \chi_i H_i \text{ for } i = x, y, z. \tag{4.2.7}$$

Let's find the z component of the force acting on the volume element dV putting (4.2.7) into (4.2.5) (we will need the z-component when we will consider levitation systems in which this component 'fights' against gravity):

$$dF_z = \mu_0\left(\chi_x H_x \frac{\partial H_x}{\partial z} + \chi_y H_y \frac{\partial H_y}{\partial z} + \chi_z H_z \frac{\partial H_z}{\partial z} \right)dV. \tag{4.2.8}$$

Applying the so-called chain rule for the derivative of the composition of two functions

$$\frac{d}{dx} f(g(x)) = \frac{df}{dg}\frac{dg}{dx} \tag{4.2.9}$$

to the function $y^2(x)$

$$\frac{d}{dx} y^2(x) = 2y(x)\frac{dy(x)}{dx} \tag{4.2.10}$$

we can write:

$$H_i \frac{\partial H_i(x,y,z)}{\partial z} = \frac{1}{2}\frac{\partial H_i^2(x,y,z)}{\partial z} \text{ for } i = x, y, z. \tag{4.2.11}$$

Using this expression, (4.2.8) can be written in a more compact form:

$$dF_z = \frac{1}{2}\mu_0\left(\chi_x \frac{\partial H_x^2}{\partial z} + \chi_y \frac{\partial H_y^2}{\partial z} + \chi_z \frac{\partial H_z^2}{\partial z} \right)dV = \frac{1}{2}\mu_0 \frac{\partial}{\partial z}\left(\chi_x H_x^2 + \chi_y H_y^2 + \chi_z H_z^2 \right)dV. \tag{4.2.12}$$

Finally the force acting on the element dV of a paramagnetic or diamagnetic material in a magnetic field is

$$\boxed{\begin{aligned} &dF_z = \mu_0\left(\chi_x H_x \frac{\partial H_x}{\partial z} + \chi_y H_y \frac{\partial H_y}{\partial z} + \chi_z H_z \frac{\partial H_z}{\partial z}\right) dV = \\ &= \frac{1}{2}\mu_0\left(\chi_x \frac{\partial H_x^2}{\partial z} + \chi_y \frac{\partial H_y^2}{\partial z} + \chi_z \frac{\partial H_z^2}{\partial z}\right) dV = \frac{1}{2}\mu_0 \frac{\partial}{\partial z}\left(\chi_x H_x^2 + \chi_y H_y^2 + \chi_z H_z^2\right) dV. \end{aligned}} \tag{4.2.12'}$$

Expressions for the x and y components can be found in the same manner. The vector of the force can be written in this way:

$$\boxed{d\mathbf{F} = \frac{1}{2}\mu_0 \nabla\left(\chi_x H_x^2 + \chi_y H_y^2 + \chi_z H_z^2\right) dV}. \tag{4.2.13}$$

In the case of isotropic magnetic material the susceptibility components are equal:

$$\chi_x = \chi_y = \chi_z = \chi,$$

and (4.2.8) becomes:

$$dF_z = \mu_0 \chi\left(H_x \frac{\partial H_x}{\partial z} + H_y \frac{\partial H_y}{\partial z} + H_z \frac{\partial H_y}{\partial z}\right) dV = \mu_0 \chi\, \mathbf{H} \frac{\partial \mathbf{H}}{\partial z} dV\,, \tag{4.2.14}$$

Note that in fact:

$$\mathbf{H} \frac{\partial \mathbf{H}}{\partial z} = H \frac{\partial H}{\partial z}\,, \tag{4.2.15}$$

where H is the magnitude of the vector $\mathbf{H}$: $H = \sqrt{H_x^2 + H_y^2 + H_z^2}$.

To prove this let's write the right part of the equation in coordinates:

$$\begin{aligned} H \frac{\partial H}{\partial z} &= \sqrt{H_x^2 + H_y^2 + H_z^2}\, \frac{\partial \sqrt{H_x^2 + H_y^2 + H_z^2}}{\partial z} = \text{/using (4.2.9)/} \\ &= \sqrt{H_x^2 + H_y^2 + H_z^2}\, \frac{1}{2\sqrt{H_x^2 + H_y^2 + H_z^2}}\, \frac{\partial\left(H_x^2 + H_y^2 + H_z^2\right)}{\partial z} = \\ &= \frac{1}{2}\left(\frac{\partial H_x^2}{\partial z} + \frac{\partial H_y^2}{\partial z} + \frac{\partial H_z^2}{\partial z}\right) = H_x \frac{\partial H_x}{\partial z} + H_y \frac{\partial H_y}{\partial z} + H_z \frac{\partial H_z}{\partial z} \equiv \mathbf{H} \frac{\partial \mathbf{H}}{\partial z}. \end{aligned} \tag{4.2.15'}$$

For an isotropic material (4.2.12) becomes:

$$dF_z = \frac{1}{2}\mu_0\chi\left(\frac{\partial H_x^2}{\partial z} + \frac{\partial H_y^2}{\partial z} + \frac{\partial H_z^2}{\partial z}\right)dV = \frac{1}{2}\mu_0\chi\frac{\partial}{\partial z}\left(H_x^2 + H_y^2 + H_z^2\right)dV = \\ = \frac{1}{2}\mu_0\chi\frac{\partial H^2}{\partial z}dV. \tag{4.2.15}$$

Expression (4.2.12') takes a more compact form:

$$\boxed{dF_z = \mu_0\chi\,\mathbf{H}\frac{\partial \mathbf{H}}{\partial z}dV = \mu_0\chi\,H\frac{\partial H}{\partial z}dV = \frac{1}{2}\mu_0\chi\frac{\partial H^2}{\partial z}dV}. \tag{4.2.15'}$$

The vector of the force can be written as:

$$\boxed{d\mathbf{F} = \mu_0\chi\,H\,\nabla H dV = \frac{1}{2}\mu_0\chi\,\nabla H^2 dV}. \tag{4.2.16}$$

Energetic approach:

The same expressions can also be obtained using the energetic approach. The force acting on the volume dV can be expressed as

$$d\mathbf{F} = \nabla(\omega_1 - \omega_0)dV\,, \tag{4.2.17}$$

where ω_0, ω_1 are the energy densities in the volume dV before and after placing the paramagnetic (or diamagnetic) body in the same external field with the strength $\mathbf{H} = (H_x, H_y, H_z)$). They are given by:

$$\omega_0 = \frac{1}{2}\mathbf{B}_0\cdot\mathbf{H} = \frac{1}{2}\mu_0(\mathbf{H}\cdot\mathbf{H}). \tag{4.2.18}$$

$$\omega_1 = \frac{1}{2}\mathbf{B}_1\cdot\mathbf{H} = \frac{1}{2}\mu_0\left(\bar{\bar{\mu}}\mathbf{H}\cdot\mathbf{H}\right), \tag{4.2.19}$$

Note that here we assume that **H** before and after placing the paramagnetic (or diamagnetic) body is the same. In fact this is exact only if the magnetic material fills all the space, and hence the field **H** is generated by the same configuration of conduction currents and remains the same with or without a magnetic material thanks to Maxwell's equation for the vector **H**: rot**H** = **j**, where **j** is the density of the conduction current generating **H**. For a paramagnetic or diamagnetic body of finite size we make this assumption based on the fact that the demagnetizing field in this body is much weaker than the external field, hence it does not considerably change the external field configuration. Limiting ourselves to paramagnetic and diamagnetic materials we also assume that the material does not saturate in any field **H**.

For a symmetric tensor $\overline{\overline{\mu}}$ with the diagonal components μ_x, μ_y, μ_z

$$\begin{aligned}\omega_1-\omega_0 &= \frac{1}{2}\mu_0\left(\mu_x H_x^2+\mu_y H_y^2+\mu_z H_z^2\right)-\frac{1}{2}\mu_0\left(H_x^2+H_y^2+H_z^2\right)=\\ &=\frac{1}{2}\mu_0\left((\mu_x-1)H_x^2+(\mu_y-1)H_y^2+(\mu_z-1)H_z^2\right)=\\ &=\frac{1}{2}\mu_0\left(\chi_x H_x^2+\chi_y H_u^2+\chi_z H_z^2\right).\end{aligned} \tag{4.2.20}$$

And the force

$$\boxed{d\mathbf{F}=\nabla(\omega_1-\omega_0)dV=\frac{1}{2}\mu_0\nabla\left(\chi_x H_x^2+\chi_y H_y^2+\chi_z H_z^2\right)dV} \tag{4.2.21}$$

which is in fact equal to formula (4.2.13).

The main conclusions, which can be made from the formulas for the force acting on a paramagnetic or diamagnetic material in an external magnetic field, are:

1. the force is proportional to the field and to the field gradient, =>
   - there is no force in a homogeneous magnetic field,
   - paramagnetic bodies ($\chi_i > 0$) are pushed from the areas of weak magnetic field to the areas of strong magnetic field, or in other words they are attracted by magnetic field sources.
   - diamagnetic bodies ($\chi_i < 0$) are pushed from the areas of strong magnetic field to the areas of weak magnetic field, or in other words they are repelled by magnetic field sources.
2. each component of the force depends on all the diagonal components (χ_x, χ_y, χ_z) of the magnetic susceptibility tensor, and on all the components of the magnetic field strength (H_x, H_y, H_z).
3. the force acting on an isotropic material is proportional only to the gradient of the field strength squared => the direction of the field does not matter.

Methods to increase the force:

1. using a material with k times higher susceptibility (all the components of the susceptibility tensor must be increased by k), keeping the source of magnetic field the same, increases the force by k.
2. increasing the magnetic field in every point occupied by the body by k, keeping the material and shape of the body the same, increases the force by k^2. If the field is generated by a system of permanent magnets, by increasing the remanent magnetization by a factor of k, the field generated by this system will increase by k in every point of space (as described in section 2.2). Thus increasing the remanence of magnets composing the source of magnetic field by k, the force increases by k^2.
3. downscaling a magnetic system by a factor of k, the magnetic field is preserved but its gradient increases by k and hence the volume force increases by k.

   In the case where the system works against gravity, like for levitation of diamagnetic bodies, the total force is determined by the difference of the magnetic levitation force and the gravitational force. Let f_{m1} and f_{g1} be the volume[1] magnetic levitation force (along the z direction) and volume gravitational force, respectively, before the downscaling of the system, and f_{m2} and f_{g2} - the volume magnetic force and volume gravitational force, respectively, after the downscaling. Then the total volume forces before and after downscaling are $f_{t1} = f_{m1} - f_{g1}, f_{t2} = f_{m2} - f_{g2}$. For the volume magnetic force, as we said, the following expression is valid:

$$f_{m2} = k f_{m1}.$$

The gravitational force will not change with changing of the dimensions of the object: $f_{g2} = f_{g1}$. So the total volume force[2] is:

---

[1] Volume force $f = \frac{\partial F}{\partial V}$.

[2] Total force acting on the whole body is:

$$F_{t2} = F_{m2} - F_{g2} = \frac{1}{k^2} F_{m1} - \frac{1}{k^3} F_{g1} = \frac{1}{k^3}\left(kF_{m1} - F_{g1}\right).$$

$$f_{t2} = k\, f_{m1} - f_{g1}.$$

Therefore, the magnetic force becomes more and more important in comparison with gravity, with decreasing the dimensions of the system [Cug.'03].

4.3 Modeling a ‘flying carpet’ stable in both the positive and negative z-directions

Plate levitation systems find potential applications for a variety of micro-devices such as shock sensors, inclinometers, accelerometers [Garm.’07], sensors for micro-robotics, and also may be potentially used as “carts” for transporting micro-particles within micro-factories. The levitation of such structures relies on the exact equilibrium (vertical stability) between gravity and diamagnetic repulsion forces[1].

Applications of magnetic levitation using high-temperature superconductors (HTS) for transport systems are also in development [Schultz ’05]. In these devices a HTS can fly either above or below a track constituted from an array of magnets, due to a force appearing because of the flux pinning in the HTS that can compensate the weight of the levitated HTS. This ability to levitate both above and below the rail greatly expands the application range of the device.

We modeled a ‘flying carpet’ for microsystems, which has a similar ability to be stable both above and below a magnetic track. The modeled device is a superconductor-free, room-temperature micro-size levitating ‘carpet’ that requires no power supply and can be integrated. The device does not demand constant cooling as in the case of superconductor-based levitation. It could potentially be used for the transportation of micro-particles but can have other possible application as described below.

The device may potentially be compatible with several ways of manipulation and positioning along Ox, such as optical, magnetic, or dielectrophoresis, if the layer of binder is a dielectric.

Fig. 4.1 describes the proposed +/-Z stable levitation device. The "flying carpet" is a 30 μm thick plate of highly oriented pyrolytic graphite (HOPG), coated with stripes of soft magnetic material of thickness 15 nm. The “flying carpet” flies above a 50 μm thick permanent magnet film; this base is magnetically patterned into stripes, alternatively magnetized up and down.

---

[1] For levitation heights lower that 1 μm the Casimir force becomes important and in some cases even crucial [Kok.’10]. If the levitated object is in a high-density medium the buoyancy force has to be taken into account.

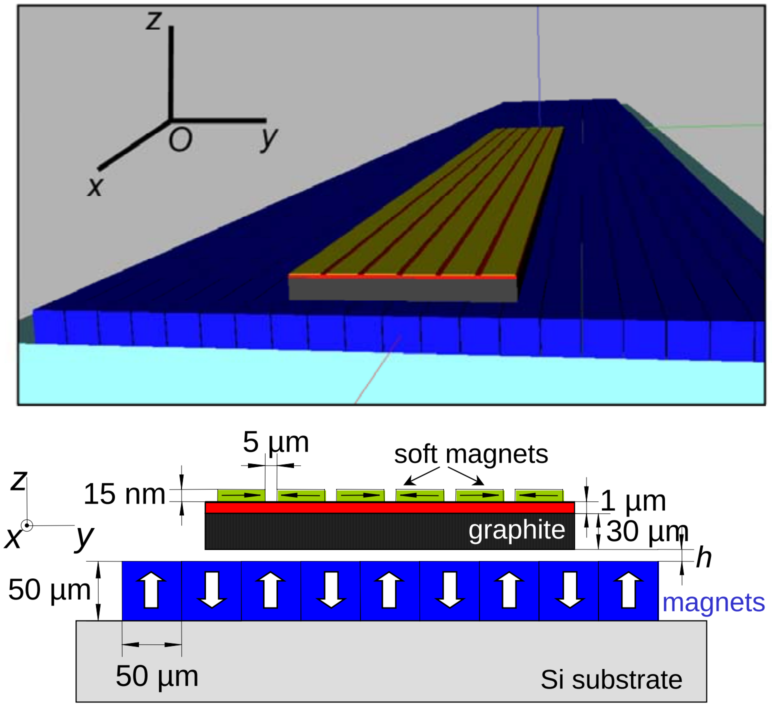

Fig. 4.1. Schematic view of the device, perspective view (top) and side view (bottom, not to scale). The array colored in blue is the permanent magnet film, magnetized in an up/down array (remanence 1.4 T). The middle layer (gray) is the micro-layer of HOPG (diamagnetic susceptibility $\chi_{\perp} = -450\cdot10^{-6}$, $\chi_{\parallel} = -85\cdot10^{-6}$) flying above the array of magnets. The stripes on top are the nano-layers of soft magnetic material (saturation magnetization $\mu_0 M_s = 1$ T) deposited onto the non-magnetic intermediate layer (colored in red), which itself is deposited onto the graphite plate.

For previously reported diamagnetic levitating devices (e.g. [Garm.'07]), the permanent magnet base has two functions. The main function is to provide important fields and field gradients (and hence resulting diamagnetic repulsion forces) so as to compensate against gravity, along the vertical (Oz) axis. The second additional function relies on the patterning and corresponding configurations along the Ox and Oy axes. Functions obtained for the levitating object are very variable, allowing possible rotation around Oz, or translations along Ox or Oy or both.

The present flying carpet levitates on stripe-like magnetization patterns, which allow one degree of freedom: Ox translation along the stripes.

4.3.1 Bi-directional stability along Oz

Previously reported diamagnetic devices do not work either upside-down or in zero gravity because the forces along Oz are purely repulsive. Our innovation is the addition of an array of 15 nm thin stripes of soft ferromagnetic material. The stripes are deposited onto a 1 μm layer of non-magnetic intermediate layer deposited onto the HOPG plate, on the far side from the magnets (this intermediate layer is added to the configuration only to simplify practical fabrication of the device). The ferromagnetic stripes generate an attractive force towards the base, which can stabilize the carpet along Oz.

Under gravity near the Earth’s surface, this possibility expands the freedom of usage of the device. In space or under low gravity conditions, the carpet will stay near the stable position from the magnetic base, so the device can be used as a sensor or for micro-transport even in space. A possible application as a mass sensor may use the resonance frequency of the carpet's oscillations along Oz, which depends on the suspended mass and hence on the mass of a particle stuck to the carpet.

The soft magnetic stripes help to guide the carpet along Ox, while improving the stability along Oy. Moving the carpet by 50 μm (the width of a permanent magnet element) along Oy will cause the magnetization inside a stripe to rotate by π (the model of magnetization of the stripes is described below in more detail). During this rotation a configuration with counter-domains within each stripe must appear, and such a domain configuration is strongly unfavorable energetically (this effect will depend on the chosen material).

The influence of the stripe’s in-plane form-factor on the carpet's in-plane angular stability was not considered in our work. This in-plane stability will depend on the material which can be magnetically anisotropic with an easy-axis anisotropy along Ox or Oy. To exclude the shape anisotropy of the soft elements in the xOy plane, each stripe may consist of smaller disks.

4.3.2 Modeling and optimization of the device

The force acting between the array of magnets and the diamagnetic element of the carpet, is repulsive and given by the formula (see section 4.2):

$$dF_z = \frac{1}{2}\mu_0\left(\chi_x\frac{\partial H_x^2}{\partial z} + \chi_y\frac{\partial H_y^2}{\partial z} + \chi_z\frac{\partial H_z^2}{\partial z}\right)dV \cdot \tag{4.3.1}$$

However, the force acting on the ferromagnetic nano-layer attracts the carpet towards the array of magnets; equation (4.3.2) shows the expression for the force acting on a unit volume of an isotropic magnetic element, in its saturated state with the saturation magnetization $\mathbf{M_s} = \left(M_{s_x}, M_{s_y}, M_{s_z}\right)$:

$$dF_z = \mu_0\left(M_{sx}\frac{\partial H_x}{\partial z} + M_{sy}\frac{\partial H_y}{\partial z} + M_{sz}\frac{\partial H_y}{\partial z}\right)dV \cdot \tag{4.3.2}$$

Here we assume that the nano-stripes of soft material are fully saturated in the alternate fashion shown on Fig. 4.1. Within the vertical displacement range of the carpet, the Y-component of magnetic field produced by the permanent magnet array (Fig. 4.2) is enough to saturate in the plane these very thin films made of soft ferromagnetic material (e.g. saturation field $\mu_0 H_s$ = 1 mT).

The stripes magnetization is supposed to be along Oy only:

$\mathbf{M_s} = (0, M_s, 0)$ or $\mathbf{M_s} = (0, -M_s, 0)$,

for odd and even numbers of stripe respectively.

The same approach was used by Furlani et al. in their works [Furl.'06, Furl.'07] where they calculated fields and forces generated by arrays of soft magnetic elemetns.

A misalignment of the saturation magnetization due to the presence of a Z-component of the external field was neglected. Taking into consideration a relatively high saturation magnetization $\mu_0 M_s$ = 1 T chosen for the simulation (significantly higher than the Z-component of the external field generated by the array of permanent magnets), even with magnetically isotropic material we have a strong “easy plane” shape anisotropy. It forces the vector of magnetization to be in the xOy plane. If needed, to increase the “easy plane” anisotropy, a material with high in-plane anisotropy can be chosen. The material must also be compatible with deposition techniques, and keep its ferromagnetic properties in a 15 nm layer.

Magnetic interactions between two neighboring stripes can be neglected. Calculations show that the value of the Y-component of stray magnetic field generated by a stripe (again assumed to be saturated along Oy) is less than 0.6 mT everywhere in the regions occupied by the neighboring stripes. Compare this value with the magnetic field generated by the array of permanent magnets, which is much higher than 0.6 mT (Fig. 4.2).

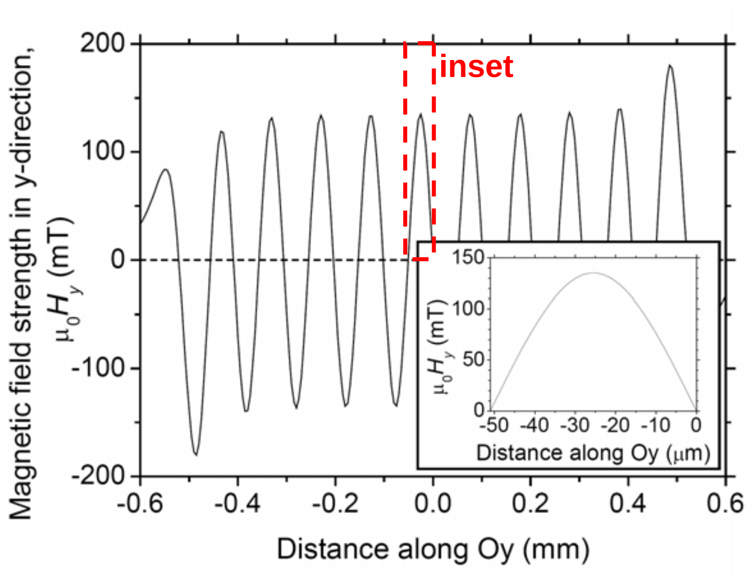

Fig. 4.2. Vertical component of magnetic field strength generated by the micromagnet base versus the distance along Oy at 30 μm (chosen maximum working range of displacement) above the permanent magnet base; inset: magnetic field strength profile in the region occupied by one stripe.

The stated assumptions allowed us to use the semi-analytical modelling and optimization tool MacMMEMS / CADES [Rak.'07] for the design of the device. This method gives a significant reduction in the calculation time compared to finite element simulations. It also helps to avoid the classical problems of FEM handling of materials of very low susceptibilities. Indeed, for such materials, FEM approximation can result in a loss of accuracy when calculating forces acting on paramagnetic and diamagnetic materials.

As can be seen from (4.3.1) and (4.3.2), the repulsive and attractive forces are functions of the partial derivatives of different powers of the magnetic field. Hence they decrease differently with the distance (Fig. 4.3). Also, they are not centered at the same point and can therefore intercept. This allows the compensation of these opposite forces at a fixed distance *h*. This distance is extremely dependent on geometrical parameters of the carpet layers, on the magnetic multipolar configuration of the base, and on the magnetic properties of the materials. For the proposed dimensions, the flying carpet would levitate at a stable position $h = 5.6$ μm above the base. That distance would decrease to 5.2 μm if gravity is taken into account, and 6.0 μm when upside-down (Fig. 4.4). Note that since the expected levitation height for both positions ('normal' and 'upside-down') is considerably higher than 1 μm, the Casimir force was not taken into account in the simulation.

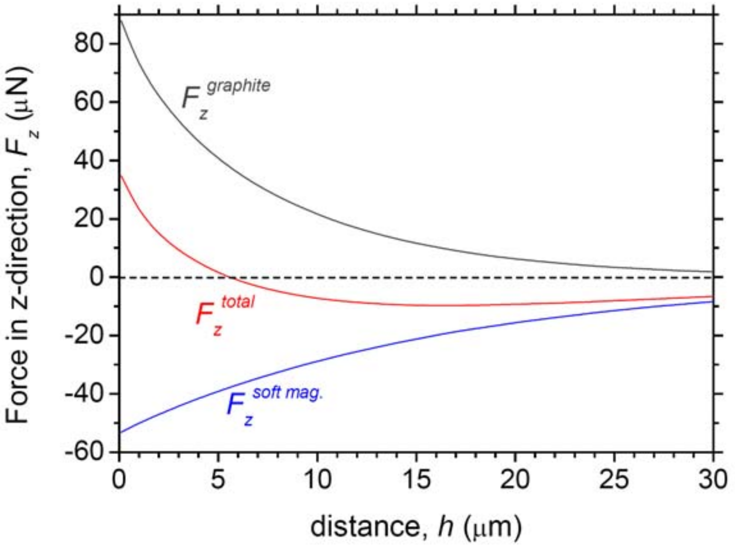

Fig. 4.3. Forces acting on the graphite layer, on the iron layer, and total force, versus the distance (airgap) between the levitating carpet and the magnet array (here gravity is not included).

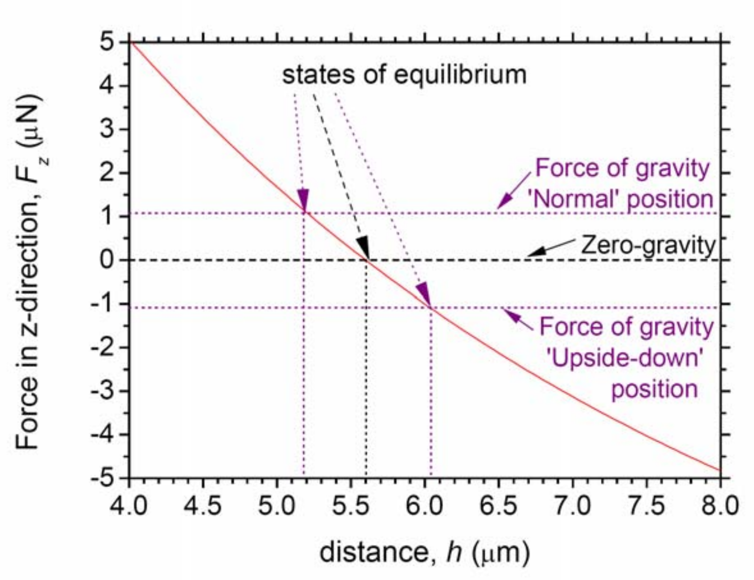

Fig. 4.4. Total magnetic force vs. airgap, compared with the gravitational force.

As can be seen from Fig. 4.3, the total magnetic force (both positive and negative) acting on the flying carpet is much higher than the gravitational force (1.1 μN on Earth) within a 30 μm distance range (chosen working range of displacement).

The simulation presented here was done purely to prove the idea of a “carpet” stable in both the positive and negative z-directions. The magnetic array was not especially optimized for this system; neither were the material properties of the soft material used in the simulation. However, an optimization of the graphite layer thickness and the thickness of the soft magnetic stripes was performed in order to achieve compensation of the repulsive and attractive forces and ensure a “decent” displacement range of the levitating body.

The optimization was done in the CADES framework where sensitivities of constrained specifications to the geometric parameters were automatically computed from algebraic equations of the model. A sequential quadratic programming (SQP) algorithm was used in order to find the best solution [Rak.’07].

This kind of device could be used in micro-robotics for transporting micro-objects and nano-particles, as well as for friction-less 3D micro-sensors (acceleration, rotation…) both on Earth and in space under low-gravity conditions.

It must be said that before making a prototype of the device a lot of optimization work will be needed, using the parameters for available magnetic arrays and taking into account the properties of the materials (soft magnetic stripes and diamagnetic substrate), available for making and integrating such a device. Though we showed that in principle this device should work, we do not claim that its fabrication would be easily doable.

4.4 Shape optimization of a levitating magnet

If in the previous section we described a levitation system where the flying part was a diamagnetic sheet, in this section we will view another kind of diamagnetic levitation: levitation of a permanent magnet above a diamagnetic substrate. This kind of levitation system may have the same applications as a system of the former type: shock sensors, inclinometers, accelerometers, sensors for micro-robotics and transporting micro-particles. Since the flying part is a magnet it can be more easily manipulated by magnetic fields than a diamagnetic body, and its position can be found using magnetic field sensors. It obviously expands the ways of manipulating the flying object and its detection. However, this kind of levitation is not easily achievable, for the flying object is a magnet, and hence it has much higher density than graphite. Because the flying object is heavy it must be small enough to make the magnetic force able to overcome gravity. In the next two sections we will answer the questions: how small it must be, and what the optimal geometry for a square magnet must be in order to maximize the levitation height and in order to maximize the permissible load at a given levitation height.

4.4.1 Maximization of the levitation height

The work described in this section was done in collaboration with Jaap Kokorian (M2 student, MESA+, University of Twente, The Netherlands).

The aim of the work described here is to find the optimal geometry for a magnet flying above a sheet of HOPG, providing the maximum levitation height. This kind of optimization is important most of all for demonstration of the feasibility of levitation systems. We want the magnet to fly as high as possible, because the higher it flies, (i) the easier to detect the fact of levitation and (ii) the lower the requirements for the quality of the substrate surface.

Unidirectionally magnetized (single-dipolar) magnets

The chosen magnet is a Nd-Fe-B magnet with remanence 1.4 T, magnetized along OZ, density 7400 kg/m^3, and of the shape of parallelepiped with a square base. The graphite substrate’s dimensions are 10x10x1 mm, the size corresponds to the typical size range for commercial HOPG plates. In fact in most cases the substrate will be considerably larger than the typical sizes of our magnets, and can thus be considered infinitely large within the error of 2%[1]. The OOP and IP components of the magnetic susceptibility tensor are $\chi_\perp = -450.10^{-6}$, $\chi_\parallel = -85.10^{-6}$. A schematic diagram of the system is shown in Fig. 4.5

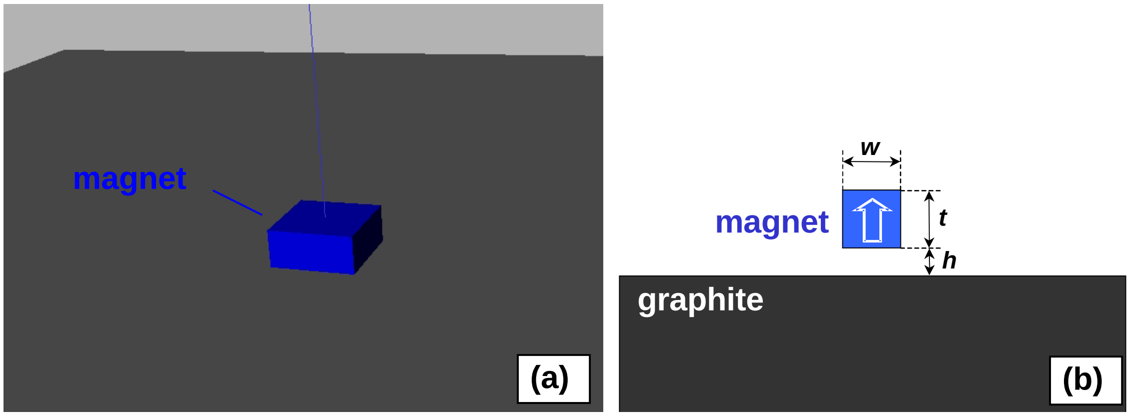

Fig. 4.5. Schematic diagram of the system: (a) perspective view, and (b) side view.

Only two forces acting on the flying magnet were considered: magnetic (levitation) force and gravitational force. The magnetic force was calculated with the aid of MacMMEMS / CADES framework. The levitation height was obtained from the equilibrium equation:

$$F_m(h) = F_g, \tag{4.4.1}$$

where F_m is the magnetic force, F_g is the gravitational force and h is the levitation height.

---

[1] No calculation is needed to say that the larger the diamagnetic substrate the larger the force between the substrate and the magnet. But since the magnetic field generated by a magnet decreases fast, the infinitely large substrate causes only 1.7 % larger force for a square magnet of the optimal geometry at the levitation height, than the substrate used in our simulation.

The equation was solved numerically using the bisection method (the script was written in Python by Jaap Kokorian).

The force F_m was calculated for a variety of magnet widths (w) and magnet thicknesses (t), then using formula (4.4.1) the levitation height (h) was found for each combination. Fig. 4.6 shows graphs of the levitation height vs. magnet's width for different thicknesses of the magnet. Such curves were used to draw a graph of largest levitation height vs. magnet's thickness (Fig. 4.7).

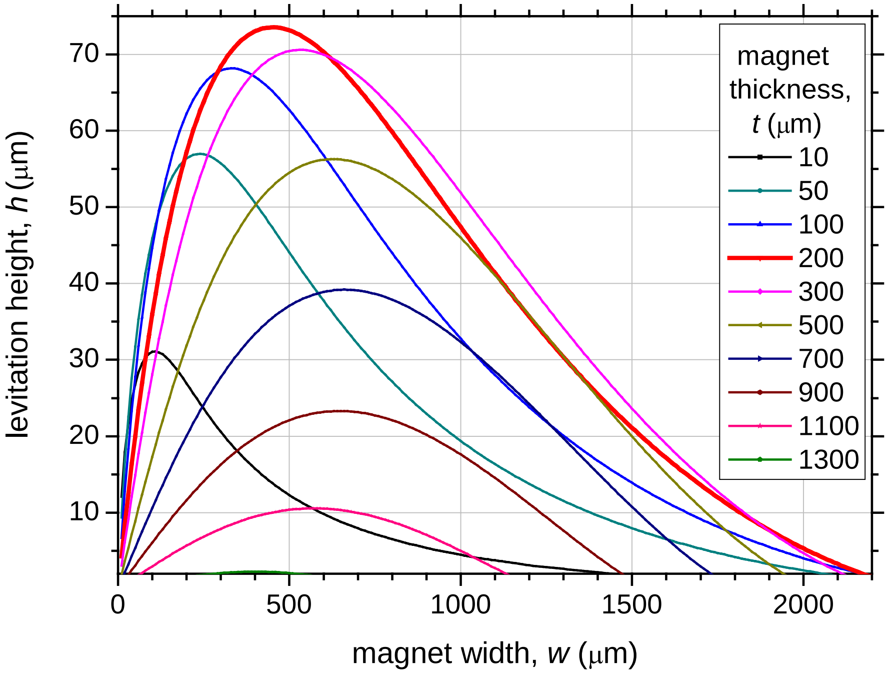

Fig. 4.6. Levitation height vs. magnet width for different magnet thicknesses.

It can be seen from the graphs that a magnet with the thickness in the range between 120 and 310 μm flies at a height above 70.0 μm, the best magnet thickness being around 200 μm. For a magnet of such thickness, widths from 320 to 610 μm give the levitation height above 70 μm. The highest value of levitation height 73.5 μm is achieved for the width = 450 μm.

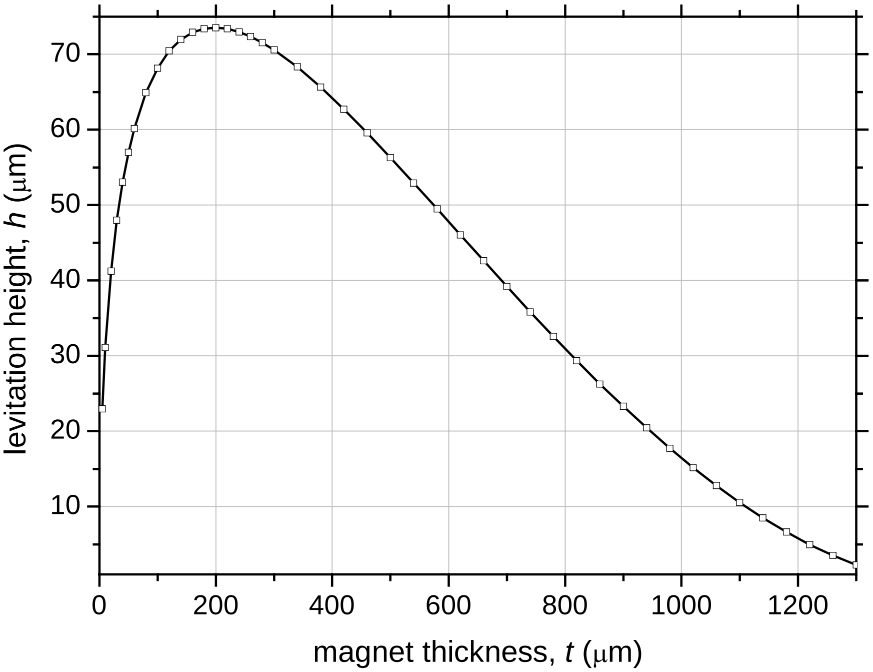

Fig. 4.7. Levitation height vs. magnet thickness for the optimal magnet width for each magnet thickness.

So the optimal dimensions for a Nd-Fe-B magnet unidirectionally magnetized out-of-plane ($B_r = 1.4$ T), to maximize its levitation height above a HOPG plate are: width = 450 μm, thickness = 200 μm[1]. Unfortunately these dimensions are not very convenient for fabrication of such a magnet. It is too thin for typical sizes of sintered Nd-Fe-B magnets and too thick for film magnets.

While for a levitation system where the flying part is a sheet of diamagnetic material, decreasing the thickness of this sheet (keeping the source of magnetic field the same) we will increase the levitation height[2], the levitation system with a flying magnet behaves differently. The fundamental difference is that the flying object is at the same time the source of magnetic field. To make this kind of levitation possible we need a small magnet but to get the maximum levitation height the magnet must not be too

---

[1] Note that if the diamagnetic substrate is made of bismuth, which has less diamagnetic susceptibility than HOPG ($\chi_x = \chi_y = \chi_z = -165.10^{-6}$), the optimal dimensions for a magnet are 250x250x100 μm, and the levitation height is 40 μm [Kok.'10].

[2] to a certain limit corresponding to the case when the thickness is infinitely small

small. Note that this does not go against the statement we made earlier, that in terms of levitation force the smaller the object the better, if we do not forget that we have to downscale everything. If we divide the values of levitation height from Fig. 4.7 by the corresponding magnet thickness we will get Fig. 4.8. A magnet thinner than 60 μm flies at a height more than its own thickness, while a magnet thicker than 60 μm flies at a height less than its own thickness. A grasshopper does not jump higher than a man but it leaps several times its own length (up to 20 times) while a man jumps only approximately one time his height[1].

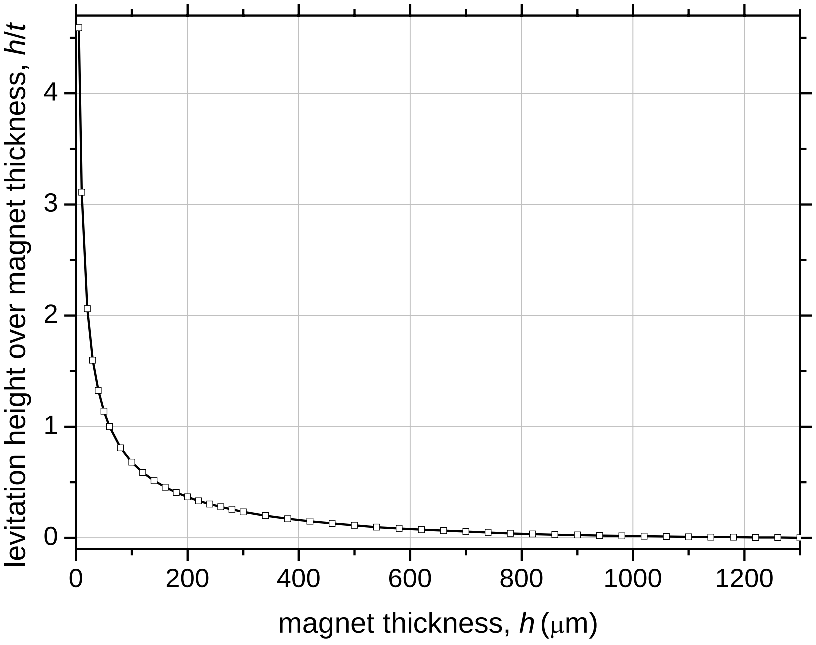

Fig. 4.8. Maximum levitation height divided by the corresponding magnet thickness vs. magnet thickness.

---

[1] Olympic champion Stefan Holm jumped 240 cm, being 181 cm tall

Double-dipolar magnets

Let's now have a look what will happen if we use a double-dipolar configuration (Fig. 4.9). Such a system was studied in an article by Harald Profijt et al. [Prof.'08].

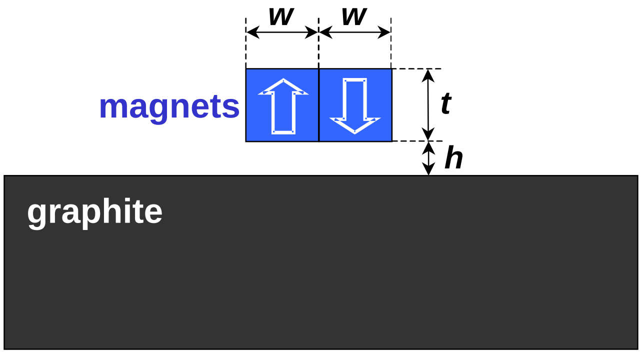

Fig. 4.9. Schematic diagram of a double-dipolar magnet. Side view.

Calculations show that the levitation height in this case will decrease to 62.5 µm. If we separate the magnet in two, each half will fly at 67 µm. If we take two square magnets of the optimal geometry and join them to form a double-dipole, the levitation height will be 76.7 µm. If we separate the two magnets, maintaining a distance between them with the aid of a weightless holder, the levitation distance of the pair does not always decrease. In fact at a separation distance of 114 µm the levitation height is maximal (81 µm). So multipolar magnetic configurations can increase the levitation height, and the effect is enhanced if the elements are separated from each other by a certain distance filled with very lightweight separator.

Influence of the orientation of magnetization

If a magnet with the optimal dimensions (200 µm thick and 450 µm wide) is magnetized along the OX (or OY) axis (Fig. 4.10), the levitation height is only 28 µm (as opposed to the magnet magnetized along OZ, which has the levitation height = 73.5 µm)[1]. The lower levitation height means that that this configuration has a lower energy. If our levitating object is sphere shaped, the stable equilibrium happens when the sphere is oriented with the magnetization vector parallel to the surface of the diamagnetic substrate. This orientation would produce the smallest levitation height. In contrast, the orientation with the magnetization vector normal to the substrate surface will correspond to the largest levitation height, however this equilibrium position will not be stable (for a sphere-shaped magnet).

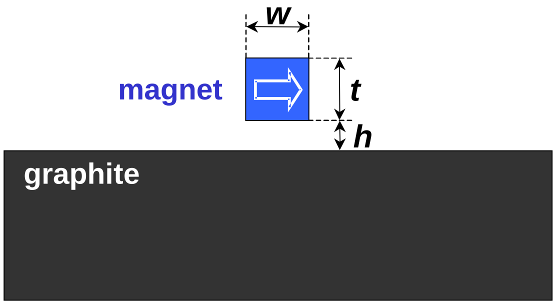

Fig. 4.10. Schematic diagram, side view. The magnet is magnetized parallel to the surface of the graphite substrate.

However, when a magnet has a sheet-like shape its levitation can be stable even if it is magnetized along OZ. Later on we will experimentally prove the possibility of stable levitation of a magnet unidirectionally-magnetized along OZ above an HOPG substrate.

---

[1] A magnet with these dimensions was optimal when it was magnetized along OZ axis, but it does not mean the same dimensions will be optimal in the case when the magnet is magnetized along OX or OY axis.

4.4.2 Maximization of the permissible load

In this section we will find the best dimensions for a square Nd-Fe-B magnet magnetized along OZ, flying above the same HOPG substrate as described in the previous subsection, providing the heaviest permissible load, at a given distance from the substrate.

The equilibrium equation is:

$$m_m g + m_l g = F_m , \tag{4.4.2}$$

where m_m is the mass of the magnet, m_l is the mass of the load (the load must not to be ferromagnetic), F_m is the magnetic force acting on the magnet.

Our aim is to maximize the load:

$$m_l = \frac{F_m - m_m g}{g} , \tag{4.4.3}$$

varying the width (w) and thickness (t) of the magnet (the notation is the same as shown in Fig. 4.5).

The optimization was done with the aid of the CADES framework using the SQP algorithm [Rak.'07]. One optimization with a laptop PC (Intel Celeron M1.7) took 12 iterations (less than 30 seconds per iteration).

Unidirectionally magnetized (single-dipolar) magnets

For the levitation height h = 10 µm, the optimal dimensions are: $w \approx 1050$ µm, $t \approx 460$ µm.[1] Such a magnet can carry 1.6 mg at this distance, i.e. around 43% of its own mass. The levitation height of this magnet without a load would be around 45.5 µm. Optimizations were done for a variety of levitation heights (see Table 4.1).

As you can see the optimal dimensions for a magnet become smaller with increasing levitation height.

---

[1] Note that for an infinitely large HOPG substrate (in the main text the substrate was of the size 10x10x1 mm), the optimal dimensions are: $w \approx 1080$ µm, $t \approx 475$ µm.

Table 4.1. Optimal dimensions for a magnet levitating at different heights from a HOPG substrate, allowing the heaviest permissible load that the magnet can carry.

Lev. height (μm)	Magnet width (μm)	Magnet thickness (μm)	Load (mg)	Lev. height without a load (μm)
10	1050	460	1.6	45.5
20	950	440	1.0	51.5
30	870	400	0.7	57.0
40	790	370	0.4	61.5
50	700	330	0.2	66.5
60	615	285	0.1	70.0
70	500	230	0.02	73.2

Double-dipolar magnets

If we use a double-dipolar magnet with the optimal dimensions for the levitation height 10 μm ($w = 1050$ μm, $t = 460$ μm), the permissible load increases up to 4 mg, which is in fact larger than the weight of the sum of the two magnets themselves. Without a load the levitation height would be 65 μm, so the double-dipolar configuration looks favorable in this case. However if we make a double-dipolar configuration from a magnet with dimensions 500x500x230 μm, which was the best for the levitation height 70μm, this double-dipolar magnet will not fly at all at this distance, not to mention carrying a load.

If we take two magnets with $w = 1050$ μm, $t = 460$ μm and put them together in the double-dipolar configuration, the carrying weight at 10 μm will be 5 mg. The levitation height without a load will be 61 μm.

The optimal dimensions for a double-dipolar system made of two square magnets for the levitation height 10 μm are: magnet width $w = 1316$ μm, magnet thickness $t = 500$ μm, distance between the magnets $d = 11$ μm. Mass of the permissible load = 5.6 mg (42% of the mass of the magnets), the levitation height without a load is 48.5 μm Note that if we put the magnets together ($d = 0$), the optimal dimensions and the mass of load change by less than 0.5%.

If we take two magnets in the double-dipolar configuration with the width of each magnet w = 1050 μm, and vary the length of the magnets, the total force $F_t = F_m - m_m g$ steadily increases with the length (Fig. 4.11). So in principle this system can carry a load with any weight if the magnets are long enough. Note that for a single-dipolar magnet of width 1050 μm the total force reaches a maximum at the magnet's length of around the same value as its width. Thus the rule: *the longer the magnets the heavier the carried weight*, does not work for a unidirectionally magnetized magnet (at least for a magnet of the given width and thickness).

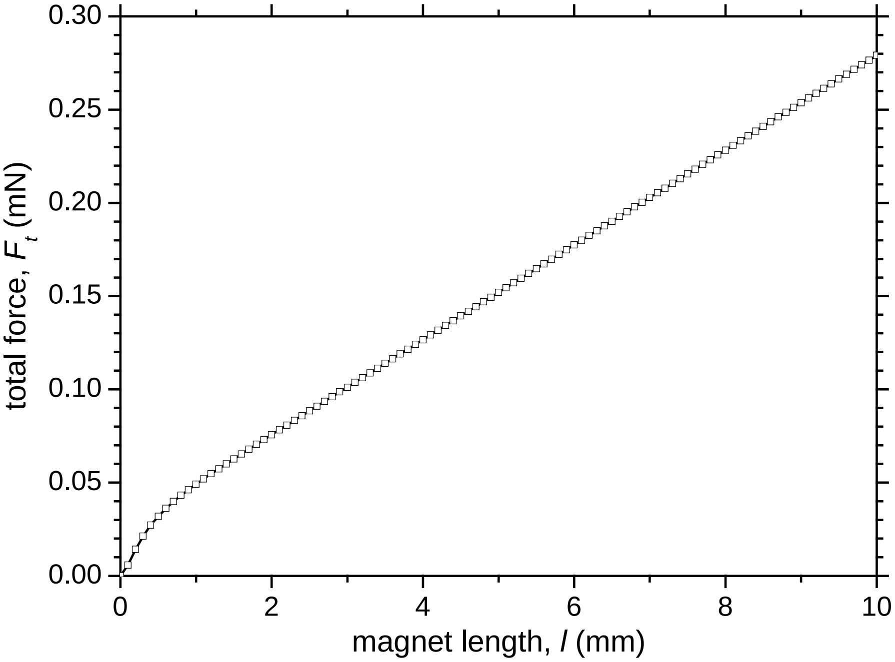

Fig. 4.11. Total force vs. magnet length for a double-dipolar configuration with fixed magnet width (1050 μm) at 1 μm from the HOPG upper surface.

To conclude, we may say that it is hard to deduce any definite rules about what kind of configuration is better for what. In some cases the double-dipolar configuration proves better, sometimes not. Even in a seemingly simple case of just two rectangular magnets, there are enough parameters to play with to make the problem quite complex. It seems that an optimization is needed for each particular case, whatever is changed: material, dimensions, load and so on.

4.5 Conclusions

In this chapter we have used semi-analytical calculations to model 2 distinct plate-like levitating systems. We have shown that, in principle, it should be possible to produce a diamagnet based “flying carpet” which is stable in position either above or below an array of hard magnets. Calculations indicate that a 30 μm thick plate of HOPG, coated with stripes of iron of 15 nm in thickness, would levitate at a height of 5.2 μm above a 50 μm thick hard magnetic film magnetized in a stripe like up/down pattern. When turned upside down, the plate would “fly” at a distance of 6.0 μm below the magnets. The ability to maintain a stable position for the diamagnetic/soft magnetic plate below a magnet track, is reminiscent of the way a superconducting body can be stabilized in position below a hard magnetic track by flux pinning. An advantage of the diamagnetic/soft magnetic system is that there is no need to cool the free body. Our novel design has not yet been tried experimentally. The preparation of HOPG in plate form of controlled size is expected to be challenging.

The second type of system considered concerned a micro-magnet in levitation above a diamagnetic substrate. We have shown how the levitation height varies depending on the magnet size and the magnetic configuration of the magnet. For a unidirectional out-of-plane magnetized magnet (single dipole) of square surface shape, the levitation height is maximum (73.5 μm) for a magnet thickness of 200 μm and width of 450 μm. Changing the direction of magnetization of such a magnet to in-plane, the levitation height drops to 28 μm. Going back to an out-of-plane direction of magnetization, but passing from a single to a double dipole configuration, while keeping the overall magnet dimension fixed, the levitation height drops to 62.5 μm. Breaking this magnet into two, according to the direction of magnetization, the levitation height of each individual magnet would be 67 μm. Forming a double dipole magnet with 2 dipole magnets of optimum size (i.e. , t = 200 μm and w = 450 μm), we would expect a levitation height of 76.7 μm. Finally, introducing a weightless spacer between the individual magnets, we could increase the levitation height to 114 μm. Finally, we have estimated the maximum permissible load which a magnet can support, for a given levitation height. This varies from 1.6 mg at 10 μm to 0.02 mg at 70 μm, for a single dipole magnet. Switching to a double dipole configuration, we can increase the load at 10 µm to 4 mg. These calculations serve as a guide to understand the influence of changing the magnet parameters.

Chapter 5: Diamagnetic levitation

5. Diamagnetic levitation

5.1 Introduction

In this chapter we will present some experimental results which are directly or indirectly related to diamagnetic levitation. The ultimate aim, not yet achieved, is to prepare model levitation systems in which we levitate objects of controlled shape and size. Such model systems would serve in the analysis of experimental diamagnetic levitation.

Since we are interested in the use of diamagnetic levitation in micro-systems, we restrict ourselves to the use of materials directly prepared at the micron scale. Both sputtering and electro-deposition have been used. In the first part we will present results concerning the levitation of a micro-magnet above a diamagnetic substrate. In the second section, we will present results concerning attempts to prepare a diamagnetic material (Bi), in a controlled shape (1D wires and 2D sheets), at the micron scale.

5.2 Levitation of a Nd-Fe-B free-standing film above highly oriented pyrolytic graphite

The work described in this section was done in collaboration with Jaap Kokorian (M2 student, MESA+, University of Twente, The Netherlands).

The magnets used here were free-standing fragments of Ta/NdFeB/Ta films made by high rate triode sputtering (see annex 1). A difference in thermal expansion coefficients of the substrate and the deposited layers, together with phase transformations in the magnetic film during the annealing process, and variations in film thickness across the wafer, leads to a build up of compressive stress in the deposited trilayer. When the trilayers are deposited on Si substrates, diffusion between the Si substrate and the Ta buffer layer, during the annealing treatment, leads to the formation of holes at the substrate which can in turn lead to film peel-off (Fig. 5.1). Note that peel off can be avoided by using Si substrates which have been thermally oxidized. Peeled-off fragments were cut into smaller pieces using a scalpel blade (the scalpel blade has to be demagnetized). Then the individual pieces were magnetized out-of-plane in the 8 Tesla field of a vibrating sample magnetometre (Oxford Instruments). The remanence of the films was estimated to be about 1.4 T [Demp.'07], and their thickness varied from 5 to 10 µm.

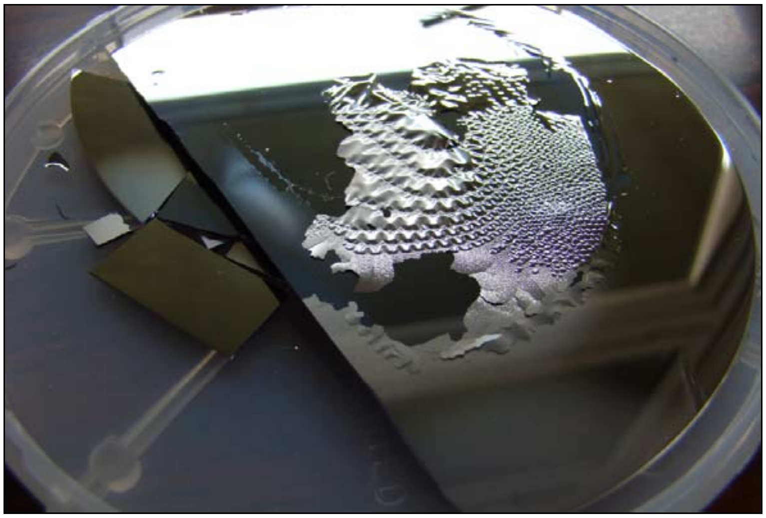

Fig. 5.1. Nd-Fe-B film partly peeled off from a 100 mm Si substrate.

The magnetized pieces were put onto an HOPG substrate, which was beforehand polished using chemical mechanical polishing. Several successful instances of levitation were recorded. Fig. 5.2 shows one selected photo of a levitating piece of a 10 µm thick film. On the photo you can see the micro-magnet and its image reflected from the surface of the HOPG substrate. The magnet was levitating almost horizontally at around 30 µm from the substrate's surface [Kok.'09].

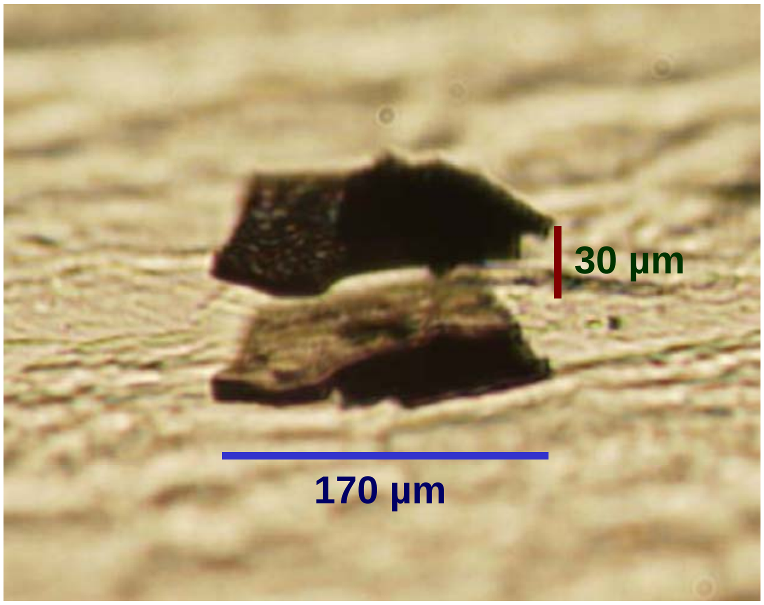

Fig. 5.2. A 10 µm thick micro-magnet levitating above HOPG.

The measured value of levitation height was compared with a calculated value. The calculation was done in the way described in the previous subsection. The magnet shape was approximated to a rectangular prism with a square base. Fig. 5.3 shows the calculated dependence of the levitation height on the magnet width. The red dot indicates the position of our levitating magnet from Fig. 5.2, assuming a 170×170 µm square. The experimental dot lies satisfyingly near the simulated curve. The slight mismatch may be explained by the incertitude in estimating the magnet size and its levitation height.

To our knowledge, this is the first experimental demonstration of levitation of a single unidirectionally magnetized magnet without external magnetic field or gradient from a supporting magnet (like e.g. Boerdijk's configuration [Boer'56/57]). Since the magnet is a single unidirectionally magnetized piece, the system is considerably less complex than proposed systems with multipolar configurations ([Perl.'92], [Prof.'08]), which is especially important if we consider that the system must be microfabricated. The absence of external field also allows the levitated magnet freedom along the substrate surface; this expands the system's potential applications for microrobotics [Kok.'09].

Note that the dimensions of the magnet are far from the optimal dimensions (450×450×200 μm) found in section 4.4.1. The optimal thickness of 200 μm is too big for Nd-Fe-B films, due to the build up of stress in such films, and the time that would be needed to fabricate such films. Since the aim of this work is to explore the potential for diamagnetic levitation in micro-systems, levitation was studied for magnets of thickness which are acceptable for micro-fabrication. Though the thickness was controlled, by the time of deposition, the planar dimensions were not well controlled. As mentioned above, efforts are on-going to prepare magnets of controlled planar shape, by the use of patterned substrates.

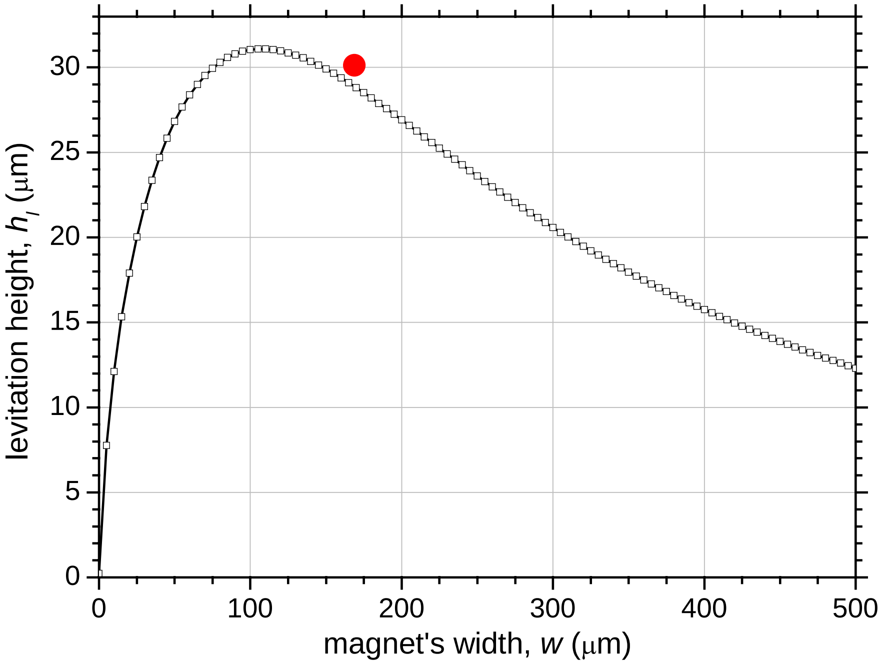

Fig. 5.3. Calculated levitation height vs. magnet width for a 10 μm thick magnet (B_r = 1.4 T) above HOPG. The red dot shows the experimentally measured position of the levitating magnet.

5.3 Towards levitation of diamagnetic objects of controlled shape

In this section we will describe preliminary experimental efforts to prepare Bi particles in controlled form, namely 1D wires and 2D sheets. To prepare the 1D structures, it was decided to electro-deposit Bi in membranes containing pores of diameter in the sub-µm range. For the 2D sheets, sputtering of Bi onto patterned Si substrates has been tried.

5.3.1 1D Bi wires by electro-deposition

The work described in this section is being done in collaboration with Laurent Cagnon and Michael Darques (Institut Néel).

Al_2O_3 nano-porous membranes with pores of diameter 50 nm were prepared by anodisation of Al sheets. Bi nano-wires of approximate length 6 µm were electro-deposited from a Bi containing salt (Bi_2O_3). The wires were released by dissolving the Al_2O_3 matrix in NaOH. The Bi nano-wire containing solution was rinsed a number of times with de-ionized water and the Bi nanowires were concentrated by centrifugation. The thus prepared nano-wires were observed in an SEM after placing a drop of the Bi nano-wire containing solution on a Si substrate and allowing it to dry. Both isolated Bi nano-wires and clusters of nanowires were observed (Fig. 5.4 (a)-(d)). In addition to the nano-wires, small particles of diameter close to 200 nm can be seen (Fig. 5.4 (a)). Imaging with the Energy Selective Back-scatter detector (ESB), which is sensitive to the atomic number of the elements being images, indicates that these small particles are not made of Bi (Fig. 5.4 (b)). Larger foreign bodies, of a few microns in size, were also observed (Fig. 5.4 (c)). The presence of these foreign bodies is attributed to recrystallization following the chemical attack used to dissolve the Al_2O_3 matrix. The use to polyamide membranes, which can be dissolved with acetone, and for which the formation of particles other than Bi is not expected, is now being tried. Membranes with pore diameters of 100 and 400 nm have been chosen.

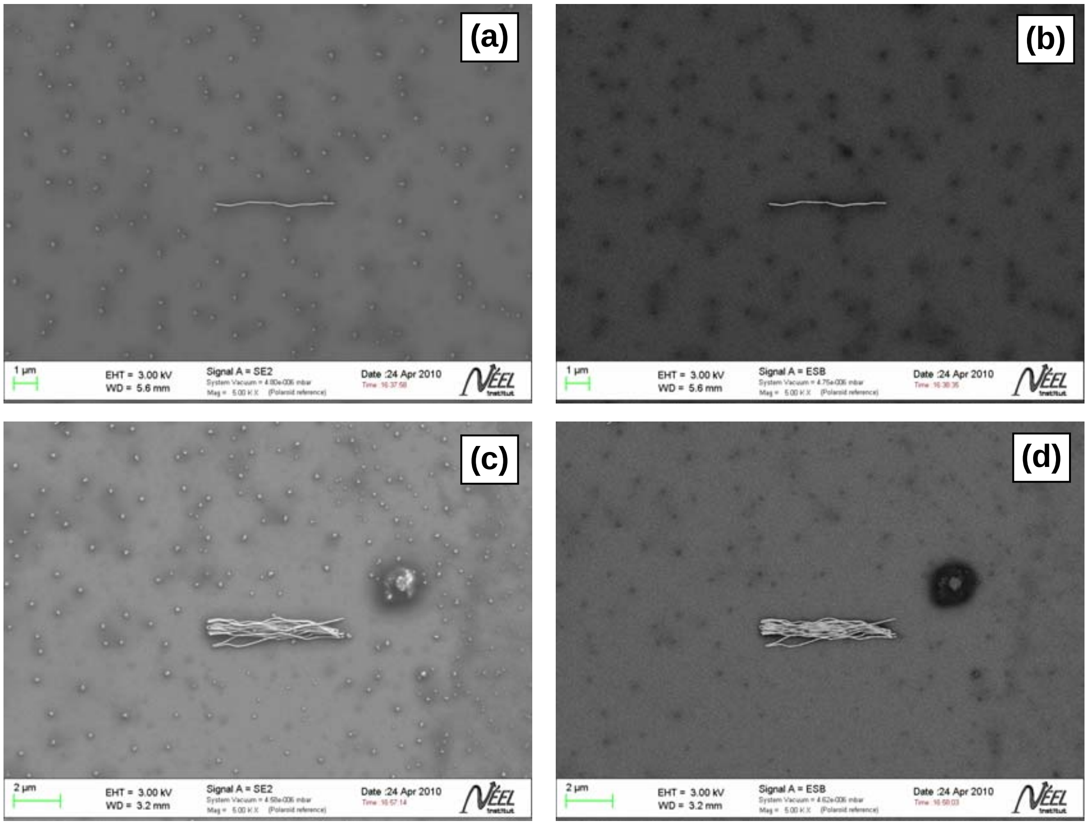

Fig. 5.4. SEM images of a residue of the Bi nano-wire containing solution, allowed to dry on a Si substrate: (a) secondary electron image of a nano-wire (diameter ≈ 50 nm, length 6 ≈µm) surrounded by equiaxed particles (diameter ≈ 200 nm); (b) back-scattered electron image showing that the equiaxed particles consist of a material having a lower atomic number than the Bi nano-wire; (c) secondary electron image of a bundle of nano-wires (diameter ≈ 50 nm, length 6 ≈µm) surrounded by equiaxed particles (diameter : 0.2-2 µm) ; (d) back-scattered electron image showing that the equiaxed particles have a lower atomic number than the Bi nano-wires.

5.3.2 2D Bi sheets by sputtering

Patterned Si substrates with stripes of depth in the range 5-20 µm and width in the range 5-100 µm were used. The substrates were prepared by deep reactive ion etching by Victor Gaude (G2Elab). Triode sputtering from a pure Bi target was carried out on both non-heated and heated substrates. The unusual form of the films (Fig. 5.5) is attributed to the low melting temperature of Bi. Thinner films deposited onto non-heated substrates are characterized by the presence of some long needle-like crystals (Fig. 5.5 (a)- (c)) while those deposited onto heated substrates are characterized by the presence of large blobs (Fig. 5.5 (d)- (f)). The formation of these blobs is attributed to a melting of the Bi during the deposition process. The thicker films deposited on non-heated substrates also show signs of melting (note spherical features in Fig. 5.5 (g)- (i)), which may be attributed to a significant heating of the substrate due to the kinetic energy of the deposited Bi atoms.

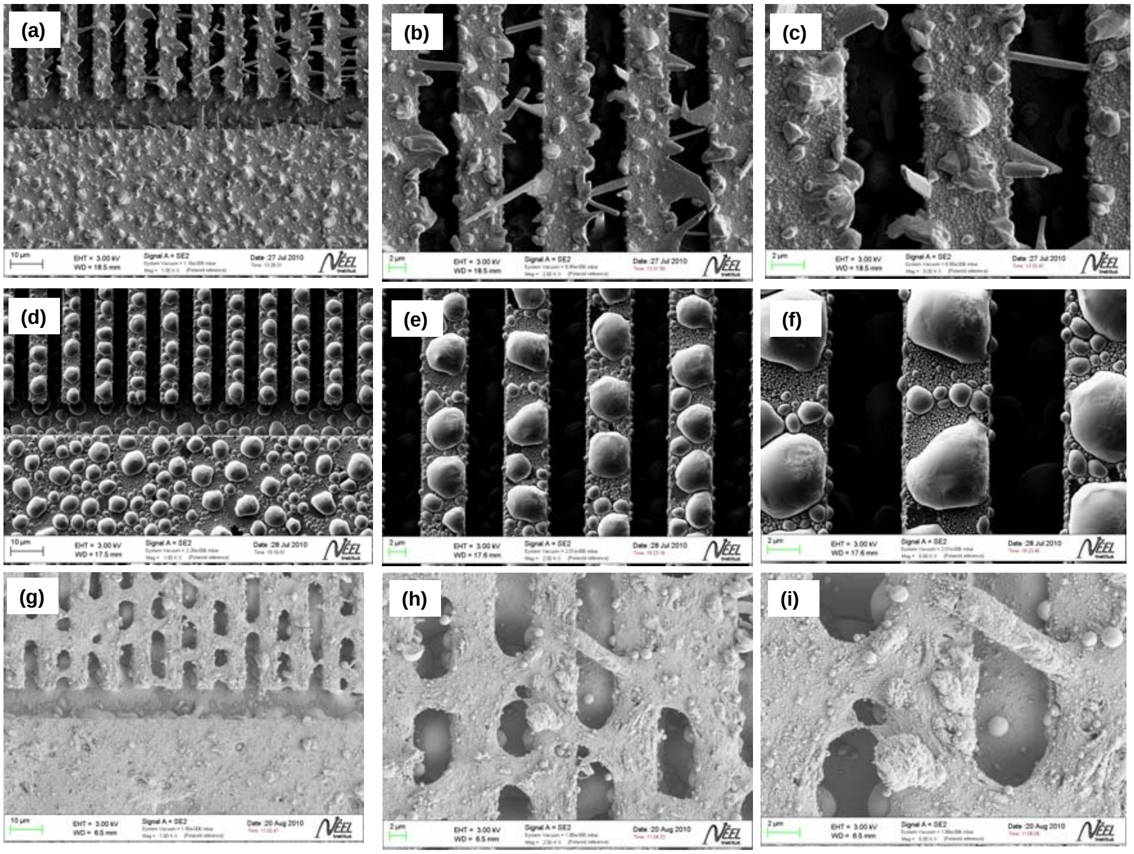

Fig. 5.5. SEM images of Bi sputter deposited onto patterned Si substrates of feature depth 5 µm. (a)-(c) films of nominal thickness 1 µm deposited on a non-heated substrate, (d)-(f) films of nominal thickness 1 µm deposited on a heated substrate (T_{sub} = 200°C), (g)-(i) films of nominal thickness 10 µm deposited on a non-heated substrate.

When films are deposited onto features with scalloped sidewalls, the form of the local Bi deposit is determined by the position on the feature (Fig. 5.6). Long needle-like crystals are formed on the top of the feature (Fig. 5.6 (a), (b)), while the side walls are characterized by two distinct populations of Bi particles, large particles at the cusp of the scallop and much finer particles between the cusps (Fig. 5.6 (c), (d)).

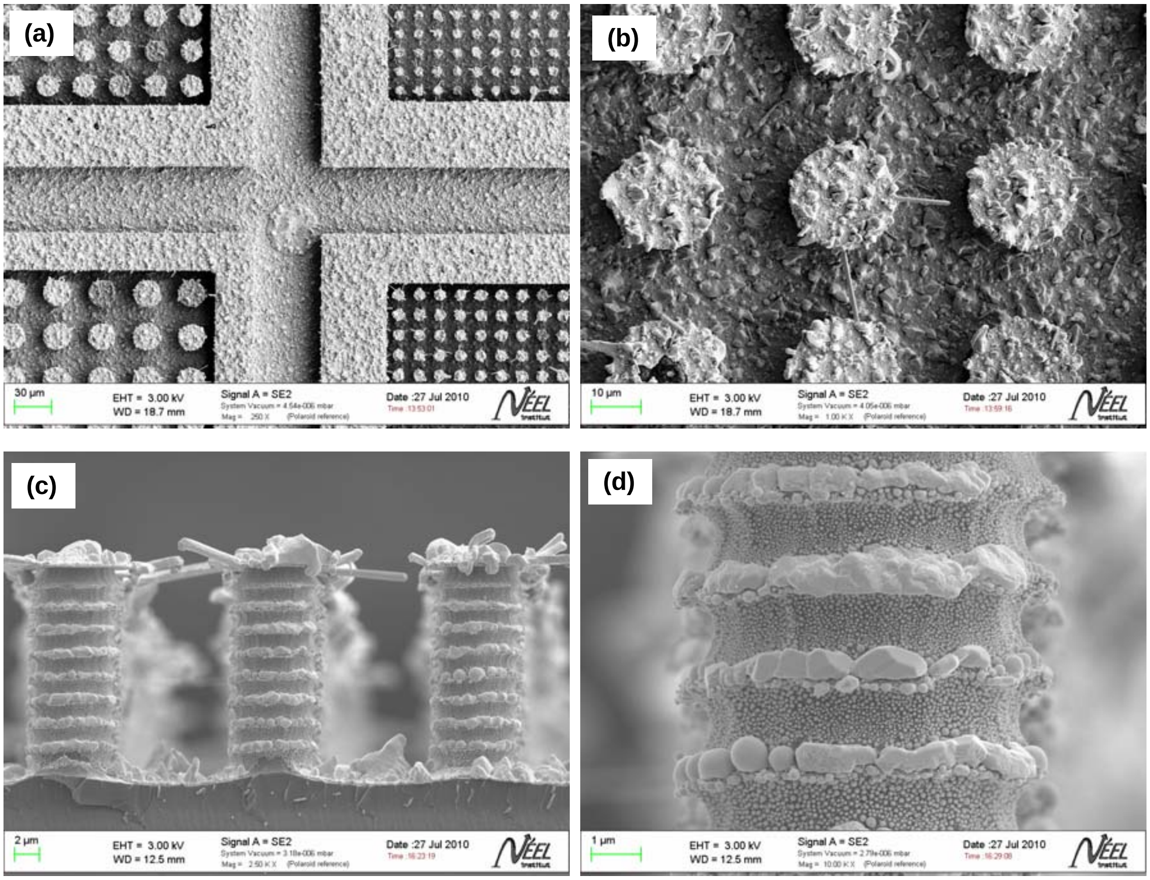

Fig. 5.6. SEM images of Bi sputter deposited (nominal thickness = 1 µm) onto non-heated patterned Si substrates of feature depth 20 µm. (a)-(b) plan-view, (c)-(d) side view.

Though the desired 2D sheet structures were not obtained using sputtering, efforts will nevertheless be made in future work to release the Bi deposits thus produced.

5.4 Conclusions and prospects

In this chapter we presented some experimental results related either directly or indirectly, to diamagnetic levitation. We showed that it is possible to levitate a uniaxially magnetized NdFeB micro-magnet above a polished substrate of HOPG. A 10 µm thick NdFeB flake levitated at a height of approximately 30 µm. The flake, of approximate surface 170×170 µm, was cut from a larger flake which had peeled off its Si substrate (the starting NdFeB film was sputter deposited).

Preliminary efforts were made to prepare Bi in controlled shapes. Electro-deposition into nano-porous Al_2O_3 membranes was used to prepare Bi wires of diameter 50 nm and length 6 µm. Deposition into polyamide membranes is now being studied, in an effort to reduce the precipitation of non-desired particles during the wire liberation step. Triode sputtering of Bi onto patterned substrates produces strangely shaped deposits. When the substrate is not heated, the deposit is characterized by the presence of some long needle-like crystals. Bi deposited onto heated substrates is characterized by the presence of large blobs, attributed to a melting of the Bi during the deposition procedure. Deposition on Bi by pulsed laser deposition will soon be assessed, as it is expected that true 2D structures will be obtainable with the technique.

Work is on-going in the lab (Luiz F. Zanini and Cuong Viet Le) to develop techniques to release deposits from their patterned substrate. In this way, micro-particles of controlled shape of any material (magnet or diamagnet) can be produced. Once structures of well-controlled shape can be made, their levitation will be studied.

GENERAL CONCLUSIONS AND PROSPECTS

Conclusions

The development and use of methods for non-invasive stray field characterization of micro-patterned high performance NdFeB hard magnetic films, destined for use in micro-systems, including levitation systems, constituted the core of this thesis work. Beyond this, modelling was used to optimise the design of levitation devices in which a diamagnetic body (HOPG), or a permanent magnet (NdFeB) is levitated. Levitation of a unidirectional magnetised NdFeB micro-magnet was experimentally demonstrated. Preliminary work was carried out on the preparation of particles of a diamagnetic material (Bi) of controlled shape and size for quantitative analysis of diamagnetic levitation.

Two experimental techniques have been used to locally measure the stray fields produced by micro-patterned hard magnetic films, scanning Hall probe microscopy and magneto-optic microscopy. In the case of scanning Hall probe microscopy, using Hall-crosses of size 4×4 μm^2 and 40×40 μm^2, protocols for the measurement of a sample's surface topography and tilt, as well as the Hall-cross to sample distance, were established. The reliable measurement of these parameters is essential for the quantitative characterisation of stray field profiles. The validity of the field profiles measured on test micro-magnet samples was supported by comparison with analytical calculations. The spatial resolution of around 15 µm was achieved (for the smallest Hall cross). A novel method for the measurement of the 3 spatial components of the stray field, using a single component probe, was proposed. The method involves making three consecutive measurements, with a rotation of the sample relative to the probe, between each measurement. The method was validated by test measurements on a mm-sized magnet.

The second technique studied concerns magneto-optic microscopy with the aid of planar and uniaxial magneto-optic indicator films (MOIF). Quantitative imaging with a planar MOIF was demonstrated for a test sample and compared to analytical calculations. A novel method, involving sequential imaging in a bias field of variable intensity, was established for quantitative imaging with the aid of a uniaxial MOIF. The method was validated by comparison of experimental data on a test micro-patterned hard magnetic film with analytical calculations.

SHPM was used for the quantitative measurement of the stray magnetic fields produced by topographically and thermomagnetically patterned NdFeB hard magnetic films. Comparison of experimentally measured field patterns with calculated ones provides important information concerning the micro-magnets' internal magnetic structure. In the case of topographically patterned films, estimation of the average value of remanent magnetization (1 T) revealed that deposition onto patterned substrates influenced the crystallographic texture achieved. In the case of thermo-magnetically patterned films, the depth of magnetization reversal was estimated to be 1.1-1.3 μm. The patterned films characterized in this study generated fields with peak-to-peak z-component induction values in the range 20-120 mT at heights of 25-30 μm above the micro-magnet arrays. At these distances the field gradient values are of the order of 10^3 T/m increasing up to 10^6 T/m at the magnet surface. A comparison of the derived z-dependence of the field and field gradient profiles reveals the relative importance of the film thickness on one hand and the magnetic structure (non-compact unipolar structure vs. fully-compact bipolar structure) on the other hand.

In a separate study, semi-analytical calculations were used to model 2 distinct plate-like levitating systems, one involving a flying diamagnet, the other a flying magnet. We have show that, in principle, it should be possible to produce a HOPG based "flying carpet" which is stable in position either above or below an array of NdFeB hard magnets, by depositing a layer of a soft magnetic material on the outer side of the HOPG. For the case of a micro-magnet in levitation above a diamagnetic substrate, we have shown how the levitation height varies, depending on the magnet size and the magnetization configuration. For a unidirectional out-of-plane magnetized magnet (single dipole) of square surface shape, the levitation height is maximal (73.5 μm) for a magnet thickness of 200 μm and width of 450 μm. The maximum permissible load which a magnet can support has been calculated for different fly heights. It varies from 1.6 mg at 10 μm to 0.02 mg at 70 μm, for a single dipole magnet.

The last part of the work concerns experimental results related either directly or indirectly, to diamagnetic levitation. We showed that it is possible to levitate a unidirectionally magnetized NdFeB micro-magnet above a polished substrate of HOPG. A 10 µm thick NdFeB flake levitated at a height of approximately 30 µm. The flake, of approximate surface 170×170 µm^2, was cut from a larger flake which had peeled off its Si substrate (the starting NdFeB film was sputter deposited). Preliminary efforts were made to prepare Bi in controlled shape by electro-deposition into nano-porous Al_2O_3 membranes and sputtering onto patterned Si substrates. While the former gave the expected geometry (nanowires of diameter 50 nm and length 6 µm), the latter technique produced films which are far from the expected 2D sheet like structure. The study of Bi growth is on-going.

Prospects

The quantitative characterization of the stray magnetic fields produced by topographically and thermomagnetically patterned hard magnetic films will remain invaluable for understanding and thus improving the processing of high performance micro-magnets. It will also contribute to the design of systems incorporating such micro-magnets. Since the used techniques are non-invasive, they could be used for quality control of partially or fully processed wafers in micro-system labs.

In future work we aim to improve the spatial resolution of SHPM, by using finer Hall-crosses and by decreasing the Hall-cross to sample distance (this will be achieved by reducing the in-plane distance between the Hall-cross and the edge of the overall probe). The spatial resolution of the MO imaging with the aid of MOIF can also be improved by using thinner MOIF, depositing a MO active layer directly onto the studied sample, and using novel types of optical microscopes and image processing techniques.

The micro-magnets which have been characterized here, are now being assessed for lab-on-chip type applications. More specifically, they are being used for the trapping of biological species (cells, bateria, liposomes, neurons...) functionalized with superparamagnetic nanoparticles (on-going thesis work of L. Zanini and collaboration with M. Frenea-Robin and N. Haddour of Laboratoire Ampere, F. Berger of Grenoble Institute of Neurosciences and C. Villard of Institut Néel). They are also being used for the repulsion of diamagnetic cells (recent thesis work of P. Kauffmann and collaboration with V. Hauget of Biopuce and F. Bruckert of LMGP). The measured field profiles and deduced field gradient profiles of the micro-magnets can be used in the quantitative analysis of the attractive / repulsive forces at play.

Work is on-going to produce micro-particles (diamagnetic particles as well as hard magnetic particles) of controlled shape and size using micro-fabrication techniques (L. Zanini and Viet Le Cuong) (lithography, lift-off, etc…). Such structures will be used as model samples to study diamagnetic levitation of objects of well-controlled shape.

Annex I: Preparation of micro-structured hard magnet films

NdFeB films were deposited by high rate triode sputtering[1] onto thermally oxidized Si substrates. The films were deposited at a substrate temperature of 450°C, and subsequently annealed at 750°C for 10 minutes, so as to induce an out-of-plane texture [Demp.'07]. 100 nm Ta layers were deposited as buffer and capping layers to prevent diffusion into the substrate and oxidation of the hard magnetic layer. The films were patterned at the micron scale using either topographic or thermo-magnetic patterning[2] (Fig. I.1).

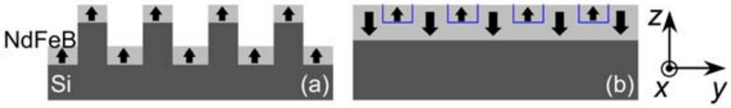

Fig. I.1. Schematic side-view representation of (a) topographically and (b) thermo-magnetically patterned films.

The latter technique exploits the fact that when we heat a hard magnetic film we reduce its coercivity. A magnetized film (typically 5 µm thick) is locally heated by laser irradiation through a mask, in the presence of an external magnetic field which is weaker than the film's room temperature value of coercivity. Only those sections of the film which are heated are remagnetized in the direction of the applied field. More details of the technique can be found elsewhere [Dum.'10].

In the case of topographic patterning, 10-40 µm thick films were deposited and annealed on Si substrates structured using deep-reactive ion etching (DRIE)[3], and then unidirectionally magnetized out-of-plane.

Both the topographically and thermomagnetically patterned films had coercivity values of about 1400 kA/m.

---

[1] The deposition was made by Nora M. Dempsey and Daniel O'Brien (Institut Néel)

[2] The thermo-magnetic patterning was performed by Frédéric Dumas-Bouchiat and Luiz F. Zanini (Institut Néel)

[3] The DRIE was performed at the PTA/MINATEC by Victor Gaude and Paul Kauffmann (G2Elab)

ANNEX II: STRAIGHTFORWARD FIELD CALCULATIONS FOR BASIC PERMANENT MAGNET CONFIGURATIONS

Annex II: Straightforward field calculations for basic permanent magnet configurations

The work described in this annex was done in collaboration with Prof. Rostislav Grechishkin (Lab. of Magnetoelectronics, Tver State University, Russia).

In this annex we give some examples using the models of Amperian currents (which was introduced in section 2.2) and of charged surfaces to calculate the stray magnetic field generated by basic configurations of permanent magnets.

In most modern textbooks on electricity and magnetism (see e.g. [Feynman '64]) the current-current forces, conduction or Amperian, are taken as fundamental, thus giving the subject a unity not attained by the older magnetic pole concept. However, as was pointed out by Brown [Brown '62], this unity is an illusion in several respects, one of which is that the interpretation of an electron spin moment as an Amperian current has no surer basis than its interpretation as a pair of poles. Although it has been criticized from a pedagogical point of view [Warb.'34], the use of magnetic poles in analogy to electrostatics is firmly established in research articles and books on ferromagnetism. The problem of reconciling of the two interpretations has been discussed in detail [Brown '62]. In the following both approaches are considered to be of equal standing and their application will be demonstrated in parallel.

II.1 Basic relations

In addition to the relations given in section 2.2 for the Amperian current model, equivalent formulas for the model of charged surfaces will be given here.

Defining the magnetic pole strength (magnetic charge) m_i (in Webers) from the Coulomb law:

$$\mathbf{F} = \frac{m_1 m_2}{4\pi\mu_0 R^3}\mathbf{R}, \tag{II.1}$$

the magnetic field strength due to magnetic charges uniformly distributed over a surface element dS will be written as:

$$d\mathbf{H} = \frac{\sigma\, dS}{4\pi\mu_0} \frac{\mathbf{R}}{R^3}, \tag{II.2}$$

where σ is the surface charge density given by the dot product:

$$\sigma = \mu_0 \left(\mathbf{M}_1 - \mathbf{M}_2\right) \cdot \mathbf{n}. \tag{II.3}$$

II.2 Axisymmetrical bodies

II.2.1 Circular turn and thin walled solenoid

The magnetic field of a circular turn has been considered in detail by Erlichson [Erl.'89] and for the sake of completeness will be outlined here. Fig. II.1 shows the geometry of the problem. From symmetry, the B_y component at the point of observation $P(x_0, y_0, z_0)$ has to be zero, so the problem reduces to the determination of B_x and B_z.

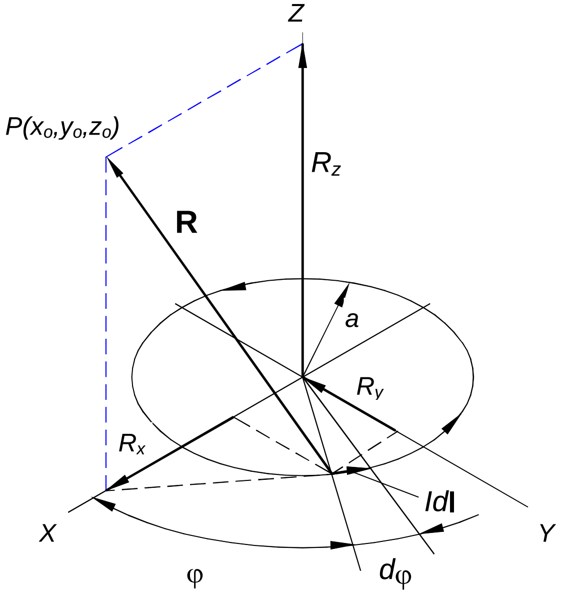

Fig. II.1. Diagram for the circular turn. *Id*l is the linear current element.

Applying the Biot-Savart law (2.2.1), noticing that the radius vector can be expressed by:

$$R^2 = z_0^2 + x_0^2 + a^2 - 2ax_0 \cos\varphi ,$$

and choosing appropriate expressions for $d\mathbf{l}$ and $\mathbf{R}$ projections we find:

$$B_x = \frac{\mu_0 I}{4\pi}\int_0^{2\pi}\frac{dl_y R_z - dl_z R_y}{R^3} = \frac{\mu_0 I}{4\pi}\int_0^{2\pi}\frac{a z_0 \cos\varphi d\varphi}{\left(z_0^2 + x_0^2 + a^2 - 2a x_0 \cos\varphi\right)^{3/2}}, \quad \text{(II.4)}$$

$$B_z = \frac{\mu_o I}{4\pi}\int_0^{2\pi}\frac{dl_x R_y - dl_y R_x}{R^3} = \frac{\mu_o I}{4\pi}\int_0^{2\pi}\frac{a(a - x_o \cos\varphi)d\varphi}{\left[z_o^2 + x_o^2 + a^2 - 2a x_o \cos\varphi\right]^{3/2}}, \quad \text{(II.5)}$$

which apart from some difference in notation coincide with the results of Erlichson.

In proceeding further to the case of a thin-walled solenoid (II.4) and (II.5) should be integrated over the solenoid length 2*h*. Taking into account that the current of an elementary ring of a height *dz* is *Idz/*2*h* one obtains:

$$B_x = \frac{\mu_0}{4\pi}\frac{I}{2h}\int_{-h}^{h}\int_0^{2\pi}\frac{a(z_0 - z)\cos\varphi d\varphi dz}{\left[(z_0 - z)^2 + x_0^2 + a^2 - 2a x_0 \cos\varphi\right]^{3/2}}, \quad \text{(II.6)}$$

$$B_z = \frac{\mu_o}{4\pi}\frac{I}{2h}\int_{-h}^{h}\int_0^{2\pi}\frac{a(a - x_o \cos\varphi)d\varphi dz}{\left[(z_o - z)^2 + x_o^2 + a^2 - 2a x_o \cos\varphi\right]^{3/2}}. \quad \text{(II.7)}$$

Making use of a subsidiary variable $u = z_0 - z$ $(du = -dz)$ one finds that the integrands in u are of the form $uU^{-3/2}$ and $U^{-3/2}$, where $U = Au^2 + Bu + C$ (A, B, C constants). The corresponding integrals are expressed in terms of elementary functions (see any standard handbook on integrals, e.g. [Dwight '61]). With this provision (II.6) and (II.7) reduce to:

$$B_x = \frac{2\mu_o a}{4\pi}\frac{I}{2h}\int_o^{\pi}\left\{\frac{\cos\varphi d\varphi}{\left[(z_o - z)^2 + x_o^2 + a^2 - 2a x_o \cos\varphi\right]^{1/2}}\right\}_{z=-h}^{z=h}, \quad \text{(II.8)}$$

$$B_z = \frac{2\mu_o a}{4\pi}\frac{I}{2h}\int_o^{\pi}\left\{\frac{(z_o - z)(a - x_o \cos\varphi)d\varphi}{\left[(z_o - z)^2 + x_o^2 + a^2 - 2a x_o \cos\varphi\right]^{1/2}}\right\}_{z=-h}^{z=h} \times$$

$$\times\left\{\frac{(z_0 - z)}{\left[(z_0 - z)^2 + x_0^2 + a^2 - 2a x_0 \cos\varphi\right]^{1/2}}\right\}_{z=-h}^{z=h} \quad \text{(II.9)}$$

Eqs. (II.8) and (II.9), as well as (II.4) and (II.5) (circular turn) could be expressed in terms of complete elliptic integrals of the first and second kind. However, following the arguments of Erlichson, we recommend here the numerical solution of these equations by any decent numerical integration routine.

II.2.2 Disk of uniform pole density

Fig. II.2 shows a diagram for the uniformly charged disk. Making use of (II.2) and taking into account that the surface element $dS = rdrd\varphi$ one arrives at integrals:

$$\mu_0 H_x = \frac{\sigma}{4\pi}\int_{r=o}^{r=a}\int_{o}^{2\pi}\frac{(x_o - r\cos\varphi)rdrd\varphi}{\left[z_o^2 + x_o^2 + r^2 - 2rx_o\cos\varphi\right]^{3/2}} =$$

$$= \frac{\sigma}{4\pi}\int_{o}^{2\pi}\left[\frac{(4C-2B^2)r-2BC}{(B^2-4C)U^{1/2}} + \ln\left|2U^{1/2}+2r+B\right|\right]_{r=o}^{r=a}\cos\varphi\, d\varphi =$$

$$= \frac{2\sigma}{4\pi}\int_{0}^{\pi}\left\{\frac{x_0(2Br+4C)-\cos\varphi\left[(4C-2B^2)r-2BC\right]}{(B^2-4C)U^{1/2}} - \right.$$

$$\left. -\cos\varphi\ln\left|2U^{1/2}+2r+B\right|\right\}_{r=0}^{r=a} d\varphi, \qquad \text{(II.10)}$$

$$\mu_0 H_Z = \frac{\sigma}{4\pi}\int_{r=o}^{r=a}\int_{o}^{2\pi}\frac{z_0 rdrd\varphi}{\left[z_o^2 + x_o^2 + r^2 - 2rx_o\cos\varphi\right]^{3/2}} = \frac{\sigma\, z_o}{4\pi}\int_{o}^{2\pi}\left[\frac{2Br+4C}{(B^2-4C)U^{1/2}}\right]_{r=o}^{r=a} d\varphi,$$

(II.11)

where $B = -2x_0\cos\varphi$, $C = x_0^2 + z_0^2$, and $U = r^2+Br+C$.

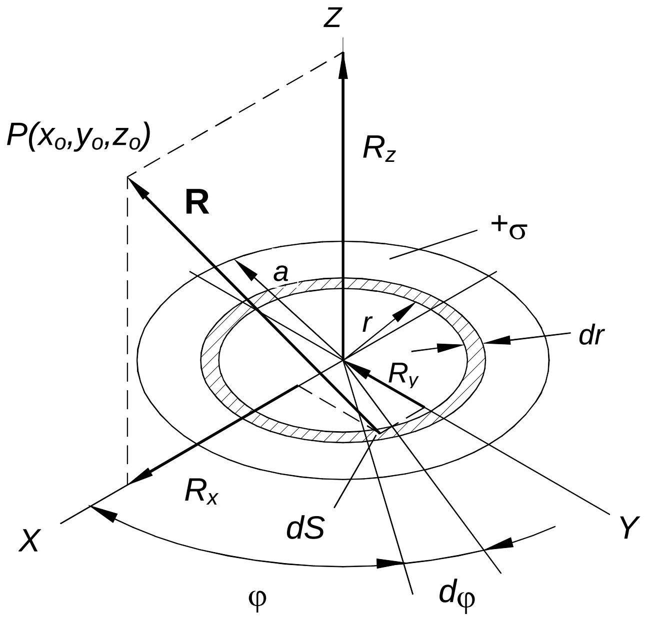

Fig. II.2. Diagram for the uniformly charged disk. $dS=rdrd\varphi$ is a surface element.

As above in this case it was possible to express external integrals over r in (II.10) and (II.11) in terms of elementary functions while the resulting expressions should be integrated numerically.

It is worthwhile to mention that Eqs. (II.10) and (II.11) derived for a single charged disk have meaning only as a one module of a sum over all positively and negatively charged surfaces constituting the real sample.

II.2.3 Axially magnetized cylinders and rings

Eqs. (II.8) and (II.9) (thin-walled solenoid) as well as (II.10) and (II.11) (charged disk) provide the basis for calculations of B_x and B_y field components of axially magnetized axisymmetrical bodies at any observation point.

As to the current model, (II.8) and (II.9) may be immediately used for permanent magnet field calculations when the coefficient $\mu_0 I/2h$ outside the integral sign is replaced by B_r, permanent magnet remanence.

For the equivalent charge model (Eqs. (II.10) and (II.11)) the axially magnetized cylinder should be represented by a pair of oppositely charged disks at a distance $2h$ apart from each other with their fields being superimposed for each point of observation. In doing so the coefficient σ should be replaced by B_r.

In Fig. II.3 (a) and (b) the current and charge presentation is sketched for axially magnetized cylinders and rings. For the former case the ring is represented by two superimposed oppositely magnetized cylinders of equal height and diameters equal to the outer and inner ring diameter, respectively. For the charge model the solution is obtained just by substitution of $r = a_1$ (inner ring radius) for the lower limit of integration in Eqs. (II.10) and (II.11), while the upper limit $r = a_2$ should be standing for the outer ring radius.

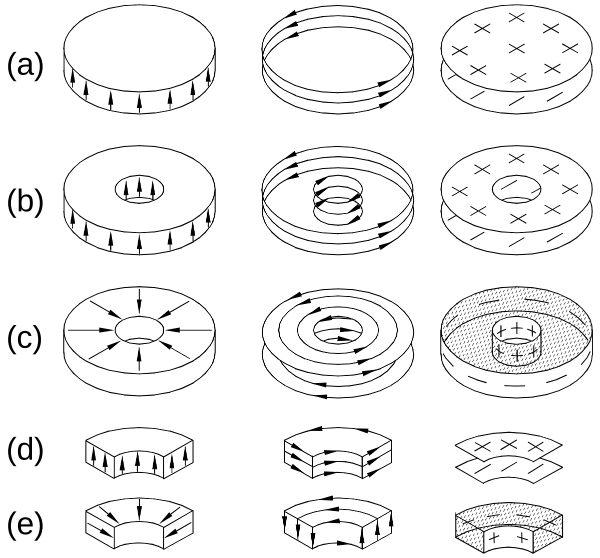

Fig. II.3. Presentation of axisymmetrical magnets (left column) by Amperian currents (middle column) and surface charges (right column). (a) - axially magnetized disk, (b) - axially magnetized ring, (c) - radially magnetized ring, (d), (e) - axially and radially magnetized ring segments, respectively. Hatching indicates the existence of volume charges in two specific cases of radial magnetization.

II.2.4 Radially magnetized rings

The presentation of a ring with radial magnetization frequently used in microwave devices is illustrated in Fig. II.3 (c) for both models.

In the current model such a ring is represented by two flat spiral solenoids. The calculation is much the same as above with the difference that now the integration of the field of a current ring is performed in the radial direction.

For example, the B_z component of a single flat spiral solenoid will be given by:

$$B_z = \frac{\mu_o}{4\pi}\frac{I}{a_2 - a_1}\int_{a_1}^{a_2} da \int_0^{2\pi} \frac{a\left(a - x_o \cos\varphi\right)d\varphi}{\left[a^2 - 2ax\cos\varphi + x_o + z_o^2\right]^{3/2}} =$$

$$= \frac{\mu_o}{4\pi}\frac{I}{a_2 - a_1}\times$$

$$\int_o^{2\pi}\left\{\frac{a}{a^2 - 2ax_o\cos\varphi + x_o^2 + z_o^2} + \ln\left|a - x_o\cos\varphi + \sqrt{a^2 - 2ax_o\cos\varphi + x_o^2 + z_o^2}\right|\right\}_{a=a_1}^{a=a_2} d\varphi\,,$$

(II.12)

where a_1 and a_2 stand for the inner and outer spiral radius, respectively. To obtain the total field of the ring (II.12) should be used twice for two flat spirals at a distance $2h$ apart. In doing so the change of the current direction for the two solenoids should be accounted for as illustrated in Fig. II.3 (c).

To obtain the similar result by the charge model it is necessary to take into account *volume* charges arising inside the ring, because for this specific case the uniformity of magnetization is violated due to its radial character. Evidently this requires additional calculating efforts not encountered in the current model and so will not be considered here.

In addition to the cases considered above, Fig. II.3 (d) and (e) illustrate the presentation of ring segments, magnetized axially or radially, by both models. Such segments are widely used in modern brushless motors. It is seen that their field may be calculated equally well by the methods described provided appropriate limits of integration corresponding to the radial and angular segment dimensions are used and the contribution of the lateral cross-sectional segment sides is taken into account.

II.3 Tetragonal prisms

II.3.1 Rectangular sheet of uniform pole density

Formulas for a rectangular current turn and a thin solenoid are given in section 2.2.2. Here we give the formulas for the field generated by a rectangular sheet having a uniform current density.

According to the Coulomb law (II.1) the magnetic field strength of a surface element $dS = dxdy$ (Fig. II.4) is:

$$\mu_0 d\mathbf{H} = \frac{\sigma}{4\pi} dxdy \frac{\mathbf{R}}{R^3} .$$

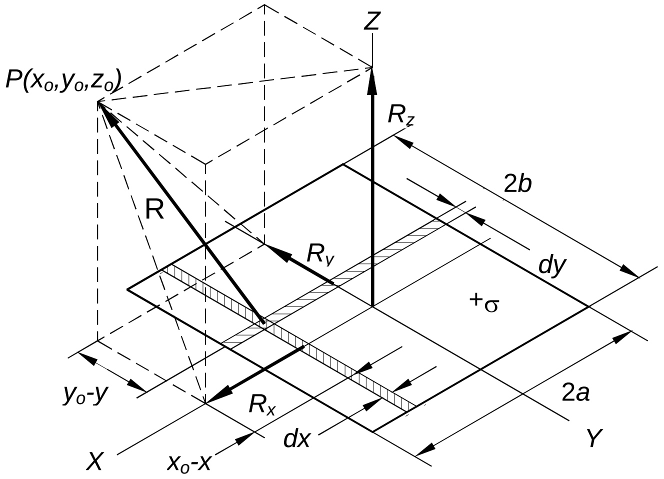

Fig. II.4. Diagram for the rectangular sheet of uniform pole density +σ.

Integration over the sides of the sheet from -*a* to *a* and -*b* to *b* yields:

$$\mu_0 H_x = \frac{\sigma}{4\pi}\left\{\left[\ln\left(\beta + \sqrt{\alpha^2 + \beta^2 + (z_o - z)^2}\right)\right]_{\alpha_1}^{\alpha_2}\right\}_{\beta_1}^{\beta_2}, \tag{II.13}$$

$$\mu_0 H_y = \frac{\sigma}{4\pi}\left\{\left[\ln\left(\alpha + \sqrt{\alpha^2 + \beta^2 + (z_o - z)^2}\right)\right]_{\alpha_1}^{\alpha_2}\right\}_{\beta_1}^{\beta_2}, \tag{II.14}$$

$$\mu_0 H_z = \frac{\sigma}{4\pi}\left\{\left[\arctan\frac{\alpha\beta}{\gamma\sqrt{\alpha^2 + \beta^2 + (z_o - z)^2}}\right]_{\alpha_1}^{\alpha_2}\right\}_{\beta_1}^{\beta_2}, \tag{II.15}$$

where $\alpha_{1,2} = x_0 \pm a, \beta_{1,2} = y_0 \pm b$ (+ and - signs apply to subscripts 1 and 2, respectively).

II.3.2 Tetragonal prismatic magnet: axial and inclined magnetization

A scheme representing the axially magnetized tetragonal prisms by charges is given in Fig. II.5 (a scheme representing the same prism by currents is given in Fig. 2.2 (a) in chapter 2).

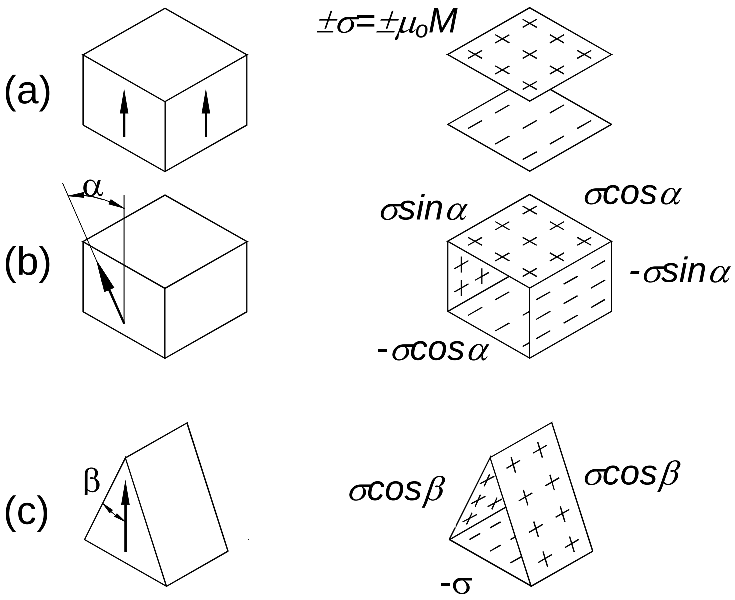

Fig. II.5. Representation of prismatic magnets (left column) by surface charges (right column).

The interpretation is similar to cylinders shown in Fig. II.3 (a). In the charge model a superposition of the field from two distant oppositely charged sheets should be performed by replacing surface charge density σ by B_r in formulas (II.13) - (II.15). With this provision (II.13) and (II.14) ($\mu_0 H_x$ and $\mu_0 H_y$) get exactly the same form as (2.2.6) and (2.2.7) (current model, given in section 2.2.3), while $\mu_0 H_z$ is expressed as:

$$\mu_0 H_z = \frac{B_r}{4\pi}\left\{\left[\left(\arctan\frac{\alpha\beta}{\gamma\sqrt{\alpha^2+\beta^2+\gamma^2}}\right)_{\alpha_1}^{\alpha_2}\right]_{\beta_1}^{\beta_2}\right\}_{\gamma_1}^{\gamma_2}. \qquad \text{(II.16)}$$

The expression in the curly brackets is a function f of α, β and γ which obeys the following relation:

$$\left\{\left[\left(f(\alpha,\beta,\gamma)\right)_{\alpha_1}^{\alpha_2}\right]_{\beta_1}^{\beta_2}\right\}_{\gamma_1}^{\gamma_2} = f(\alpha_2\beta_2\gamma_2) - f(\alpha_1\beta_2\gamma_2) - f(\alpha_2\beta_1\gamma_2)$$
$$+ f(\alpha_1\beta_1\gamma_2) - f(\alpha_2\beta_2\gamma_1) + f(\alpha_1\beta_2\gamma_1) + f(\alpha_2\beta_1\gamma_1) - f(\alpha_1\beta_1\gamma_1),$$

where $\alpha_{1,2} = x \pm a, \beta_{1,2} = y_o \pm b, z_{1,2} = z \pm h$ (+ and - signs apply to subscripts 1 and 2, respectively).

For a case of **M** rotated by an angle φ in the *ZY* plane (Fig. II.5 (b)), four charged sheets should be used. In the general case of φ arbitrary (not shown in the figure) six charged sheets (or three superimposed solenoids) are needed.

Still another application of the models to triangular prisms is depicted in Fig. II.5 (c). Such triangular prisms are effective as building blocks in some modern permanent magnet systems [Leup.'92, Abele '90, Blaz.'85].

Fig. II.6 shows how the magnetization orientation in two adjacent rectangular blocks affects the total B_z field at some distance above the magnets. It is seen that B_z passes through a maximum with the change of abs(φ) from zero to $\pi/2$. A three-fold increase in the peak value of B_z is observed when $\varphi \cong 70^o$ thus demonstrating the performance improvement obtainable in the so-called convergent magnet structure [Blaz.'85].

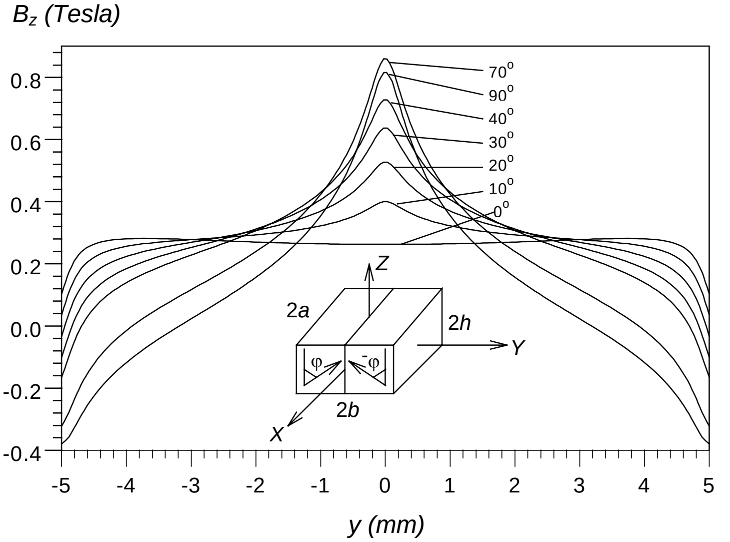

Fig. II.6. Variation of the B_z field near the upper surface (δ = 0.2 mm) of a convergent magnet structure as dependent on the orientation of magnetization in adjacent blocks. For φ=0 the system behaves like a single magnet, otherwise a maximum in B_z occurs. $2a$ = 15, $2b$ = 10, $2h$ = 5 mm, B_r = 0.9 T.

II.4 Remarks and discussion

The above given derivations show that both current and charge models may be in principle equally well employed to the description of various permanent magnet configurations. Some advantages may be found in a particular model from the mathematical point of view or when keeping up the tradition is desirable. For example, the current model requires simpler mathematics when axisymmetrical bodies are considered. On the other hand we find the charge model more convenient in the analysis of complex polygonal shapes.

Juxtaposing the two models provides a very instructive insight into the problem of external and internal field of magnetized bodies. To illustrate this important matter in Fig. II.7 we present the B_z and $\mu_0 H_z$ distributions for a cubic sample (magnetized along the Z-direction) as obtained by two methods [Eqs. (2.2.8) and (II.16)]:

$$B_z = -\frac{\mu_o}{4\pi}\frac{I}{2h}\left\{\left[\left(\arctan\frac{\gamma\sqrt{\alpha^2+\beta^2+\gamma^2}}{\alpha\beta}\right)_{\alpha_1}^{\alpha_2}\right]_{\beta_1}^{\beta_2}\right\}_{\gamma_1}^{\gamma_2},$$

$$\mu_0 H_z = \frac{B_r}{4\pi}\left\{\left[\left(\arctan\frac{\alpha\beta}{\gamma\sqrt{\alpha^2+\beta^2+\gamma^2}}\right)_{\alpha_1}^{\alpha_2}\right]_{\beta_1}^{\beta_2}\right\}_{\gamma_1}^{\gamma_2}.$$

Note that the current model gives the **B** value everywhere, while the charge model gives the subsidiary vector quantity μ_o**H**, which is equal to **B** outside the sample and differs exactly by the value of μ_0**M** inside the sample, in full accordance with basic relation **B** = μ_0(**H** + **M**) [Purcell ’86]. At the same time $\mu_o H_x$ and $\mu_o H_y$ are equal to B_x and B_y correspondingly because for this particular case $\mu_0 M_x = \mu_0 M_y = 0$. These arguments explain why the formulas for B_x ($\mu_o H_x$) and B_y ($\mu_o H_y$) are the same when different models are applied to tetragonal prisms. In contrast, similar pair of formulas (II.8) and (II.10) (cylinders) are of markedly different appearance. We were not able to bring them into the same form analytically. However, the numerical check confirmed their full consistency with the above deduction within the error of integration.

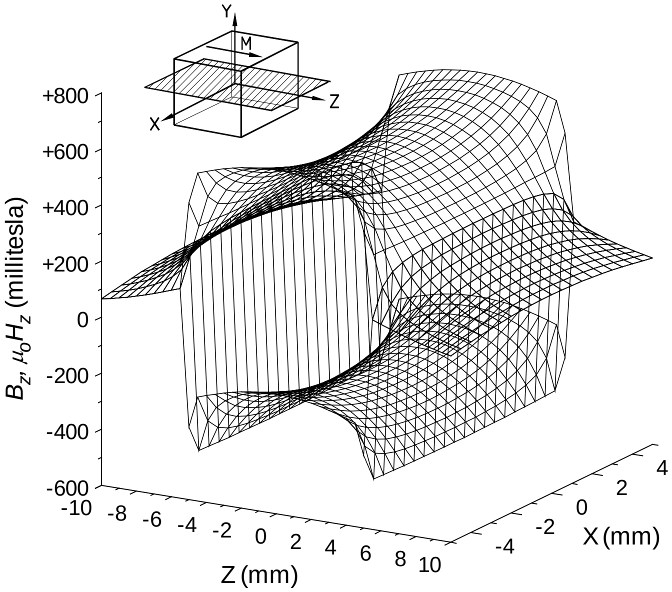

Fig. II.7. Magnetic induction B_z and field intensity μ_0H_z in the central *XZ* plane for a 10×10×10 mm *Z*-magnetized cube as calculated by equivalent current (upper graph) and charge (lower graph) formalisms. The values are the same outside the body and differ exactly by $\mu_0M_z=B_r=0.8$ T ($M_x=M_y=0$) inside it. Dashed surface in the inset indicates the observation plane.

The inside $\mu_0\mathbf{H}$ derived by any model (to obtain $\mu_0\mathbf{H}$ inside the sample by the current model just subtract $\mu_0\mathbf{M}$ from $\mathbf{B}$) is in fact the so-called self-demagnetizing field. It is worthwhile to recall that in non-ellipsoidal bodies the demagnetizing field is not uniform [Past.'94, Joseph '65]. This fact is generally accounted for by introducing a ballistic (averaged over the central cross-section) and magnetometric (averaged over the whole sample volume) demagnetizing factors [Joseph '65]. These may be computed provided $\mu_0\mathbf{H}$ is characterized locally inside the sample. In this way we were able to reproduce exactly the known tables of demagnetizing factors for cylinders and rectangular prisms derived otherwise in a more complex fashion. Evidently other magnet shapes may be characterized in the same way.

Still another application of the results presented is connected to the calculation of both external and internal fields arising from magnetic domains. To this end we may think of a magnetic domain as a permanent magnet. This is justified because generally the domain wall thickness is small compared to the domain size. With this provision the above derivations may be directly applied to a variety of magnetic domain structures. An illustration of this approach to the analysis of some typical domain structures is given in Fig. II.8.

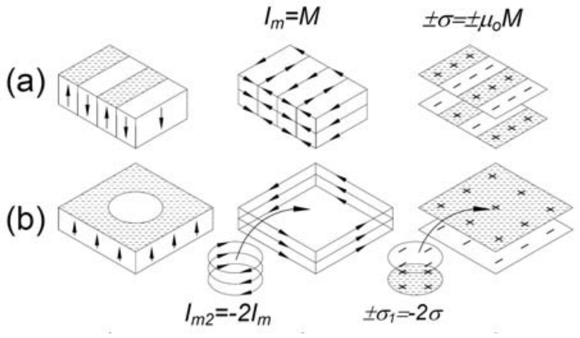

Fig. II.8. Presentation of some typical domain structures (DS) by Amperian currents and magnetic charges. (a) Kittel-type stripe 180° DS , (b) cylindrical (bubble) DS.

In conclusion of the annex, we have demonstrated that straightforward calculations of a variety of permanent magnet configurations are feasible from the first principles given by the fundamental laws supported by simple numerical techniques. The calculation details presented here have not been previously available in a single paper or textbook.

The derived general formulas are summed below for particular cases of the B_z field component on the magnet Z-axis, as a function of coordinate z_0, when the solutions are greatly simplified. Part of these formulas may be found in standard textbooks on electromagnetism. However, here they arrive from the simplification of corresponding general equations rather than from direct elementary derivation.

Circular turn of radius *a*:

$$B_z^{x=y=0}(z_0)=\frac{\mu_0 I}{2}\frac{a^2}{\left(a^2+z_0^2\right)^{3/2}}.$$

Charged disk of radius *a*:

$$\mu_0 H_z^{x=y=0}(z_0)=\frac{\sigma}{2}\left(1-\frac{z_o}{\left(a^2+z_0^2\right)^{1/2}}\right).$$

Axially magnetized cylinder of height 2h:

$$B_z^{x=y=0}(z_0)=\frac{B_r}{2}\left\{\frac{\gamma}{\left(a^2+\gamma^2\right)^{1/2}}\right\}_{\gamma_1=z_0+h}^{\gamma_2=z_0-h}.$$

Axially magnetized ring:

$$B_z^{x=y=0}(z_0)=\frac{B_r}{2}\left\{\left[\frac{\gamma}{\left(a^2+\gamma^2\right)^{1/2}}\right]_{a_1}^{a_2}\right\}_{\gamma_1=z_0+h}^{\gamma_2=z_0-h}.$$

where a_1 = inner, a_2 = outer ring radius.

Flat spiral solenoid:

$$B_z^{x=y=0}(z_0)=\frac{\mu_0}{2}\frac{NI}{a_2-a_1}\left[-\frac{a}{\left(a^2+\gamma^2\right)^{1/2}}+\ln\left(a+\sqrt{a^2+\gamma^2}\right)\right]_{a_1}^{a_2},$$

where N = number of turns.

Radially magnetized ring:

$$B_z^{x=y=0}(z_0)=\frac{B_r}{2}\left[\left(\frac{1}{\xi_1}-\frac{1}{\xi_2}\right)-\left(\frac{1}{\zeta_1}-\frac{1}{\zeta_2}\right)+\ln\left|\frac{(1+\zeta_1)(1+\xi_2)}{(1+\zeta_2)(1+\xi_1)}\right|\right],$$

$$\xi_{1,2} = \frac{\left[a_1^2 + (h \mp z_0)^2\right]^{1/2}}{a_1}, \ \zeta_{1,2} = \frac{\left[a_2^2 + (h \mp z_0)^2\right]^{1/2}}{a_2},$$

where - and + signs apply to subscripts 1 and 2, respectively.

Rectangular current turn $2a \times 2b$:

$$B_z^{x=y=0}(z_0) = \frac{\mu_0 I}{\pi} \frac{ab}{\left(a^2 + b^2 + z_0^2\right)^{1/2}} \left(\frac{1}{b^2 + z_0^2} + \frac{1}{a^2 + z_0^2} \right).$$

Rectangular charged sheet $2a \times 2b$:

$$\mu_0 H_z^{x=y=0}(z_0) = \frac{\sigma}{\pi} \arctan \frac{ab}{z_0 \sqrt{a^2 + b^2 + z_0^2}} \ .$$

Tetragonal prism $2a \times 2b \times 2h$:

$$B_z^{x=y=0}(z_0) = -\frac{B_r}{\pi} \left[\arctan \frac{\gamma \sqrt{a^2 + b^2 + \gamma^2}}{ab} \right]_{\gamma_1 = z_0 + h}^{\gamma_2 = z_0 - h},$$

$$\mu_0 H_z^{x=y=0}(z_0) = \frac{B_r}{\pi} \left[\arctan \frac{ab}{\gamma \sqrt{a^2 + b^2 + \gamma^2}} \right]_{\gamma_1 = z_0 + h}^{\gamma_2 = z_0 - h}.$$

Annex III: Operation features of a lock-in amplifier

To understand specificity of the calibration procedure (section 2.3.2) due to the operation features of a lock-in amplifier let's have a look at the basic principle of the lock-in operation, which is called synchronous detection. The technique is used to detect and measure very small AC signals. A Lock-in amplifier can make accurate measurements of small signals even when the signals are obscured by noise sources which may be a thousand times larger. Essentially, a lock-in is a filter with an arbitrarily narrow bandwidth which is tuned to the frequency of the signal. Such a filter will reject most unwanted noise to allow the signal to be measured. A typical lock-in application may require a center frequency of 10 KHz and a bandwidth of 0.01 Hz. This 'filter' has a *Q* of 10^6 - well beyond the capabilities of passive electronic filters [Manual of Stanford Research Systems SR530].

The synchronous detection is based on multiplication of an input signal with a reference signal (Fig. III.1).

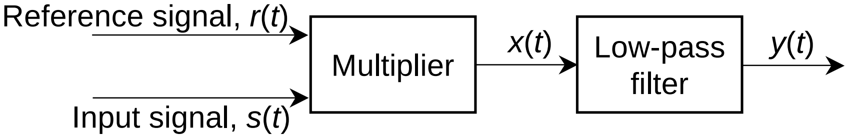

Fig. III.1. Schematic diagram of the principal of synchronous detection.

If the reference $r(t)$ and input $s(t)$ signals are both harmonic functions $r(t) = R\sin(\omega_R t)$, $s(t) = S\sin(\omega t + \varphi)$ then the output signal of the multiplier is

$$x(t) = r(t)s(t) = RS\frac{\cos((\omega - \omega_R)t + \varphi) - \cos((\omega + \omega_R)t + \varphi)}{2}. \qquad \text{(III.1)}$$

This signal then goes through a low-pass filter; the cutoff frequency of the filter ω_C is much smaller than the reference frequency ω_R. Therefore the sum frequency term does not pass the filter and the difference frequency term pass the filter only if the differential frequency $\omega - \omega_R < \omega_C$. Usually ω_C is so low that only the frequencies very close to the reference frequency can have a nonzero response at the output of the filter.

In the case when the frequency of the input signal is equal to the reference frequency (the input signals of the multiplier are synchronous – it gives the name to the method “synchronous detection”) a term with the zero difference frequency (i.e. DC component) appears at the output of the multiplier. If the filter’s transfer constant within the bandwidth is one than the output signal of the filter is

$$y_S(t) = \text{const} = \frac{1}{2} RS \cos\varphi . \tag{III.2}$$

So the output signal of a synchronous detector is proportional to the amplitude of the input signal and depends on its phase shift relatively the reference signal. If we shift the phase of the reference signal by π/2 (i.e. take it $r(t) = R\cos(\omega_R t)$) then the output signal will be

$$y_c(t) = \text{const} = \frac{1}{2} RS \sin\varphi . \tag{III.3}$$

y_s and y_c are called the in-phase and out-of-phase components of the output signal. Usually lock-in amplifiers provide both of these values (such lock-n amplifiers are called two-phase lock-in amplifiers). These values are proportional to the quadrature components of the input signal, $S\cos\varphi$ and $S\sin\varphi$ respectively, and allow calculating the amplitude and phase of the input signal:

$$S = \frac{2\sqrt{y_c^2 + y_s^2}}{R} , \tag{III.4}$$

$$tg\varphi = \frac{y_c}{y_s} . \tag{III.5}$$

In the general case when the input signal is not harmonical (but the reference signal is) and its amplitude changes with time, the in-phase and out-of-phase components of the output signal of a lock-in amplifier are:

$$y_s(t) = \frac{R}{T} \int\limits_{t-T}^{t} \sin(\omega_R \tau + \varphi) S(\tau) d\tau , \tag{III.6}$$

$$y_c(t) = \frac{R}{T} \int\limits_{t-T}^{t} \cos(\omega_R \tau + \varphi) S(\tau) d\tau . \tag{III.7}$$

Note that taking the input signal $s(t) = S\sin(\omega t + \varphi)$ and the time constant $T \to \infty$, formulas (III.6) and (III.7) give you formulas (III.2) and (III.3).

Annex IV: Estimation of the probe inclination by comparison of magnetic calibration curves

This annex concerns to the problem stated in section 2.3.4. The probe's inclination angle can be measured not only optically but also magnetically, by comparison of two calibration graphs: one for the horizontal and the other one for the inclined position of the probe. The inclination angle is given by the formula:

$$\alpha_1 = \arccos\left(\frac{c_{s1}}{c_{s0}}\right), \tag{IV.1}$$

where c_{s1} is the slope value of the calibrating line at $\alpha = \alpha_1$, and c_{s0} is the slope for the horizontal position of the probe.

Let's take up an example. If the coefficient c_{s0} is measured with a relative error $\varepsilon(c_{s0})$, the coefficient $c_{s1} = c_{s0}\cos\alpha_1$ will have the same relative error $\varepsilon(c_{s0})$. So $c_{s0} = \bar{c}_{s0} \pm \varepsilon(c_{s0})\%$, $c_{s1} = \bar{c}_{s1} \pm \varepsilon(c_{s0})\%$. We can rewrite (1) as

$$\alpha_1 = \arccos\left(\frac{\bar{c}_{s1} \pm \varepsilon(c_{s0})\%}{\bar{c}_{s0} \pm \varepsilon(c_{s0})\%}\right) = \arccos\left(\frac{\bar{c}_{s1}}{\bar{c}_{s0}} \pm 2\varepsilon(c_{s0})\%\right). \tag{IV.2}$$

Or

$$\alpha_1 = \bar{\alpha}_1 \pm \Delta\alpha_1 = \arccos\left(\frac{\bar{c}_{s1}}{\bar{c}_{s0}} \pm \frac{\bar{c}_{s1}}{\bar{c}_{s0}} \cdot 2\varepsilon(c_{s0})\right). \tag{IV.3}$$

If we note $\frac{\bar{c}_{s1}}{\bar{c}_{s0}}$ as *v*, so its absolute error $\frac{\bar{c}_{s1}}{\bar{c}_{s0}} \cdot 2\varepsilon(c_{s0})$ will be Δv.

The absolute error for α_1 will be

$$\Delta\alpha_1 = \left|\frac{\partial}{\partial v}(\arccos(v))\right|\Delta v = \left|-\frac{1}{\sqrt{1-v^2}}\right|\Delta v. \tag{IV.4}$$

The slope of the calibration line for the 40×40 μm^2 active area c_{s0} = 42.44 mV/A ± 0.35%. For the typical inclination angle 5^o: $c_{s1} = c_{s0} \cdot \cos 5° \pm 0.35\%$. In this case $v = \frac{\bar{c}_{s1}}{\bar{c}_{s0}} = \frac{\bar{c}_{s0}\cos 5°}{\bar{c}_{s0}} = \cos 5° \approx 0.99619$, $\Delta v = \frac{\bar{c}_{s1}}{\bar{c}_{s0}} \cdot 2\varepsilon(c_{s0}) \approx 0.00697$. Using (4), $\Delta\alpha_1 = 11.4737 \cdot 0.00697 \approx 0.08001$. And the relative error $\varepsilon(\alpha_1) = \frac{\Delta\alpha_1}{\alpha_1} \times 100\% \approx \frac{0.08001}{5\pi/180} \times 100\% \approx \frac{0.08001}{0.08727} \times 100\% \approx 91.6851$. It is a much higher error than we have for the optical method of measurement of inclination angle (±10%). Let's find out what the relative error of the coefficient c_{s0} must be to make $\varepsilon(\alpha_1)$=10%. For this find Δ*v* first. From (IV.4) it is

$$\Delta v = \sqrt{1 - v^2}\,\Delta\alpha_1 \approx 0.00076 .$$

Knowing that $\Delta v = \frac{\bar{c}_{s1}}{\bar{c}_{s0}} \cdot 2\varepsilon(c_{s0})$,

$$\varepsilon(c_{s0}) = \frac{\Delta v}{2}\frac{\bar{c}_{s0}}{\bar{c}_{s1}} \times 100\% = \frac{\Delta v}{2\cos\alpha_1} \times 100\% \approx \frac{0.00076}{2 \cdot 0.99619} \times 100\% \approx 0.038174\% ,$$

which means that the tilt of the tilt of the calibration line must be measured with an accuracy almost 10 times better than we have now, and this is why we used the optical method in our work.

Annex V: Coordinate system transformation and the choice of the angles

This annex concerns the measurement method for the three spatial magnetic field components, using a single component probe, which was described in section 2.3.6. The aim of this analysis was to find the angles of the Hall probe / sample orientation which are most appropriate for the two different measurement purposes described below. Matrices of coordinate system transformation corresponding to each of the two sets of optimal angles will also be given.

V.1 Coordinate system transformation

The non-orthogonal coordinate system is determined by three sensor-sample orientations (at three moments when the three measurements are taken). Each of the axes of this coordinate system in fact shows the direction of the probe's sensitivity axis at a corresponding moment when a measurement is taken. The orthogonal system is attached to the sample. In this system we need to know the three components of the magnetic field vector.

The position of the *pqr* coordinate system in the *xyz* system is determined by four angles (Fig. V.1). The angle α determines the probe tilt with respect to the Z-axis. Note that the axis of rotation is orthogonal to the XoY plane, and hence the angles between the pairs (p, z), (q, z) and (r, z) are equal. The angle β_1 is the angle between the projection of the p axis on the XoY plane and the x axis. The two angles α and β_1 are given by the initial orientation of the probe and must be measured. An optical measurement may be used, though we suppose it will give a considerable uncertainty. Scalar [Mer.'00] or vector [Ripka '01] calibration procedures may be a better option for finding the angles. Note that these angles must be measured anyway (even in the case of 1D measurements), for they determine the Hall cross – sample distance (see section 2.3.4).

The angles β_2 and β_3 are the angles between the projections of the q and r axes correspondingly and the projection of the p axis on the XoY plane. These angles are determined by the rotation of the rotary table and can be set with a very good precision (0.025° for Semprex KD-series).

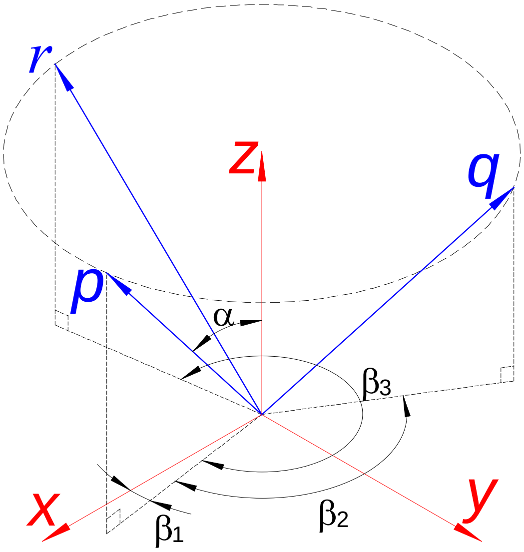

Fig. V.1. Two coordinate systems: a nonorthogonal (*pqr*) determined by the sensor–to-sample position at the moments of measurement and an orthogonal (*xyz*) linked to the sample.

As a result of the measurement procedure described before we have three components of magnetic field in the coordinate system *pqr* (B_p, B_q, B_r) As for the next step, we have to calculate the components of the vector in the *xyz* coordinate system (B_x, B_y, B_z). Let's find out the corresponding coordinate system transformation.

The dot product of the vectors $B_p\mathbf{e}_p$ and $\mathbf{B}$, where B_p is the projection of $\mathbf{B}$ on the axis *p* and $\mathbf{e}_p$ is the basis vector of this axis:

$$(B_p\mathbf{e}_p,\mathbf{B}) = B_pB\cos(\mathbf{e},\mathbf{B}) = B_pB_p\,. \tag{V.1}$$

On the other hand:

$$(B_p\mathbf{e}_p,\mathbf{B}) = B_p(e_{p_x}B_x + e_{p_y}B_y + e_{p_z}B_z)\,, \tag{V.2}$$

where e_{p_x}, e_{p_y}, e_{p_z} appear to be the direction cosines of the axis *p* in the *xyz* coordinate system:

$$e_{p_x} = \left|\mathbf{e}_p\right|\cos\gamma_{px} = \cos\gamma_{px}\,,\; e_{p_y} = \cos\gamma_{py}\,,\; e_{p_z} = \cos\gamma_{pz}\,, \tag{V.3}$$

where $\gamma_{px}, \gamma_{py}, \gamma_{pz}$ are angles between the axis *p* and the axes *x*, *y* and *z* correspondingly).

From (V.1), (V.2) and (V.3) we can conclude:

$$B_p = B_x\cos\gamma_{px} + B_y\cos\gamma_{py} + B_z\sin\gamma_{pz}\,. \tag{V.4}$$

The expressions for the B_q and B_r can be found in exactly the same way, they will differ from (V.4) by the indexes q and r placed instead of p.

Let's write the coordinate system transformation in matrix form, denoting $\cos\gamma_{ij}$ by t_{ij}, where i is either p, q or r; and j is either x, y or z:

$$\begin{vmatrix} B_p \\ B_q \\ B_r \end{vmatrix} = \begin{vmatrix} t_{px} & t_{py} & t_{pz} \\ t_{qx} & t_{qy} & t_{qz} \\ t_{rx} & t_{ry} & t_{rz} \end{vmatrix} \begin{vmatrix} B_x \\ B_y \\ B_z \end{vmatrix}. \qquad \text{(V.5)}$$

It can be shown that for the axis p, the direction cosines are:

$$t_{px} = \sin\alpha \cos\beta_1,\ t_{py} = \sin\alpha \sin\beta_1, \text{ and } t_{pz} = \cos\alpha, \qquad \text{(V.6)}$$

Similarly finding the direction cosines for the axes q and r rewrite (V.5):

$$\begin{vmatrix} B_p \\ B_q \\ B_r \end{vmatrix} = \begin{vmatrix} t_{px} & t_{py} & t_{pz} \\ t_{qx} & t_{qy} & t_{qz} \\ t_{rx} & t_{ry} & t_{rz} \end{vmatrix} \begin{vmatrix} B_x \\ B_y \\ B_z \end{vmatrix} = \begin{vmatrix} \sin\alpha\cos\beta_1 & \sin\alpha\sin\beta_1 & \cos\alpha \\ \sin\alpha\cos(\beta_1+\beta_2) & \sin\alpha\sin(\beta_1+\beta_2) & \cos\alpha \\ \sin\alpha\cos(\beta_1+\beta_3) & \sin\alpha\sin(\beta_1+\beta_3) & \cos\alpha \end{vmatrix} \begin{vmatrix} B_x \\ B_y \\ B_z \end{vmatrix}. \qquad \text{(V.7)}$$

Denote the transformation matrix as A**.** Then:

$$\mathbf{B}' = A\mathbf{B}, \qquad \text{(V.7')}$$

where **B** and **B**' are the magnetic field vector in the xyz and the pqr coordinate systems respectively.

From (V.7):

$$\mathbf{B} = A^{-1}\mathbf{B}'. \qquad \text{(V.8)}$$

where A^{-1} is the inverse matrix to A.

We do not present the inverse matrix here for simplicity's sake.

V.2. The choice of the angles

The choice of the angles α, β_1, β_2 and β_3 is determined by minimization (or rather symmetrization) of the error for each component of the field, which appears due to the error in the measurements of the angles.

Let's start with α.

We have to choose the angles in such a way as to equalize (if possible) the relative error of each component of the magnetic field vector:

$$\frac{\Delta B_x}{B_x} = \frac{\Delta B_y}{B_y} = \frac{\Delta B_z}{B_z} \,. \tag{V.9}$$

The absolute errors are given by:

$$\Delta B_i = \left| \frac{\partial B_i}{\partial \alpha} \right| \Delta\alpha \,, \ (i = x\,,\, y, \text{ or } z), \tag{V.10}$$

where $\Delta\alpha$ is the absolute error of the value α.

After taking the derivatives taking into account (V.7) and (V.8) the relative errors become:

$$\frac{\Delta B_x}{B_x} = \frac{\Delta B_y}{B_y} = \cot\alpha \,\Delta\alpha \,,\ \frac{\Delta B_z}{B_z} = \tan\alpha \,\Delta\alpha \,. \tag{V.11}$$

Obviously the system of the five equations {(V.9) and (V.11)} has only one solution for $\pi/2 > \alpha > 0$:

$$\alpha = \pi/4.$$

The relative errors in this case are: $\frac{\Delta B_x}{B_x} = \frac{\Delta B_y}{B_y} = \frac{\Delta B_z}{B_z} = \Delta\alpha$.

Note that decreasing the angle α we decrease the relative error for the value of the OOP component of the field and vice versa. Then if, for example, the OOP component is needed to be measured with a high precision and only a sort of semi-qualitative measurements are needed for the IP components, the angle can be seriously decreased. It will also help to decrease the distance between probe sensitive area and sample surface. Note that even if there is no interest in the IP components at all, the proposed procedure makes sense for compensation of the error coming from the fact that the Hall probe is always tilted anyway. In this case only two measurements at each point will be needed (it will be described later).

Now in the same manner we will find the optimal angle β_1.

In this case the relative errors are:

$$\frac{\Delta B_x}{B_x} = \left| \frac{B_y}{B_x} \right| \Delta\beta_1 \,,\ \frac{\Delta B_y}{B_y} = \left| \frac{B_x}{B_y} \right| \Delta\beta_1 \,,\ \frac{\Delta B_z}{B_z} = 0 \,. \tag{V.12}$$

From (V.12) we can see that the relative errors do not depend on β_1 but depend on the components of magnetic field B_x,and B_y. The larger the ratio B_y/B_x the larger is the relative error for the B_x and vice versa.

Comparing (V.11) and (V12) we can notice that system (V.9) does not have a solution (other than the obvious case when $\Delta\alpha$ and $\Delta\beta_1$ are zero). Since it appears that the equalization of the relative errors is not possible, we will now try to find angles β_1, β_2 and β_3 such that they will symmetrize the relative errors for the B_x and B_y components of the magnetic field.

Let's denote the absolute error for the angles β_2.and β_3 as $\Delta\beta_{23}$, since they are equal and are determined by the precision of the rotary table (while the absolute errors for the angles a and β_1 depend on the precision of their measurements).

In this case, the analytical derivation of angles based on the symmetrization of the relative errors is a complicated task and so we found the angles through trial and error using educated guesses:

$$\beta_1 = \pi/4,\ \beta_2 = 2\pi/3,\ \beta_3 = 4\pi/3 \text{ (Fig. V.2 (a)).}$$

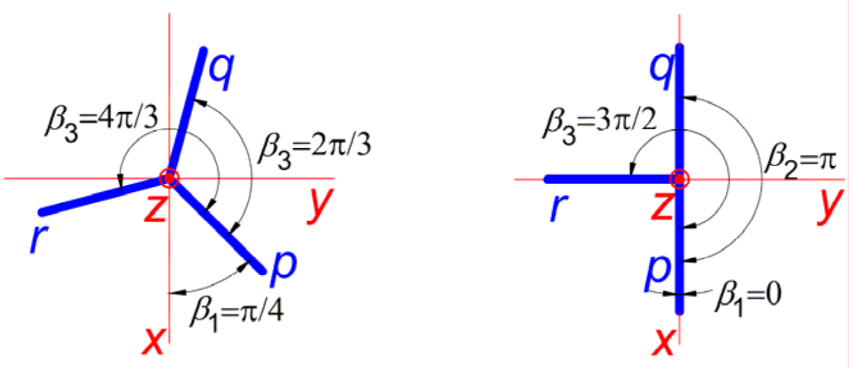

(a) (b)

Fig. V.2. Two choices of the angles (β_1, β_2, β_3).

The relative errors due to $\Delta\beta_{23}$ are:

$$\frac{\Delta B_x}{B_x} = \frac{\sqrt{2\left(B_x^2 + 4B_xB_y + 7B_y^2\right)}}{|B_x|}\Delta\beta_{23},$$

$$\frac{\Delta B_y}{B_y} = \frac{\sqrt{2\left(7B_x^2 + 4B_xB_y + B_y^2\right)}}{|B_y|}\Delta\beta_{23}, \tag{V.13}$$

$$\frac{\Delta B_z}{B_z} = \frac{\tan\alpha\sqrt{\left(B_x^2 + B_xB_y + B_y^2\right)}}{3|B_z|}\Delta\beta_{23}.$$

So to symmetrize the relative errors the angles must be:

$$\alpha = \pi/4,\ \beta_1 = \pi/4,\ \beta_2 = 2\pi/3,\ \beta_3 = 4\pi/3. \tag{V.14}$$

And the final relative errors are:

$$\begin{aligned}
\frac{\Delta B_x}{B_x} &= \cot\alpha\ \Delta\alpha + \left|\frac{B_y}{B_x}\right| \Delta\beta_1 + \frac{\sqrt{2\left(B_x^2 + 4B_xB_y + 7B_y^2\right)}}{\left|B_x\right|}\Delta\beta_{23}\,, \\
\frac{\Delta B_y}{B_x} &= \cot\alpha\ \Delta\alpha + \left|\frac{B_x}{B_y}\right| \Delta\beta_1 + \frac{\sqrt{2\left(7B_x^2 + 4B_xB_y + B_y^2\right)}}{\left|B_y\right|}\Delta\beta_{23}\,, \\
\frac{\Delta B_z}{B_x} &= \tan\alpha\ \Delta\alpha + \frac{\tan\alpha\sqrt{\left(B_x^2 + B_xB_y + B_y^2\right)}}{3\left|B_z\right|}\Delta\beta_{23}\,.
\end{aligned} \tag{V.15}$$

The matrices A and A^{-1} look like:

$$A = \left|\begin{matrix} \frac{\sqrt{2}\sin\alpha}{2} & \frac{\sqrt{2}\sin\alpha}{2} & \cos\alpha \\ -\frac{\sqrt{2}(\sqrt{3}+1)\sin\alpha}{4} & \frac{\sqrt{2}(\sqrt{3}-1)\sin\alpha}{4} & \cos\alpha \\ \frac{\sqrt{2}(\sqrt{3}-1)\sin\alpha}{4} & -\frac{\sqrt{2}(\sqrt{3}+1)\sin\alpha}{4} & \cos\alpha \end{matrix}\right|, \tag{V.16}$$

$$A^{-1} = \left|\begin{matrix} \frac{\sqrt{2}}{3\sin\alpha} & -\frac{\sqrt{2}(\sqrt{3}+1)}{6\sin\alpha} & \frac{\sqrt{2}(\sqrt{3}-1)}{6\sin\alpha} \\ \frac{\sqrt{2}}{3\sin\alpha} & \frac{\sqrt{2}(\sqrt{3}-1)}{6\sin\alpha} & -\frac{\sqrt{2}(\sqrt{3}+1)}{6\sin\alpha} \\ \frac{1}{3\sin\alpha} & \frac{1}{3\sin\alpha} & \frac{1}{3\sin\alpha} \end{matrix}\right|. \tag{V.17}$$

For $\alpha = \pi/4$ the matrices become:

$$A = \left|\begin{matrix} \frac{1}{2} & \frac{1}{2} & \frac{\sqrt{2}}{2} \\ -\frac{\sqrt{3}(3+\sqrt{3})}{12} & \frac{\sqrt{3}(3-\sqrt{3})}{12} & \frac{\sqrt{2}}{2} \\ \frac{\sqrt{3}(3-\sqrt{3})}{12} & -\frac{\sqrt{3}(3+\sqrt{3})}{12} & \frac{\sqrt{2}}{2} \end{matrix}\right|, \tag{V.16'}$$

$$A^{-1} = \begin{vmatrix} \frac{2}{3} & -\frac{\sqrt{3}(3+\sqrt{3})}{9} & \frac{\sqrt{3}(3-\sqrt{3})}{9} \\ \frac{2}{3} & \frac{\sqrt{3}(3-\sqrt{3})}{9} & -\frac{\sqrt{3}(3+\sqrt{3})}{9} \\ \frac{\sqrt{2}}{3} & \frac{\sqrt{2}}{3} & \frac{\sqrt{2}}{3} \end{vmatrix}. \tag{V.17'}$$

In some cases both the IP components of the magnetic field are symmetrical and hence only one of them, together with the out-of-plane component, is of interest. In this case only two measurements are needed to obtain the x and the z components of the magnetic field vector if the angles are chosen this way: $\beta_1 = 0$, $\beta_2 = \pi$. If the other IP component proves to be of interest, another measurement has to be done, at for example $\beta_3 = 3\pi/2$.

Also this choice of angles may be used if we need to compensate the contribution of the in-plane component of magnetic field to the Hall signal due to the tilt of the probe. In section 2.3.5 we said that in many cases we can assume that, in spite of the probe's tilt, we measure the out-of-plane component of the field. However there are magnetic configurations that will give a significant difference between B_z (the probe's sensitive axis is strictly perpendicular to the sample surface) and $B_z \cos\alpha + B_x \sin\alpha$ (the probe's sensitive axis is tilted by an angle α with respect to the Z axis). As an example, Fig. V.3 shows calculated profiles of B_z and $B_z \cos\alpha + B_x \sin\alpha$ ($\alpha = 5^{\circ}$) generated by a Halbach array (see the insertion in the figure). It can be noticed where the component B_z is nearly equal to zero the component B_x starts to contribute to the signal significantly. It's clear that when dealing with this kind of magnetic configuration it is important to take the probe's tilt into account.

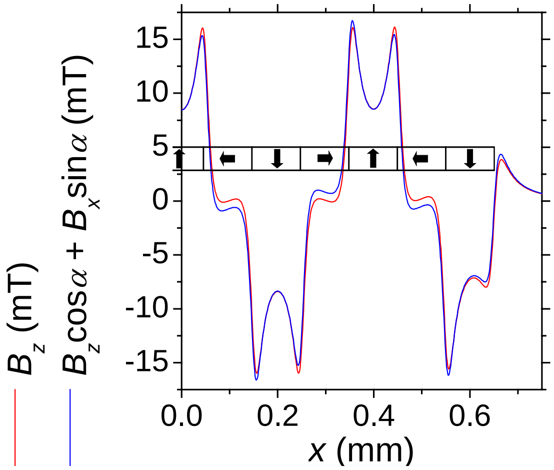

Fig. V.3. Calculated profiles of magnetic field generated by a linear Halbach array: sensitive axis strictly parallel to z-axis (red) and sensor tilted by α = 5° (blue).

For the angles $\beta_1 = 0$, $\beta_2 = \pi$, $\beta_3 = 3\pi/2$ the matrices A and A^{-1} are:

$$A = \begin{vmatrix} \sin\alpha & 0 & \cos\alpha \\ -\sin\alpha & 0 & \cos\alpha \\ 0 & -\sin\alpha & \cos\alpha \end{vmatrix}, \tag{V.18}$$

$$A^{-1} = \begin{vmatrix} \frac{1}{2\sin\alpha} & -\frac{1}{2\sin\alpha} & 0 \\ \frac{1}{2\sin\alpha} & \frac{1}{2\sin\alpha} & -\frac{1}{\sin\alpha} \\ \frac{1}{2\cos\alpha} & \frac{1}{2\cos\alpha} & 0 \end{vmatrix}. \tag{V.19}$$

And for $\alpha = \pi/4$ they become:

$$A = \begin{vmatrix} \frac{\sqrt{2}}{2} & 0 & \frac{\sqrt{2}}{2} \\ -\frac{\sqrt{2}}{2} & 0 & \frac{\sqrt{2}}{2} \\ 0 & -\frac{\sqrt{2}}{2} & \frac{\sqrt{2}}{2} \end{vmatrix}, \tag{V.18'}$$

$$A^{-1} = \begin{vmatrix} \frac{\sqrt{2}}{2} & -\frac{\sqrt{2}}{2} & 0 \\ \frac{\sqrt{2}}{2} & \frac{\sqrt{2}}{2} & -\sqrt{2} \\ \frac{\sqrt{2}}{2} & \frac{\sqrt{2}}{2} & 0 \end{vmatrix} . \tag{V.19'}$$

Relative errors in this case are:

$$\begin{aligned} \frac{\Delta B_x}{B_x} &= \cot\alpha\,\Delta\alpha + \left|\frac{B_y}{B_x}\right|\Delta\beta_1 + \frac{1}{2}\left|\frac{B_y}{B_x}\right|\Delta\beta_{23}, \\ \frac{\Delta B_y}{B_y} &= \cot\alpha\,\Delta\alpha + \left|\frac{B_x}{B_y}\right|\Delta\beta_1 + \frac{\sqrt{\left(4B_x^2 + B_y^2\right)}}{2\left|B_y\right|}\Delta\beta_{23}, \\ \frac{\Delta B_z}{B_z} &= \tan\alpha\,\Delta\alpha + \tan\alpha \cdot \left|\frac{B_y}{B_z}\right|\Delta\beta_{23}. \end{aligned} \tag{V.20}$$

BIBLIOGRAPHY

[Abel.'05] L. Abelmann, A. van den Bos, C. Lodder, "Magnetic Force Microscopy – Towards Higher Resolution", Ch. 12. In: H. Hopster and H.P. Oepen (Eds.), Magnetic Microscopy of Nanostructures, Springer-Verlag Berlin Heidelberg, p.253-284, 2005.

[Abel.'98] L. Abelmann, S. Porthun, M. Haast, C. Lodder, A. Moser, M.E. Best, P.J.A. van Schendel, B. Stiefel, H.J. Hug, G.P. Heydon, A. Farley, S.R. Hoon, T. Pfaffelhuber, R. Proksch, K. Babcock, "Comparing the resolution of magnetic force microscopes using the CAMST reference samples", J. Magn. Magn. Mater., 190, pp. 135-147, 1998.

[Abele '90] M.G. Abele, "Linear theory of yokeless permanent magnets", J. Magn. Magn. Mater., 83, pp. 276-278, 1990.

[Ardiz.] V.A. Ardizzone, "Viewing film for dc magnetic fields", www.magnerite.com

[Arkad.'47] V. Arkadiev, "A Floating Magnet", Nature 160, pp. 330-330, 1947.

[Atk.'95] R. Atkinson et al., "Visualization of magnetic DS through the interaction of their stray fields with MO garnet films". J. Magn. Magn. Mater., 149, pp. 418-424, 1995.

[Beaug.'01] E. Beaugnon, D. Fabregue, D. Billy, J. Nappa, R. Tournier, "Dynamics of magnetically levitated droplets", Physica B, 294–295, pp. 715–720, 2001.

[Beaug.'91] E. Beaugnon, R. Tournier, "Levitation of water and organic substances in high static magnetic fields", J. Phys. I, France, 1, pp. 1423–1428, 1991.

[Bend.'97] S.J. Bending and A. Oral, "Hall effect in a highly inhomogeneous magnetic field distribution", J. Appl. Phys., 81 (8), pp. 3721-3725, 1997.

[Bend.'99] S.J. Bending, "Local magnetic probes of superconductors", Advances in Physics, 48, pp. 449-535, 1999.

[Binn.'86] G. Binnig, C.F. Quate, Ch. Gerber, "Atomic Force Microscope", Phys. Rev. Lett., 56, pp. 930–933, 1986.

[Blaz.'85] Z. Blazek, V. Landa, and P. Novak, "Permanent magnets with convergent anisotropic structure", J. Phys. 46, pp. C6-295 - C6-298, 1985.

[Boer.'56/57] A.H. Boerdijk, "Levitation by static magnetic fields", Philips Technical Review, 18, pp. 125–127, 1956/57.

[Boer.'56] A.H. Boerdijk, "Technical aspects of levitation", Philips Research Report, 11, pp. 45–56, 1956.

[Boz.'49] R.M. Bozorth, "Ferromagnetic domains", Physica, 15, pp. 207-218, 1949.

[Brag.'69] V.B. Braghinskii, V.I. Osika, Instruments and Experimental Techniques, 4, p. 196, 1969.

[Brag.'70] V.B. Braghinskii, "Physical experiments with test objects", (Nauka, Moscow, 1970) (in Russian).

[Braunb.'39 1] W. Braunbek, "Freies Schweben diamagnetischer Körper im Magnetfeld", Zeitschrift für Physik, 112, pp. 764–769, 1939.

[Braunb.'39 2] W. Braunbek, "Frei schwebende Körper im elektrischen und magnetischen Feld", Zeitschrift für Physik, 112, pp. 753–763, 1939.

[Brook '03] A.J. Brook, S.J. Bending, J. Pinto, A. Oral, D. Ritchie, H. Beere, M. Henini, and A. Springthorpe, "Integrated piezoresistive sensors for atomic force-guided scanning Hall probe microscopy", Appl. Phys. Lett., 82, pp. 3538-3540, 2003.

[Brown '62] W.F. Brown, "Magnetostatic Principles in Ferromagnetism" (North-Holland Publ. Co., Amsterdam, 1962).

[Chang '92] A.M. Chang, H.D. Hallen, L. Harriott, H.F. Hess, H.L. Kao, J. Kwo, R.E. Miller, R. Wolfe, J. van der Ziel, and T.Y. Chang, "Scanning Hall probe microscopy", Appl. Phys. Lett., 61, pp. 1974-1976, 1992.

[Chet.'07] H. Chetouani, V. Haguet, C. Jeandey, C. Pigot, A. Walther, N.M. Dempsey, F. Chatelain, B. Delinchant, G. Reyne, "Diamagnetic levitation of beads and cells above permanent magnets", IEEE Transducers Eurosensors, 715. 2007.

[Chig.'09] S. Chigirinsky, M. Kustov, N. Dempsey, C. Ndao, and R. Grechishkin, "Calculations and measurements of the magnetic field of patterned permanent magnetic films for lab-on-chip applications", Rev. Adv. Mater. Sci., 20, pp. 85 – 91, 2009.

[Chris.'99] C. Christides, S. Stavroyiannis, G. Kallias, A.G. Nassiopoulou, D. Niarchos, "Giant magnetoresistance Co/Cu multilayer sensors for use in magnetic field mapping", Sensors and Actuators, 76, pp. 167–171, 1999.

[Cug.'03] O. Cugat, J. Delamare, G. Reyne, "Magnetic Micro-Actuators and Systems (MAGMAS)", IEEE Trans. Magn., 195., 2003.

[Demp.'07] N.M. Dempsey, A. Walther, F. May, D. Givord, K. Khlopkov, and O. Gutfleisch, "High performance hard magnetic NdFeB thick films for integration into micro-electro-mechanical systems", Appl. Phys. Lett. 90, 092509, 2007.

[Demp.'09] N.M. Dempsey, "Hard magnetic materials for MEMS applications" in "Nanoscale Magnetic Materials and Applications", J.P. Liu et al. (eds), (Springer 2009), p.661.

[Din.'05] R.B. Dinner, M.R. Beasley, K.A. Moler, "Cryogenic scanning Hall-probe microscope with centimeter scan range and submicron resolution", Rev. Sci. Instr., 76, 103702, 2005.

[Dum.'10] F. Dumas-Bouchiat, L.F. Zanini, M. Kustov, N.M. Dempsey, R. Grechishkin, K. Hasselbach, J.C. Orlianges, C. Champeaux, A. Catherinot, and D. Givord, "Thermomagnetically patterned micromagnets", Appl. Phys. Lett. 96, 102511, 2010.

[Dwight '61] H.B. Dwight, "Tables of integrals" (MacMillan, New York, 1961).

[Erl.'89] H. Erlichson,"The magnetic field of a circular turn," Am. J. Phys. 57, pp. 607-610, 1989.

[Evr.'69] R. Evrard, G. Boutry, J. Vac. Sci. and Technol., 6 (2), p. 279, 1969.

[Fedor '03] J. Fedor, V. Cambel, D. Gregusova, "Scanning vector Hall probe microscope", Rev. Sci. Instr., 74 pp. 5105-5110, 2003.

[Feynman '64] R.P. Feynman, R.B. Leighton, and M. Sands, "The Feynman Lectures on Physics" (Addison Wesley, Reading, MA, 1964), vol. II.

[Freem.'01] M.R. Freeman, B.C. Choi, "Advances in magnetic microscopy". Science 294, pp. 1484-1488, 2001.

[Frén.'08] M. Frénéa-Robin, H. Chetouani, N. Haddour, H. Rostaing, J. Laforêt, and G. Reyne, "Contactless diamagnetic trapping of living cells onto a micromagnet array", 30th IEEE EMBS Annual International Conference, Vancouver, BC, Canada, 20–25 August 2008, IEEE, New York, pp. 3360–3363, 2008.

[Furl.'06] E.P. Furlani and Y. Sahoo, "Analytical model for the magnetic field and force in a magnetophoretic microsystem", J. Phys. D: Appl. Phys. 39, pp. 1724–1732, 2006.

[Furl.'07] E.P. Furlani, "Magnetophoretic separation of blood cells at the microscale", J. Phys. D: Appl. Phys. 40, 1313–1319, 2007.

[Garm.'07] D. Garmire et al., "Diamagnetically Levitated MEMS Accelerometers", Traducers and Eurosensors, pp. 1203-1206, 2007.

[Geim '97] A.K. Geim, M.V. Berry, "Of flying frogs and levitrons", European Journal of Physics, 18, pp. 307–313, 1997.

[Gijs '07] M.A.M. Gijs, Microfluidic Technologies for Miniaturized Analysis Systems, Springer, USA, pp. 241–274. 2007.

[Grech.'07] R.M. Grechishkin, S. Chigirinsky, M. Gusev, O. Cugat, and N.M. Dempsey, "Magnetic Imaging Films" in Magnetic Nanostructures in Modern Technology, edited by B. Azzerboni, G. Asti, L. Pareti, and M. Ghidini Springer/Kluwer Academic, Dordrecht, 2007, pp. 195–224.

[Grech.'96] R. Grechishkin et al., "High-resolution sensitive magneto-optic ferrite-garnet films with planar anisotropy", J. Magn. Magn. Mater., 157/158, pp. 305-306, 1996.

[Greg.'03] D. Gregušová, V. Cambel, J. Fedor, R. Kúdela, J. Šoltýs, T. Lalinský, I. Kostič, and S.J. Bending, "Fabrication of a vector Hall sensor for magnetic microscopy", Appl. Phys. Lett., 82, pp. 3704-3706, 2003.

[Griff.'99] D.J. Griffiths, R. College "Introduction to Electrodynamics", 3rd edition, Prentive Hall, Upper Saddle River, New Jersey, 1999.

[Grut.'92] P. Grutter, H.J. Mamin, and D. Rugar, in "Scanning Tunneling Microscopy", Vol. II, eds. H.J. Gunterodt and R. Wiesendanger, Springer, Berlin, Heidelberg, New York, 1992.

[Gud.'02] S.A. Gudoshnikov, B.Ya. Liubimov, L.V. Matveets, A.P. Mikhailenko, Yu.V. Deryuzhkina, Yu.S. Sitnov, O.V. Snigirev, "Flux guide for high-Tc SQUID microscope with high spatial resolution", Physica C: Superconductivity, 368, Issues 1-4, pp. 66-69, 2002.

[Guill.'03] H. Guillou et al., "Geometries for high spatial resolution Hall probes", J. Appl. Phys., 93 (5), pp. 2746-2751, 2003.

[Haged.’76] W. Hagedorn and H.H. Mende, “A method for inductive measurement of magnetic flux density with high geometrical resolution”, J. Phys. E: Sci. Instr., 9, pp. 44-46, 1976.

[Hart.’05] U. Hartmann, “Scanning Probe Methods for Magnetic Imaging” Ch. 13. In: H. Hopster and H.P. Oepen (Eds.), “Magnetic Microscopy of Nanostructures”. Springer-Verlag Berlin Heidelberg, 2005, pp. 285-307.

[Hart.’82] U. Hartmann and H.H. Mende, “The stray-field induced birefringence of ferrofluids applied to the study of magnetic domains”, J. Magn. Magn. Mater. 41, pp. 244-246, 1984.

[Hassel.’08] K. Hasselbach, C. Ladam, V.O. Dolocan, D. Hykel, T. Crozes, K. Schuster, and D. Mailly, “High resolution magnetic imaging : MicroSQUID Force Microscopy”, J. Phys. Conf. Ser. 97, 012330, 2008.

[Hels.’04] L.E. Helseth, Th.M. Fischer, T.H. Johansen, “Magnetic structuring and transport of colloids at interfaces”, Journ. Magn. Magn. Mater., 277 pp. 245–250, 2004.

[Hub.’09] A. Hubert and R. Schäfer, “Magnetic domains. The Analysis of Magnetic Microstructures” (Berlin, Springer, 1998; corrected 3rd printing 2009).

[Jones ’82] G.A. Jones, E.T.M. Lacey, and I.B. Puchalska, “Bitter patterns in polarized light: a probe for microfields”, J. Appl. Phys. 53, pp. 7870-7872, 1982.

[Jooss ’02] C. Jooss, J. Albrecht, H. Kuhn, S. Leonhardt, H. Kronmüller, “Magneto-optical studies of current distributions in high-Tc superconductors”. Rep. Prog. Phys., 65, pp. 651-788, 2002.

[Joseph ’65] R.I. Joseph and E. Schlomann, “Demagnetizing field in nonellipsoidal bodies”, J. Appl. Phys., 36, pp. 1579-1593, 1965.

[Kacz.’55] J. Kaczer, “A new method for investigating the domain structure of ferromagnetics”. Czechosl J. Phys. 5, pp. 239–244, 1955.

[Kacz.’56] J. Kaczer, R. Gemperle, “Vibrating permalloy probe for mapping magnetic fields”. Czechosl J. Phys. 6, 173, 1956.

[Kejik ’05] P. Kejik, E. Schurig, F. Bergsma, R.S. Popovic, "First Fully CMOS-Integrated 3D Hall Probe", Transducers 05, Seoul, Korea, June, pp. 317-320, 2005.

[Khot.’08] V.V. Khotkevych, M.V. Milošević, and S.J. Bending, “A scanning Hall probe microscope for high resolution magnetic imaging down to 300 mK”, Rev. Sci. Instr., 79, 123708, 2008.

[Kirt.'02] J.R. Kirtley, "SQUID microscopy for fundamental studies. Physica C: Superconductivity", 368, pp. 55-65, 2002.

[Kobl.'95] M.R. Koblischka and R.J. Wijngaarden, "Magnetooptical investigations of superconductors", Supercond. Sci. Technol., 8, pp. 199-213, 1995.

[Kokor.'09] J. Kokorian, Traineeship report, "Diamagnetic levitation of sputtered NdFeB thick films above polished Higly Oriented Pyrolytic Graphite", 2009.

[Kokor.'10] J. Kokorian, Master's thesis, "Towards diamagnetic levitation in MEMS. Parallel-plate diamagnetic levitation above ultra-flat bismuth", 2010.

[Kon.'04] T. Kondo, H. Itozaki, R. Koetitz, M. Tachiki, "Sample vibration technique for HTS SQUID microscope", Physica C: Superconductivity 412-414, pp. 1501-1505, 2004.

[Koon 93] D.W. Koon, C.J. Knickerbocker, "What do you measure when you measure the Hall effect", Rev. Sci. Instrum., 64 (2), pp. 510-513, 1993.

[Koon 98] D.W. Koon, C.J. Knickerbocker, "Resistive and Hall weighting functions in three dimensions", Rev. Sci. Instrum., 69(10), pp. 3625-3627, 1998.

[Kust.'10] M. Kustov, P. Laczkowski, D. Hykel, K. Hasselbach, F. Dumas-Bouchiat, D O'Brien, P. Kauffmann, R. Grechishkin, D. Givord, G. Reyne, O. Cugat, and N.M. Dempsey, "Magnetic characterization of micropatterned Nd–Fe–B hard magnetic films using scanning Hall probe microscopy", J. Appl. Phys., 108, 063914, 2010.

[Küstl.'07] G. Küstler, "Diamagnetic Levitation – Historical Milestones", Rev. Roum. Sci. Techn., 52, 3, p. 265–282, 2007.

[Leroy '08] P. Leroy, C. Coillot, V. Mosser, A. Roux, G. Chanteur, "An ac/dc magnetometer for space missions: Improvement of a Hall sensor by the magnetic flux concentration of the magnetic core of a search coil", Sensors and Actuators A, 142, pp. 503–510, 2008.

[Leup.'92] H.A. Leupold, A.S. Tilak and E. Potenziani II, "Tapered fields in cylindrical and spherical spaces," IEEE Trans. Magn., 28, pp. 3045-3047. 1992.

[Liu '04] X. Liu, D. Mazumdar, B.D. Schrag, W. Shen, and G Xiao, "Magnetization reversal of submicrometer Co rings with uniaxial anisotropy via scanning magnetoresistance microscopy", Phys. Rev. B., 70, 014407, 2004.

[Liu ’06] C. Liu, S-H. Chung, Q. Jin, A. Sutton, F. Yan, A. Hoffmann, B.K. Kay, S.D. Bader, L. Makowski, and L. Chen, “Magnetic viruses via nano-capsid templates”, J. Magn. Magn. Mater. 302 (1), pp. 47-51, 2006.

[Liu ’98] S. Liu et al. “Effect of probe geometry on the Hall response in an inhomogeneous magnetic field: A numerical study”, J. Appl. Phys., 83 (11), pp. 6161-6165, 1998.

[Lomm.’67] J.M. Lommel, “The vibrating head magnetometer – instrument for the measurement of magnetic transitions in high-coercive films”, IEEE Trans. Magn., 3, pp. 621-624, 1967.

[Lyuks.’04] I.F. Lyuksyutov, D.G. Naugle, K.D.D. Rathnayaka, “On-chip manipulation of levitated femtodroplets”, Applied Physics Letters, 85, pp. 1817–1819, 2004.

[Mer.’00] J.M.G. Merayo, P. Brauer, F. Primdahl, J.R. Petersen and O.V. Nielsen, "Scalar calibration of vector magnetometers", Meas. Sci. Technol., 11, pp. 120–132, 2000.

[Misra 92] D. Misra, M. Zhang, Z. Cheng, “A novel 3-D magnetic field sensor in standard CMOS technology”, Sensors and Actuators A34, pp. 67-75, 1992.

[Moh.’05] J. Mohanty, R. Engel-Herbert, T. Hesjedal, “Variable magnetic field and temperature magnetic force microscopy”, Appl. Phys. A, 81, pp. 1359–1362, 2005.

[Mos.’94] V. Mosser, S. Contreras, S. Aboulhouda, Ph. Lorenzini, F. Kobbi, J.L. Robert, K. Zekentes, “High sensitivity Hall sensors with low thermal drift using AlGaAs/InGaAs/GaAs heterostructures”, Sensors and Actuators A: 43, pp. 135-140, 1994.

[Nak.’02] M. Nakamura, M. Kimura, K. Sueoka, and K. Mukasa, “Scanning magnetoresistance microscopy with a magnetoresistive sensor cantilever”, Appl. Phys. Lett. 80, 2713-2715, 2002.

[Nölt.’06] B. Nölting, “Methods in Modern Biophysics”, 2nd edition. Springer-Verlag Berlin Heidelberg, 2006.

[O’Brien] D. O’Brien et al., in preparation.

[Oral ’96] A. Oral, S.J. Bending, and M. Henini, “Real-time scanning Hall probe microscopy”, Appl. Phys. Lett., 69, pp. 1324-1326, 1996.

[Papp.’05] D.P. Pappas, A.V. Nazarov, D. Stevenson, S. Voran, M.E. Read, E.M Gormley, J. Cash, K. Marr, J.J. Ryan, “Second-harmonic magnetoresistive imaging to authenticate and recover data from magnetic storage media”. Journal of Electronic Imaging 14(1), 013015, 2005.

[Past.'94] Yu.G. Pastushenkov, A.V. Shipov, R.M. Grechishkin and L.E. Afanasieva, "Thermal remagnetization effect in RE-Fe-B permanent magnets", J. Magn. Magn. Mater., 140-144, 1103 –1104, 1995.

[Pelr.'04] R.E. Pelrine "Diamagnetic levitation", American Scientist, 92, pp. 428–435, 2004.

[Pelr.'92] R.E. Pelrine, "Magnetic field levitation", 1992, United States Patent 5,396,136.

[Pigot '08] C. Pigot et al., "Diamagnetic Levitation of Solids at Microscale", IEEE Trans. on Magnetics, 44(11), pp. 4521-5524, 2008.

[Pokh '97] T.G. Pokhil and R.B. Proksch, "A combined magneto-optic magnetic force microscope study of Co/Pd multilayer films", J. Appl. Phys., 81, pp. 3846-3848, 1997.

[Poniz.'82] V.M. Ponizovskii, "Diamagnetic suspension and its applications (survey)", Instruments and Experimental Techniques 24, pp. 833-841, 1982.

[Poodt '05] P. Poodt, M. Heijna, K. Tsukamoto, W. de Grip, P. Christianen, J. Maan, W. van Enckevort, E. Vlieg, "Suppression of convection using gradient magnetic fields during crystal growth of NiSO4·6H2O", Appl. Phys. Lett., 87, 214105, pp. 1–3, 2005.

[Port.'98] S. Porthun, L. Abelmann, and C. Lodder, "Magnetic force microscopy of thin film media for high density magnetic recording", J. Magn. Magn. Mater., 182, pp. 238-273, 1998.

[Prof.'08] H.B. Profijt et al., "Stable diamagnetic self-levitation of a micro-magnet by improvement of its magnetic gradients", J. Magn. Magn. Mater. 321, pp. 259–262, 2009.

[Prok.'99] R. Proksch, "Recent advances in magnetic force microscopy", Current Opinion in Solid State and Material Science 4, pp. 231–236, 1999.

[Pross '04] A. Pross, S. Bending, K. Edmonds, R.P. Campion, C.T. Foxon, and B. Gallagher, "Magnetic domain imaging of ferromagnetic GaMnAs films", J. Appl. Phys. 95, 7399 (2004).

[Pross '05] A. Pross, A.I. Crisan, S.J. Bending, V. Mosser, and M. Konczykowski, "Second-generation quantum-well sensors for room-temperature scanning Hall probe microscopy", J. Appl. Phys. 97, 096105, 2005.

[Purcell '86] E.M. Purcell, "Electricity and Magnetism", Berkeley Physics Course Vol. II (McGraw-Hill, New York, 1986).

[Rak.'06] H.L. Rakotoarison et al., "Methodology and Tool for generating Semianalytical Models, used to Pre-design Electromagnetic MEMS (Mag-MEMS)", 12th IEEE COMPUMAG 2006, p. 444.

[Rave '98] W. Rave, E. Zueco, R. Schäfer, A. Hubert, "Observations on high-anisotropy single crystals using a combined Kerr/magnetic force microscope", J. Magn. Magn. Mater., 177-181 (2), pp. 1474-1475, 1998.

[Rave '99] W. Rave, R. Schäfer, M. Mertig, L. Schultz, "Observations of Fe surfaces with magnetic force and Kerr microscopy", J. Magn. Magn. Mater. 196-197, pp. 115-117, 1999.

[Rice '91] P. Rice and J. Moreland, "A new look at the Bitter method of magnetic imaging", Rev. Sci. Instr., 62, pp. 844-845, 1991.

[Ripka '01] P. Ripka (ed.): "Magnetic Sensors and Magnetometers", Artech, Boston, 2001.

[Sak.'92] T. Sakurai and Y. Shimada, Application of the gas evaporation method to observation of magnetic domains, Japan. Journ. Appl. Phys. Pt.1, 31, pp. 1905-1908, 1992.

[Schott '98] Ch. Schott, D. Manic, R.S. Popovic, Microsystem for high-accuracy 3-D magnetic-field measurements, Sensors&Actuators A, 67, pp. 133-137, 1998.

[Schultz '05] L. Schultz et al., "Superconductively Levitated Transport System—The SupraTrans Project", IEEE Transactions on Applied Superconductivity, 15 (2), 2005.

[Shurk.'62] W.A. Shurkliff, "Polarized Light". Cambridge, MA, Harvard University Press, 1962.

[Simon '68] I. Simon et al., "Sensitive tiltmeter utilizing a diamagnetic suspension", Rev. Scient. Instrum., 39 (11), p.1666-1671, 1968.

[Simon '69] I. Simon, "Diamagnetic Accelerometer", United States Patent 3,465,598, 1969, Int. cl. G01p 19/08.

[Šimš.'91] J. Šimšová, R. Gemperle, and J.C. Lodder, "The use of colloid-SEM method for domain observation in CoCr films", J. Magn. Magn. Mater., 95, pp. 85-94, 1991.

[Stein.'98] R. Steiner et al, "Offset reduction in Hall devices by continuous spinning current method", Sensors and Actuators A, 66, pp. 167–172, 1998.

[Steing.'52] E. Steingroever, "Magnetische Lagerung", 1952, Patentschrift DE976997B.

[Sug.'99] A. Sugimoto, T. Yamaguchi, and I. Iguchi, "Direct observation of vortex structure in a high T_c $YBa_2Cu_3O_{7-y}$ thin film by Bitter decoration method", J. Low. Temp. Phys., 117, pp. 1347-1351, 1999.

[Szew.'83] A. Szewczyk, K. Piotrowski, and R. Szymczak, "A new method for the study of magnetic domains at temperatures below 35 K", J. Phys. D: Appl. Phys., 16, pp. 687-696, 1983.

[Thiav.'05] A. Thiaville, J. Miltat, and J.M. Garcia, "Magnetic Force Microscopy: Images of Nanostructures and Contrast Modeling", Ch. 11. In: H. Hopster and H.P. Oepen (Eds.), "Magnetic Microscopy of Nanostructures", Springer-Verlag Berlin Heidelberg, p.225-252, 2005.

[Thom.1847] W. Thomson, "On the forces experienced by small spheres under magnetic influence; and on some of the phenomena presented by diamagnetic substances", Cambridge and Dublin Mathematical Journal, 1847.

[Veauvy '02] C. Veauvy, K. Hasselbach, D. Mailly, Rev. Sci. Instr. 73, pp. 3825-3830, 2002.

[Vell.'98] B. Vellekoop, L. Abelmann, S. Porthun, C. Lodder, "On the determination of the internal magnetic structure by magnetic force microscopy", J. Magn. Magn. Mater., 190, pp. 148-151, 1998.

[Wald.'66] R.D. Waldron, United States Patent 3,597,022, 1969, Int. cl. F16c 39/06.

[Warb.'34] F.W. Warburton, "The magnetic pole, a useless concept", Am. Phys. Teacher (Am. J. Phys.) 2, pp. 1-6, 1934.

[Wils.'98] E.O. Wilson, "Consilience: the unity of knowledge". Knopf, New York, 1998.

[Wurm.'78] G. Wurmbach, N. Normann, H.H. Mende, "Measuring equipment to register the local dependence of magnetic fields with high geometrical resolution". J. Magn. Magn. Mater., 9, pp. 242-244, 1978.

[Yam.'97] S.Y. Yamamoto and S. Schultz, "Scanning magnetoresistance microscopy (SMRM): Imaging with a MR head". J. Appl. Phys. 81 (8), pp. 4696-4698, 1997.

[Yell.'05] B.B. Yellen and G. Friedman, "Programmable assembly of colloidal particles using magnetic microwell templates", Langmuir 20, pp. 2553-2559, 2005.

[Zhang '05] D.E. Zhang, X.M. Ni, H.G. Zheng, Y. Li, X.J. Zhang, and Z.P. Yang, "Synthesis of needle-like nickel nanoparticles in water-in-oil microemulsion", Mater. Lett. 59 (16), pp. 2011-2014, 2005.

[Zong.’90] L. Zongsheng et al., “A novel integrated 3-d magnetic vector sensor based on BCD technology”, Sensors and Actuators A21-A23, pp. 786-789, 1990.

[Zueco ’98] E Zueco, W Rave, R Schäfer, A Hubert, L Schultz, “Combined Kerr-/magnetic force microscopy on NdFeB crystals of different crystallographic orientation”, J. Magn. Magn. Mater., 190, pp. 42–47, 1998.

LIST OF FIGURES

LIST OF TABLES

List of articles published during the PhD study

1. M. Kustov, P. Laczkowski, D. Hykel, K. Hasselbach, F. Dumas-Bouchiat, D O'Brien, P. Kauffmann, R. Grechishkin, D. Givord, G. Reyne, O. Cugat, and N.M. Dempsey, "Magnetic characterization of micropatterned Nd–Fe–B hard magnetic films using scanning Hall probe microscopy", **J. Appl. Phys.,** 108, 063914, 2010.

2. P. Kauffmann, P. Pham, A. Masse, M. Kustov, T. Honegger, D. Peyrade, V. Haguet, and G. Reyne, "Contactless dielectrophoretic handling of diamagnetic levitating water droplets in air", **IEEE Trans. on Magn**., V. 46, issue 8, pp. 3293 – 3296, 2010.

3. F. Dumas-Bouchiat, L. F. Zanini, M. Kustov, N. M. Dempsey, R. Grechishkin, K. Hasselbach, J. C. Orlianges, C. Champeaux, A. Catherinot, and D. Givord, "Thermomagnetically patterned micromagnets", **Appl. Phys. Letters,** 96, 102511, 2010.

4. S. Chigirinsky, M. Kustov, N. Dempsey, C. Ndao, and R. Grechishkin, "Calculations and measurements of the magnetic field of patterned permanent magnetic films for lab-on-chip applications", **Rev. Adv. Mater. Sci.**, 20, pp. 85 – 91, 2009.

List of conferences (presenting author)

1. M. Kustov, N.M. Dempsey, P. Laczkowski, D. Hykel, D. Givord, O. Cugat, R. Grechishkin and K. Hasselbach, “Measurement of the 3 components of a magnetic field using a single component Scanning Hall Probe Microscope”, **EMSA 2010** (8th European Conference on Magnetic Sensors and Actuators), Bodrum, Turkey, July 4-7, 2010 *(poster)*.

2. M. Kustov, R. Grechishkin, F. Dumas-Bouchiat, D. O’Brien, K. Hasselbach, P. Laczkowski, D. Hykel, S. Soshin, D. Givord, and N.M. Dempsey, “Comparative magneto-optic and scanning Hall probe microscopy of magnetic field distributions in patterned Nd-Fe-B films”, **EUROMAT 2009** (European Congress and Exhibition on Advanced Materials and Processes), Glasgow, UK, September 7-10, 2009 *(oral)*.

3. M. Kustov, R. Grechishkin, F. Dumas-Bouchiat, and N.M. Dempsey, “Quantitative imaging and straightforward calculation of magnetic fields of micropatterned permanent magnet films for magnetic MEMS”, **JCGE 2008** (Conférence des Jeunes Chercheurs en Génie Electrique), Lyon, France, December 16, 17, 2008 *(poster)*.

4. C. Pigot, P. Kauffmann, H. Chetouani, M. Kustov, “Diamagnetic levitation applied to the μ-manipulation of μ- and nano-objects and biological cells”, **Minatec Crossroads 2008**, Grenoble, France, June 23-27, 2008 *(poster)*.

ACKNOWLEDGEMENTS

Here in a few lines I would like to acknowledge everybody who helped me with this work, who supported me in difficult periods of my life, who shared both my joys and worries, who made the time of my PhD so memorable…

First of all I would like to express my profound gratitude to the members of my graduation committee. It has been truly an honor to have such a jury! I would like to thank Dr. Leon Abelmann for agreeing to be a reviewer of the manuscript and the president of the jury, and for the valuable remarks and comments that he made on my PhD manuscript, in particular concerning the question of 3D measurements. I would like to thank Dr. Rudolf Schäfer for agreeing to be a reviewer of the work and for his corrections, detailed remarks and valuable suggestions on every section of the manuscript. I truly appreciate the work that has been done on reviewing the manuscript. I would like to thank Dr. Vincent Mosser for agreeing to be an examiner at my defense, also for the Hall probes that he provided us (without the probes a large part of this work would not be possible), and for the interesting discussion that we had concerning reduction of the noise of the Hall signal and other aspects of the Hall measurements.

I would like to express my deep gratitude to my supervisors, Orphée Cugat, Nora M. Dempsey, and Gilbert Reyne, who always supported and encouraged me and kept me motivated.

Nora, I am not sure that the level of my English is enough to express the deep and sincere gratitude that I feel. All your comprehensive help and support concerning every aspect of my life in general and my PhD study in particular cannot be possibly measured. I am also amazed by the unbelievable combination of straightforwardness and tactfulness that you always demonstrated (I was thinking that such a combination is simply impossible before I got to know you). When I felt depressive, my spirits always rose up after I talked to you. Thank you very much for everything! Yes, and I came to love Ireland in spite of the fact that I've never been there (yet).

Orphée, first of all, thank you for the possibility to do my PhD in such a beautiful place, the possibility that I owe mostly to you, Rostislav and the Fondation Nanosciences. Also thanks for all your help concerning versatile aspects of my PhD and my life. I truly appreciate that doing all the organization and paper work for the team (in particular, doing lots of papers for me as well), you always managed to find time for regular meetings concerning my work and other aspects of my life. All these meetings were very important for me. And your "davai, davai!" kept me well motivated! Thank you also for the very useful kitchen stuff and other things that you gave Gor and me for our apartment (thanks a lot to Nora and Alexey too for helping to furnish our apartment). It is hard to count every thing that you helped me with. Thanks a lot for everything, then!

Gilbert, first of all thank you for considerably increasing my "magnetic intuition"! All the meetings that we had were extremely valuable to me. Many of the aspects, especially concerning questions of computational electromagnetism that you told me, I never even heard before. Thanks a lot also for the bike that you gave me. It still serves me well and I like it very much!

I would like to express my profound gratitude to Prof. Rostislav Grechishkin, who has truly been a mentor to me for many years. Rostislav, first of all thank you for the opportunity to do my PhD in Grenoble, without you I would never got such a chance. Thank you for the comprehensive help with countless aspects of this work in particular and of my studies and many other aspects of my life, both in Grenoble and in Tver. Thanks for many shared ideas that were aw well used in this work. You help and support during all these years is truly invaluable! And thank you that you managed to come for my defense!

I would like to thank the Fondation NanoSciences for the financial and administrative support of this work. Without this funding this work would not be possible. In particular, I would like to thank the secretaries, Mmes Marie-Laure Eliard, Karine Argento, Maud Dayez for helping with many administrative questions, including renewing my 'cartes de sejours'. It would take a lot of my time if I had to do it myself. Thanks also to Stéphanie Monfront for all her organization work. And thanks to

Stéphanie and M. Hérino for coming to support me at my defense! It was always a pleasure to come to the Fondation because of the friendly people that work (or once worked) there.

I would like to express my deep gratitude to Klaus Hasselbach who in fact supervised a large part of this PhD work (the part concerning the SHPM). Klaus, first of all thank you for integrating me into your team. And I truly appreciate the time you spent helping me with the problems with the set-up and discussing various questions, from magnetic measurements to superconductivity. I always truly enjoyed working in your 'salle de manips'!

I would like to thank Dominique Givord for his support in many questions and for the numerous discussions that we had on the different aspect of this work. Dominique, thanks a lot for you help and thanks that you could find the time for all these many discussions, the value of which cannot be overestimated!

I would like to thank Sergey Soshin who helped me a lot when I was preparing to start the PhD study and during the PhD study itself. Sergey, I truly appreciate all the help and support that you offered to me at different stages of my life. Thank you for all the discussions that we had concerning soft and hard magnets, demagnetization factors, programming and many other things (all of them cannot be really counted). Thanks a lot also for your Python scripts that I often used in this work. And thank you for all this material that you sent me during the PhD study.

I would like to thank Frédéric Dumas-Bouchiat for all his support he offered to me and for the thermomagnetically patterned magnets that I could investigate in this work. Fréd, really thanks for being such a nice colleague!

Thanks to Daniel O'Brien for his help and support, and for the topographically patterned magnets that I could investigate in this work as well. Thanks also for showing me a lot of the lab's equipment and explaining its working principles. And thanks, Dan, for being such a nice interlocutor at every group's 'miam' and other occasions. It has always been a pleasure to talk to you, both of science and of life.

Thanks a lot to Piotr Laczkowski and Danny Hykel for the SHPM setup. Piotr, thank you also for always keeping a place in you car to take me back to Grenoble from the concerts that we saw together in Lyon. Danny, thanks for all the help with programming, and thanks for being a nice interlocutor too, who I was always pleased to talk to.

Thanks to Benoit Delinchant for the MacMMEMS/CADES computational tool that was widely used in this work, and for the very useful consultations on the usage of the tool.

I am thankful to my ex-'stagiaire' Jaap Kokorian (whom I was supposed to supervise but who, in fact, seldom needed my supervision) for his marvelous job on the flying magnet and also for the pleasant time we spent in and outside the lab. Thanks also to you and Maaike for the nice trip and perfect dinner in the Netherlands!

Thanks to Paul Kauffmann for his masks and substrates for the topographically patterned magnet. Thanks also for the many scientific (and not) discussions that we had during these years and thanks for helping me to become integrated in the team when I arrived in Grenoble.

I am thankful to Laurent Cagnon and Michael Darques for the bismuth nanowires.

I would like to thank Olivier Geoffroy who let me to work in his 'salle de manips' and use a part of it also as an office. Thanks, Olivier, also for letting me borrow your equipment and for the valuable consultations concerning the soft magnetic materials.

Thanks to Pierre Molho for lending us his microscope's lamp, power supply and polarizers for our set-up.

Thanks to Victor Gaude for the clean room lessons and for the Si microfluidic chamber.

Thanks to Alexey Dobrynin for the discussions on the different aspect of magnetism, and also for giving us a lot of useful stuff for our apartment.

Thanks to Christian Jeandey for discussions concerning optimization of levitation systems.

I would like to thank the secretary of the Scolarité, Mme Isabelle Raffin, for being so friendly and helpful with the document for the PhD defense. Also I am thankful to all the secretaries from G2Elab and Institut Néel who in any event helped me with all the numerous documents.

My dear friends, Geta and Luiz, one can only dream of having such friends as you! Thanks a lot for all the pleasant time that we spent in and outside the lab. Thanks for the bike rides we had together. Luiz (and Carol), thanks for the marvelous trip to Rome! And thanks for the support you are always ready to offer!

Geta, thank you for being so nice a friend and a colleague. It was truly a pleasure to train you up working with the SHPM. I am sure you will get nice results with the aid of the device. Thanks a lot for helping with the 'pot' after my defense (also thanks a lot to Nora, Orphée, Ancuta, and all the MNM group). And thank you and also Teo, Anca, and Flo for the nice trip to Avignon.

I would like to thank Harald Profijt for helping me a lot with becoming integrated into the team and providing me with some useful stuff like a coverlet etc. when I just arrived and did not have anything.

Thanks to Christian Pigot who helped me a lot to get settled in the lab and in the city, and for showing me some of the lab's equipment. Also I would like to thank Jerome, Luis, Aline, and the others from the microsystems team who helped me to become integrated in the team.

Also I would like to thank Yuepeng, Laurent, Cheikh, Cuong, Idris (who also considerably enlarged my French vocabulary) and all the people from the MNM group and the Nano department of Institut Néel for being such nice colleagues. I will always remember the Institut Néel as a pleasant and friendly place to be in.

Thanks to my flat-mate Gor for having found such a nice apartment where we stayed for more that 1.5 years, and for being a nice flat-mate and friend.

I would like to express my profound gratitude to my ex-landlady Galina, who was as a grandmother to me during all the 1.5 year that I lived at her place.

I would like to thank a friend of mine, Sergey, for his support during all these years. It is always pleasant to have a like-minded person.

I would like to thank my friend Lisa for advises and warm encouragement, and also for a nice trip in Germany.

Last but not least I would like to thank my mother Lidia, whose continual support was always palpable, despite that I was more than 2500 km from home.

Again I want to thank everybody who helped me and supported me during all these three years! I am sorry if forgot to mention somebody personally!